ABSTRACT

Title of Dissertation: UNVEILING THE ENVELOPE AND DISK:
A SUB-ARCSECOND SURVEY OF YOUNG
STELLAR SYSTEMS

Leslie W. Looney, Doctor of Philosophy, 1998

Dissertation directed by: Dr. Lee G. Mundy, Associate Professor
Department of Astronomy

Nearby (less than 500 light years away) stellar systems are forming that may someday resemble our solar system. By studying these forming stars, we can probe the origins, evolution, and properties of circumstellar disks that are probably similar to the disk from which our planets formed. This thesis endeavors to address some of the major questions in modern star formation and planet formation theory via sub-arcsecond resolution observations of the envelopes and disks surrounding the youngest stars.

We present the results of a detailed survey of 24 nearby forming stars with sub-arcsecond $\lambda = 2.7$ mm interferometric observations covering a range of evolutionary states. These multi-array observations fully sample spatial scales ranging from $0\farcs4$ to $50''$, allowing the first consistent comparisons of circumstellar structures, as seen in their dust emission. The images show a variety of structure and complexity. The optical/near-infrared T Tauri stars (DG Tauri, HL Tauri, GG Tauri, and GM Aurigae) have continuum emission that is dominated by compact ($< 1''$) circumstellar disks; these disks are resolved in two systems. The embedded near-infrared sources (SVS13 and L1551 IRS5) have both extended and compact continuum emission. The deeply embedded sources (L1448 IRS3, NGC1333 IRAS2, NGC1333 IRAS4, VLA 1623, and IRAS 16293-2422) have continuum emission that is dominated by the extended envelope. If these systems have disks, they are not more massive than the expected mass of the envelope extrapolated to small scales. Our sample has a large number of multiple systems; morphologically, they can be separated into three types: independent envelope, common envelope, and common disk. The three types have distinct size scales which are probably indicative of the fragmentation scale and formation mechanism for multiple systems.

Many of the systems were modeled in the *u,v* plane. All of the systems could be well fit by the standard power-law models for envelopes and disks. In the more massive envelopes, a self-consistent temperature profile was needed to achieve acceptable fits. Our data conclusively show that the majority of the emission and mass in the embedded systems is due to the envelope. Even though the embedded systems have massive envelopes, any circumstellar disk is less than 10% of the system mass, and the disk is not more massive than circumstellar disks in optical systems.

UNVEILING THE ENVELOPE AND DISK: A SUB-ARCSECOND SURVEY OF YOUNG STELLAR SYSTEMS

by

Leslie W. Looney

Dissertation submitted to the Faculty of the Graduate School of the
University of Maryland, College Park in partial fulfillment
of the requirements for the degree of
Doctor of Philosophy
1998

Advisory Committee:

Associate Professor Lee G. Mundy, Chair/Advisor
Professor Robert Dorfman, Co-chair
Associate Professor Richard Ellis
Professor Jordan Goodman
Associate Professor Andrew Harris

PREFACE

This thesis presents the results of sub-arcsecond observations in the $\lambda = 2.7$ mm continuum. These observations were made with the Berkeley-Illinois-Maryland Association (BIMA) millimeter Array, which operates under funding from the National Science Foundation. The key aspect of this thesis was the evolution of high resolution capability of the BIMA array. The project consisted of adding 7 new outrigger stations to the current array which increased the baseline lengths to 1.9 km for the 1997/1998 observing season. This work would not have been possible without the vision and foresight of Lee Mundy, Leo Blitz, and Jack Welch, the early work of Bill Erickson and Arie Grossman, and the continued efforts of Lee Mundy, Jack Welch, Dick Plambeck, Doug Thornton, Mel Wright, and Rick Forster.

The high resolution imaging of the binary system L1551 IRS5 presented in Chapter 3 has been published by the Astrophysical Journal (Looney, Mundy, & Welch 1997, ApJ, 484, L157). Chapters 4 and 5 were written as manuscripts suitable for submission to professional journals. Much of the work has been presented at numerous scientific conferences, such as the Protostars and Planets IV conference in Santa Barbara, California, the Star Formation Workshop in Santa Cruz, California, the Binary Star Formation Conference in Stony Brook, New York, and at meetings of the American Astronomical Society in San Antonio, Toronto, and Washington, D.C.

DEDICATION

For my parents.

Without their support, I would never had made it.

ACKNOWLEDGMENTS

As I begin to type this acknowledgment section (the final section) of the thesis, I am amazed that the graduate school ride is finally over. But, as I walk away and shuffle into line for the next ride, I am comforted to know that I have enough carnival tickets. This is not due to me alone, and I have a large number of important people to thank for their encouragement, help, advice, and prodding.

Of course, the first person to acknowledge is Lee Mundy. He took a chance on a physics graduate student who walked into his office one day to talk about interferometry, and for that I am grateful. He has been a great advisor, giving me kicks when I needed them, filling paper drafts with red ink, providing insight into the fundamental and detailed physics of star formation and astronomy in general, working with me for many weeks at Hat Creek, and finally, not dropping me on the hard, cold rock when belaying me while rock climbing.

Next, I thank the Laboratory for Millimeter Astronomy (LMA). As a large support group you can't ask for more. The skills and diversity of the group is one of its greatest assets. I thank the LMA faculty, staff, postdocs, and students. Leo Blitz for talking to me about my instrumentation interest and accepting me into the group. Stuart Vogel for his continued LMA support and enthusiasm. Bill Erickson for help with the initial fiber optic project. Andy Harris, as a committee member, has been essential for this manuscript. He provided comments and asked questions that has made it a better piece of work. In addition, Andy helped with accurate lab measurements of the temperature dependency of fiber cable, and he has given advice that will be useful in my new position at MPE. Peter Teuben for too many things to list, typically dealing with Miriad code or Linux. Jim Morgan for all his help, especially on Wip. Steven White for all his discussions and help. Marc Pound for letting me listen to his mighty Dylan collection and for not dropping heavy weights on me. Mark Wolfire for his indispensable expertise on the self-consistent radiative transfer code. Of course, thanks to Paula Palmisano and Susan Gammon. Elizabeth Lada for many useful conversations about star formation in clusters. Pedro Safier for tolerating many questions about cloud collapse. Kate Isaak for her interest in physics and instrumentation. Joe McMullin, a fellow advisor sibling, was very inspirational when I first started working in the Astronomy Department. Robert Gruendl for many things, including my first rock climbing trip. Mike Regan, another USF alum, for many useful discussions. Michele Thornley, my immediate advisor sibling, for too much to address, especially the help on my move to Germany. Sally "when do I get the computer?" Watt for her fun attitude, support, and dog stories. Kartik Sheth for saying what he thinks and not saying what he thinks. Other LMA graduate students I would like to thank: Tamara Helfer, Chin Fei Lee, Nikolaus Volgenau (especially for reading two thesis chapters), and Stef McLaughlin.

I owe a big debt of gratitude to the entire Astronomy Department. They accepted me into the department and gave me as much, or at times better, support than the Physics department. This includes Marv Leventhal, John Trasco, Grace Deming, Mike A'Hearn, Dennis Wellnitz, Mark Houdashelt, Mary Ann Phillips, Sharon Elliott, Pat Pai, and Thelma Bublitz. I thank Eve Ostriker and Jim Stone for useful discussions. I especially thank John Ohlmacher and Bill Sebok for all of the computer support.

I will never forget my entire incoming Physics class; it was fun. Some graduate students to single out: Fred Cawthorne, Sham Chotoo, Susan Chotoo, Raj Mohanty, Jennifer Catelli, Joe Gerber, Milan Reichbach, Manher Jariwala, and Matt Herndon. Especially, Jeff Miller for starting me on heavy weights and long walks to lunch. In addition, I want to thank the Physics members of my committee (Robert Dorfman, Richard Ellis, and Jordan Goodman) for finding time to finally meet. Of course, I want to thank Jane Hessing for helping keep the paperwork minimal.

There are a number of people to thank at Berkeley and Hat Creek. Jack Welch for all of his help and enthusiasm for star formation and instrumentation. Dick Plambeck and Mel Wright for their early A array work and interest. The electronics staff at Berkeley, including Ed Fields, Doug Thornton, and Calvin Cheng. All of the staff at Hat Creek, especially Rick Forster, Matt Fleming, Mark Warnock, Susie Jorgenson, and Marc Masters. At Illinois, I would like to thank Doug Roberts for his software support on modi4.

I want to thank all of the astronomy graduate students for their support and sarcasm. Amy Fredricks for all the music (I'll miss that). Laura Woodney for weights and being a great officemate. Neil "don't crash!" Nagar for rock climbing and other interests. Yanga Rolando Fernández-Ponte Martin for being interested in so much. Don Horner for understanding the meaning of a cold beverage. Arunav Kundu needs no introduction. And in no specific order, Rob Cavallo, K. D. Kuntz, Kristen Miller, Scott Miller, Keith Watt, Chun Xu, Wayne Baumgartner, Glenn Piner, Jim Braatz, and Keith Watt.

I want to thank the system engineers at NASA Kennedy Space Flight Center (DPS division) for their encouragement. It was fun to launch shuttles. (The decision to go to graduate career was made there.) Special thanks to Bob Panzak (surf dude!) and Kathy Milon.

Of course, I could never had finished this work without my family, their support, love, and selfless help. I dedicated this thesis to Mom and Dad (Linda and Jerry Looney) for their support, which has been unquestioned for my entire undergraduate and graduate career. I would also like to dedicate the work to my grandmother Mildred Davies. I want to thank Jodie Touchton, Cheyenne Touchton, Austin Touchton, Elsie Looney, Frank Looney, Helen Davies, Melonie Wilkerson, Cindy Wilkerson, David Davies, and Tina Dudeck. Of course, Randy Pierce, Bonnie Robertson, and Bob Robertson.

Finally, I come to Trudi Reinhold, Tim Richmond, Leslie Sherman, and Photon. Thanks Trudi for too many things to mention, inspiration, help, and for just being wonderful (high school to this baby). Of course, Photon for her willingness to try anything. Thanks (Are you done already?) Tim. Tim is probably the most responsible for me being in radio astronomy. His interest in astronomy was the impetus for my senior electrical engineering project. Thanks to Tim and Trudi for random acts: Maine, Seattle, the Montana lake that was only 10 miles, and the undergraduate years. Leslie for her tenderness and support over the writing of this thesis. It wasn't all glamour and parties, but it was fun.

TABLE OF CONTENTS

LIST OF TABLES

LIST OF FIGURES

Chapter 1

Introduction

1.1 “Let there be light”

The origin of the Sun and Earth has been pondered by every civilization throughout history. Most modern theories of solar system formation rely upon a flattened disk of material surrounding the young Sun (e.g. Safranov 1960; Cameron 1962), as first hypothesized by Kant (1755). It is from this circumstellar disk of gas and dust that the planets, comets, and all bodies in the solar system were formed. Unfortunately, we are 4.5 billion years too late to study this disk directly, so we must turn to other stellar systems to understand better our own origins.

Modern star formation observation and theory require the presence of circumstellar disks to explain the formation and appearance of young suns that evolve within the dense regions of molecular clouds. By studying these low mass forming stars, we are probing the origins, evolution, and properties of circumstellar disks that are probably similar to the disk from which our planets formed. Thus, an investigation into the formation of stars and their disks provides unique insights into the origin of our own solar system. In addition, a firm grasp of the fundamental stellar formation process addresses persistent questions in astrophysics, such as the binarity of stars, the origin of the recently discovered extra-solar planetary systems (e.g. Mayor & Queloz 1995; Marcy & Butler 1996) and, since stars and star clusters are the building blocks of galaxies, the origin of galaxies and galaxy clusters.

1.2 Some Star Formation History

Although the origin of the Sun has been discussed throughout history, the first scientific step of our continuing journey toward understanding star formation came with the invention of the telescope in the early years of the seventeenth century. The telescope opened an era where stars, planets, and many other objects were scrutinized in ever increasing detail. Some of the first historical accounts of images seen through telescopes were of nebulae, such as the famous M42 in the belt of Orion, discovered as a nebula by Nicholas Peirsec in 1620 (Glyn Jones 1968). The Messier catalog (Messier 1781), the “M” in M42, illustrates the increasing awareness of nebulous objects being observed with the early telescopes.

Prior to the nineteenth century, nebulae were popularly interpreted as dense clusters of stars that might be resolved with larger telescopes. With improved instrumentation, astronomers realized that, while some of these objects were dense stellar clusters, many others consisted of interstellar gas and dust. Many astronomers began to speculate that these nebulae were involved in the star formation process. In 1798, William Herschel described the Orion nebula (M42) as “an unformed fiery mist, the chaotic material of future suns” (Glyn Jones 1968). Herschel envisioned one of the first star formation evolutionary sequences: planetary nebulae, to bright emission nebulae, to stars with nebulosity (Herschel

1784). Although the sequence was flawed, Herschel's hypothesis stimulated further work on the basic physics of cloud collapse. Norman Lockyer (1887; 1888) invoked contraction under self-gravity as the main source of energy for stars (Helmholtz 1853; Kelvin 1863), and Jeans (1928) formulated the criteria for collapse instabilities in a self-gravitating system.

Recognition of star formation as an ongoing process came with the identification and study of pre-main-sequence stars at various stages of evolution. T-Tauri stars, strong emitters of Hα, were detected toward the Taurus Clouds (Joy 1945, 1946) and were interpreted as young stars (Baade 1952; Herbig 1952). Bok globules, very compact dark features that were noticed in photographic plates (Barnard 1919), were argued to be early compact condensations containing protostars (Bok & Reilly 1947). The interpretation of these two types of objects as young stellar systems was a watershed in the observational record of star formation, linking old thoughts to new. The stage was set for the breakthrough of infrared and millimeter/sub-millimeter observational technologies that would change how star formation was viewed.

1.3 The Modern Era of Star Formation

Within the last three decades, the combined efforts of optical, infrared, and millimeter/sub-millimeter observations have unveiled the birthplace of stars: stars form in dense, dusty regions of molecular clouds. One of the most important observational facts is that pre-main-sequence stars are brighter in the infrared than similar stars on the main sequence (Mendoza 1966). The excess infrared emission is explained as arising from circumstellar dust absorbing photospheric radiation and re-radiating the emission at longer wavelengths (Mendoza 1968; Lynden-Bell & Pringle 1974; Harvey, Thronson, & Gatley 1979; Cohen & Kuhi

1979; Cohen 1983; Adams, Lada, & Shu 1987; Bertout, Basri, & Bouvier 1988).

Four distinct morphological classes of young stellar objects were defined based primarily on their infrared emission (Lada & Wilking 1984; Lada 1987; André, Ward-Thompson, & Barsony 1993). The classes are numbered 0 (sometimes called Extreme Class I), I, II, and III in order of decreasing far infrared emission and posited increasing age. Each class has a different shape in a spectral energy distribution plot, $log(\lambda F_\lambda)$ versus $log(\lambda)$, where F_λ is the flux measured at wavelength λ. The quantity $\log(\lambda F_\lambda)$ is proportional to the energy flux radiated in a logarithmic wavelength interval; the peak of the curve in such a diagram occurs at the wavelength where the greatest amount of energy is radiated.

A Class 0 object is deeply embedded within its prenatal envelope. The spectral energy peaks in the sub-millimeter, with no detectable emission shortward of 20 μm. Class I is a less embedded object with a broad blackbody spectral energy that increases longward of 2 μm, peaking in the 10-100 μm band. Class II is an optically revealed young star (typically a classical T Tauri star) with a spectral energy distribution peaking around 2 μm, characteristic of a main-sequence photosphere plus a significant excess in the infrared. Class III is a pre-main sequence star (typically a weak-lined T Tauri star) with essentially a stellar blackbody spectrum, peaking around 1 μm, and no sign of an accretion disk. These morphological differences tie the class system into an evolutionary sequence (cf. Shu, Adams, & Lizano 1987; Shu et al. 1993). This rudimentary sketch of isolated star formation has six rough stages.

(1) Within a large cloud complex supported by magnetic fields and turbulent motions, the neutrals particles drift past the field lines, a process called ambipolar diffusion (Mestel & Spitzer 1956). Due to ambipolar diffusion, an originally stable cloud forms a centrally condensed core over a period of $\sim 10^6$

years or more (Nakano 1984; Fiedler & Mouschovias 1992; Basu & Mouschovias 1994). The cloud evolves to the verge of collapse with a Jeans mass of material in the central region. The theoretical expectation is that the core will quasi-statically evolve toward the density distribution of an isothermal sphere, $\rho \propto r^{-2}$ (Larson 1969; Shu 1977).

(2) When the central region is sufficiently condensed, the cloud begins to collapse dynamically. The theory of this stage has been extensively studied over the last three decades. The isothermal spherical collapse problem, with only thermal pressure to counteract gravity (excluding magnetic fields), has two classes of self-similar solutions: the Larson-Penston (LP) solution (Larson 1969; Penston 1969; Hunter 1977) and the Shu solution (Shu 1977). Although these solutions are idealized, they have important ramifications on the nature of the collapse.

The primary difference between the two solutions is the general morphology of the collapse. The LP solution starts with a uniform density cloud that evolves into a density profile with $\rho \propto r^{-2}$ and an infall velocity of 3.3 times the local sound speed at the time that a finite mass forms at the center. The Shu solution starts with a $\rho \propto r^{-2}$ density profile that is at rest; the collapse begins in the center and moves outward at the local sound speed creating an "inside-out" collapse wave. The mass infall rate of the Shu solution is constant with time, but the mass infall rate of the LP solution is initially a maximum, then asymptotically approaches the Shu value. Both solutions tend toward free-fall density profiles of $\rho \propto r^{-3/2}$ as the collapse proceeds.

Detailed numerical calculations, which included magnetic fields and other effects, are more like the LP solution than the Shu solution: an inner uniform density profile that evolves into a $\rho \propto r^{-2}$ density profile with infall velocities near 3.3 times the local sound speed (Whitworth & Summers 1985; Mouschovias, Paleologu, & Fiedler 1985; Fiedler & Mouschovias 1993; Basu & Mouschovias

1994,1995; Safier, McKee, & Stahler 1997). However, the Shu solution is currently more widely used, especially the property of the constant mass infall rate over all time scales.

(3) About 10^4 years after the collapse has started, the object can be classified as a protostar (Class 0) with a central source that is probably burning deuterium. However, the majority of the object's luminosity still derives from mass accretion of the envelope onto the protostar. The infalling envelope (radii of many 1000's of AU) of the young protostar is a large mass reservoir, typically containing more than twice the mass of the final star. This massive envelope completely obscures the young star at wavelengths shorter than about 20 μm.

As the collapse of the envelope proceeds, the infalling mass fails to accrete directly onto the surface of the protostar due to the angular momentum of the infalling material. The mass effectively "misses" the protostar and builds a circumstellar disk around it. Cassen & Moosman (1981) showed the evolution of the young disk was strongly dependent upon both the distribution of mass and angular momentum in the original cloud and the dissipative processes within the circumstellar disk. For reasonable assumptions, they found that a circumstellar disk would grow more massive and larger with time. Building upon these results, Stahler et al. (1994) considered a disk with negligible viscosity. They found the disk radius to be a strong function of time, increasing as t^3.

When observers first began to look for infalling material toward young systems, they found instead strong outflows, for example, the spectacular molecular outflow of L1551 IRS5 (Snell, Loren, & Plambeck 1980). Now, molecular outflows, optical jets, and HH objects are known to be commonly associated with young systems. This was one of the earliest puzzles in modern star formation. Why does a collapsing object have an outflow?

In current models of star formation, the outflow process is recognized as an essential element of star formation, carrying away much of the angular momentum of the infalling material and preventing the star from spinning near breakup speed. The details of angular momentum exchange is still not well understood. The outflow is observed to originate from within the central few AUs of the object (e.g. Edwards, Ray, & Mundt 1993; Wilner, Rodríguez, & Ho 1998). The theoretical explanation for the outflow utilizes interactions between the accretion disk and the young protostellar magnetic field (e.g. Königl & Ruden 1993; Shu et al. 1994; Ouyed & Pudritz 1997)

(4) During the next few 10^5 years, the object evolves from an envelope dominated to a circumstellar disk dominated system. The mass reservoir of the envelope is depleted through accretion onto the growing circumstellar disk and star, and through evacuation of the system by the powerful outflow. These systems are Class I objects that can be observed in the near-infrared, but are still obscured at optical wavelengths.

(5) By an age of about 10^6 years, the envelope of the young star is mostly dissipated, and the source becomes a visible T Tauri star (Class II). The fact that these stars are seen at optical wavelengths yet have excess infrared and millimeter emission compared to a stellar photosphere, argues for the presence of a flattened disk structure surrounding the star (Lynden-Bell & Pringle 1974; Harvey, Thronson, & Gatley 1979; Cohen & Kuhi 1979; Cohen 1983; Adams, & Shu 1985; Bertout, Basri, & Bouvier 1988). Such circumstellar disks are known to be relatively common among T Tauri stars with typical disk masses of ~ 0.02 $M_{\odot}$, and masses as high as 0.1 $M_{\odot}$ (Beckwith et al. 1990; Osterloh & Beckwith 1995). (The minimum disk mass for the proto-solar system is estimated to be ~ 0.01 $M_{\odot}$.) The disks have radii extending to ~ 100 AU and typically have low-mass, larger scale structures of ~ 1000 AU that exhibit Kepler rotation (e.g.

Sargent & Beckwith 1991; Hayahi, Ohashi, & Miyama 1993; Koerner & Sargent 1998; Dutrey et al. 1998).

(6) The final stage in this simple picture of stellar evolution (Class III to main sequence stars) is the epoch of disk clearing which occurs around 10^7 years after the initial collapse. It may have been during this stage in the solar system's evolution that the planets, Kuiper belt, and Oort cloud formed. Theoretical work has shown that the formation of large planets opens gaps in the disk and may be an important mechanism for disk clearing (e.g. Lin & Papaloizou 1979). As the disk clears, the young star gravitationally contracts toward the main sequence, finishing the journey started more than 10^7 years earlier.

The above "cartoon" summary of star formation is based upon numerous observational and theoretical advances made over the last few decades. Although it gives an overall notion of the astrophysical processes of low mass star formation, it is still a sketchy outline that spans many orders of magnitude in physical conditions— from densities of 10^3 to 10^4 $\frac{particles}{cm^3}$ and temperatures of 10 K to 50 K in the molecular cloud to densities of 10^{23} to 10^{28} $\frac{particles}{cm^3}$ and temperatures of 100 K to 10^6 K in the environs of stars and planets. The important aspects of the above sequence for this thesis are the evolutionary patterns and size scales relevant to the structures that will be examined in more detail in the following chapters— the circumstellar envelope and circumstellar disk.

1.4 Oops, What About Binaries?

Surveys of main-sequence stellar systems have shown that the majority of stars are in binary or multiple systems (Heintz 1969), with separations ranging from a few $R_\odot$ to 10^4 AU, and the distribution peaking near 30 AU (Duquennoy &

Mayor 1991). In addition, recent surveys of star forming regions show that the occurrence of binaries in the young visible T Tauri stars is twice that of local main-sequence stars (Simon et al. 1992; Ghez, Neugebauer, &, Matthews 1993; Leinert et al. 1993; Reipurth & Zinnecker 1993; Ghez, White, & Simon 1997). Thus, the most likely outcome of the star formation process is a binary star. Yet, the star formation sequence discussed in the previous section does not address binary systems.

Three theories have been commonly invoked to explain the formation of binary systems: fission, capture, or fragmentation (cf. Clarke 1995; Pringle 1991). The fission of a protostar into two objects has been shown not to work theoretically (Durisen et al. 1986) and is ruled out observationally because young stars are not observed to be rotating near breakup speeds (Bouvier et al. 1993). The second idea, capture of a passing stellar system, is too inefficient a mechanism to produce the observed abundance of binary systems, and does not easily explain the numerous very young systems (Clarke & Pringle 1991). The favored mechanism for the formation of binary and multiple stellar systems involves the fragmentation of either the initial cloud core, the collapsing condensation, or the circumstellar disk.

The fragmentation of a cloud core by either geometry or cooling-driven thermal fragmentation can produce binary systems with separations ranging from 10 to 10^4 AU (Boss & Bodenheimer 1979; Monaghan & Lattanzio 1986; Bonnell et al. 1991; Bonnell & Bastien 1992; Boss 1993; Bate, Bonnell, & Price 1995). Rotationally driven fragmentation, due to m = 1 spiral mode instabilities in the circumstellar disk, can form binary systems with separations ranging from 10 $R_\odot$ to 100 AU (Adams, Ruden, & Shu 1989; Shu et al. 1990; Bonnell 1994; Bonnell & Bate 1994). With some tuning of formation parameters, binary systems can be created at the earliest stage of the collapse, or early in the circumstellar disk formation.

1.5 Nature of the $\lambda = 2.7$ mm Continuum Emission

This thesis will be primarily concerned with observations of millimeter continuum emission from young stellar systems. There are three emission mechanisms that could be responsible for the observed flux from forming stars at millimeter wavelengths: (1) bremsstrahlung free-free emission from the interaction between free electrons and positive ions in the stellar wind or outflow, (2) nonthermal synchrotron radiation from relativistic electrons moving in the magnetic field of stellar flares or the active corona, and (3) thermal emission from dust particles surrounding the young star.

The flux of bremsstrahlung free-free emission can be written as

$$S_\nu = \int B_\nu(T)(1 - e^{-\tau})d\Omega,$$

where $\tau \propto T^{-1/3}\nu^{-2}g_{ff}$ (cf. Spitzer 1978). Here, $B_\nu(T)$ is the Planck function $\left(B_\nu(T) = \frac{2h\nu^3}{c^2}\frac{1}{e^{h\nu/kT}-1}\right)$, T is the temperature of the plasma, h is the Planck constant, ν is the frequency, c is the speed of light, k is the Boltzmann constant, τ is the optical depth, $d\Omega$ is the solid angle subtending the source, and g_{ff} is the free-free quantum mechanical correction, or the Gaunt factor. The Gaunt factor varies as $g_{ff} \propto T^{0.15}\ \nu^{-0.1}$ in the radio regime (e.g. Mezger & Henderson 1967). In the optically thin limit ($\tau \ll 1$), $S_\nu \propto B_\nu(T)\tau \propto \nu^2\ \nu^{-2.1} \propto \nu^{-0.1}$, and in the optically thick region ($\tau \gg 1$), $S_\nu \propto B_\nu(T) \propto \nu^2$. Theoretical models of stellar winds predict free-free emission with $S_\nu \propto \nu^{0.6}$ to $\nu^{1.2}$ depending upon the geometry of the wind (Panagia & Felli 1975; Reynolds 1986). In classical T Tauri or embedded systems, the observed free-free emission arises from ionized gas in stellar winds or jets with typically flat or slightly rising ($S_\nu \propto \nu^{0.3}$) (e.g. Cohen, Bieging, & Schwartz 1982; Snell & Bally 1986; Rodríguez et al. 1989; Morgan, Snell, & Strom 1990). Typically, the flux of a classical T Tauri or an embedded system at $\lambda \leq 2$ cm is weak ($\leq$ 2 mJy) and dominated by free-free emission. This emission, scaled to $\nu = 110$ GHz with $\alpha = 0.6$ is ~5 mJy. Although bremsstrahlung emission may contribute a few mJy of flux at our frequency, it is not dominant in most systems.

The flux of synchrotron radiation emission scales with frequency as $S_\nu \propto \nu^\alpha$, but, due to various absorption and emission effects and the complexity of the geometry, the index can range from α = -1 to α = +4 (cf. Feigelson 1987). Unlike bremsstrahlung, synchrotron emission is time variable and usually circularly polarized (e.g. Feigelson 1987; André 1987). Many weak lined T Tauri systems have synchrotron radiation arising from stellar flare activity and electrons gyrating in strong magnetic loops in the active corona (e.g. Stine et al. 1988; Suters et al. 1996). The nonthermal emission associated with young stellar systems is expected to peak around 10 GHz and decrease with increasing frequency (cf. Dulk 1985). In addition, among low luminosity systems (< 100 $L_\odot$), nonthermal synchrotron emission has only been detected toward weak-lined T Tauri stars (e.g. André et al. 1992) which have little circumstellar material. Since none of the objects in this thesis are weak-lined T Tauri stars, synchrotron radiation should not contribute any of the observed λ = 2.7 mm emission.

Thus, most of the emission observed for this thesis is from thermal dust particles surrounding the forming star. The circumstellar dust is heated directly by stellar photons and by stellar energy which has been reprocessed into longer wavelength photons by dust structures close to the protostar. The dust emission at these wavelengths exhibits characteristics of a modified blackbody spectrum: a

Planck function times a broad frequency-dependent dust opacity function. Although the dust surrounding young stellar sources obscures the central object at optical wavelengths, the dust is a strong emitter in the infrared to millimeter wavelengths, and the dust emission can be studied to derive profiles of the dust temperature, density, and composition.

The dust grain properties and composition can vary significantly depending on the environment; in cold regions the grains could form large fluffy aggregates or simply acquire ice mantles, in warmer regions ices can sublimate off the dust grains, and in hot regions the dust can be destroyed completely (e.g. Gehrz 1989; Weintraub, Sandell, & Duncan 1989; Henning, Michel, & Stognienko 1995). The dust opacity function is strongly dependent upon the dust grain composition, size, distribution, and chemistry (Krügel & Siebenmorgen 1994; Pollack et al. 1994). Thus, the determination of the dust temperature, density, and opacity from dust thermal emission in the environments of young stars is explicitly dependent on the underlying emissivity properties of the dust.

In the standard parameterized description, the dust opacity is characterized by a mass opacity, κ_ν, which has a power-law dependence on frequency, $\kappa_\nu = \kappa_0(\frac{\nu}{\nu_0})^\beta$ (cf. Hildebrand 1983; Beckwith and Sargent 1991). The mass opacity coefficient, κ_0, and the frequency dependence of the mass opacity coefficient, β, is assumed to fully characterize the emissivity. While real interstellar dust properties are undoubtedly more complex, this simple treatment provides a reasonable first approximation at millimeter wavelengths where the expected grain sizes are small compared to the wavelength. Unfortunately, even these two parameters are not well determined at millimeter wavelengths, and the uncertainty in the frequency dependence limits the reliability of extrapolating properties from other wavelengths where these parameters are somewhat better determined (Hildebrand 1983).

Studies of circumstellar material have suggested that dust emissivity at submillimeter wavelengths varies with $\beta \sim 1$ (Beckwith and Sargent 1991; Beckwith et al. 1990; Weintraub, Sandell, & Duncan 1989) rather than $\beta = 2$ as found in calculations based on grain dielectric properties (c.f. Draine 1990). However, measurements of β are very uncertain (measured values of β range from 0 to 2) due to uncertainties in the measurements and in the true material distribution in the systems (Beckwith and Sargent 1991).

For this thesis, we will use the parameterized dust opacity description with values of κ_o and β consistent with other works on young stellar objects (e.g. Beckwith & Sargent 1991; Ohashi et al. 1991; Osterloh & Beckwith 1995): $\kappa_\nu = 0.1(\nu/1200\text{ GHz})\text{ cm}^2\text{ g}^{-1}$, corresponding to $\kappa_\nu = 0.009\text{ cm}^2\text{ g}^{-1}$ at $\lambda = 2.7$ mm. We will also generally assume that dust properties are not a function of distance from the central source. These assumptions are necessary because the data and analysis central to this thesis work do not provide strong constraints on dust properties.

1.6 The Standard Envelope Model

The emergent radiation from a sphere at an impact parameter ω in the plane of the sky is simply

$$I_\nu(\omega) = \int_{-l_{max}}^{+l_{max}} B_\nu\Big(T(r)\Big)\rho(r)\kappa_\nu e^{-\tau(l)} dl,$$

where r is the radius from the center of the sphere, $B_\nu\Big(T(r)\Big)$ is the Planck function, $T(r)$ is the temperature as a function of r, $\rho(r)$ is the density as a function of r, κ_ν is the dust opacity at a given frequency, dl is the line of sight depth through the sphere at the impact parameter, l_{max} is the maximum line of sight depth into the sphere along the impact parameter, and $e^{-\tau(l)}$ is the attenuation from dl to the front of the sphere. The total integrated flux from a sphere with radius R would be

$$S_\nu = 2\pi \int_0^R I_\nu(\omega) \frac{\omega d\omega}{D^2},$$

where D is the distance to the source.

1.6.1 Envelope Density and Temperature

As can be seen from this treatment, three quantities are needed to calculate the expected flux: $\rho(r)$, κ_ν, and $T(r)$. The standard model uses power-laws for all three quantities (Adams, Shu, & Lada 1988; Beckwith et al. 1990; Adams, Emerson, & Fuller 1990; Keene & Masson 1990; Beckwith & Sargent 1991; Terebey, Chandler, & André 1993).

For the density profile, a power-law is a good assumption. Theoretical models predict density profiles that range from an static isothermal sphere profile of $\rho \propto r^{-2}$ to a free-fall density profile of $\rho \propto r^{-3/2}$ (Larson 1969; Penston 1969; Hunter 1977; Shu 1977). The $\rho \propto r^{-2}$ profile is derived from the balancing of thermal pressure and gravity; the $\rho \propto r^{-3/2}$ profile comes from the free-fall collapse of a $\rho \propto r^{-2}$ density profile. We adopt the standard density power-law description with index p,

$$\rho(r) = \rho_o \left(\frac{r}{r_o}\right)^{-p}$$

for all radii, where ρ_o is the density at radius r_o. For this simple treatment, we will assume that the envelope has a single power-law. However, the density profile may be a broken power-law; one power-law for the interior of the envelope and another for the outer radii.

The temperature profile of an optically thin dust envelope heated by a central star will have a power-law dependence in radius and the stellar luminosity

(L_*) (cf. Spitzer 1978),

$$T(r) = T_o \left(\frac{r}{r_o}\right)^{-q} \left(\frac{L_*}{L_o}\right)^{\frac{q}{2}},$$

where T_o is the dust temperature at the radius r_o for a stellar luminosity of L_o. The power-law index q is dependent on the dust opacity power-law index such that $q = \frac{2}{4+\beta}$. This relation is derived from energy balance between absorbed and emitted radiation in an optically thin envelope. Since reasonable values of β range from 0 to 2, the temperature power-law index is between 0.33 and 0.5. For most of our calculations, we will adopt a temperature profile of the form $T(r) = T_o\left(\frac{r}{r_o}\right)^{-0.4}$, or $\beta = 1$.

Detailed radiative transfer calculations (Rowan-Robinson 1980; Wolfire & Cassinelli 1986; Butner et al. 1990) are consistent with our assumed temperature radial dependence when the envelope is optically thin at the wavelength where the peak energy transport occurs. However, the temperature profile will diverge from a single power-law as the envelope becomes optically thick at the primary wavelengths of energy transport. For a centrally peaked envelope, such as $\rho \propto r^{-2}$, the envelope can become optically thick at the inner radii, resulting in a steeper temperature profile.

The value of T_o can be estimated from the source luminosity. Wilner, Welch, & Forster (1995) derived the following relation,

$$T_o = 233 \left(\frac{L}{L_\odot}\right)^{-0.25} \left(\frac{r}{1AU}\right)^{-0.4} \mathrm{K}$$

based on detailed self-consistent radiative transfer models of spherical, central illuminated optically thin clouds (Rowan-Robinson 1980; Wolfire & Cassinelli 1986). This formula has an estimated accuracy of 20 % in temperature for $1 \leq \left(\frac{L}{L_\odot}\right) \leq 6 \times 10^6$.

1.7 The Standard Circumstellar Disk Model

We adopt the standard description of a circumstellar dust disk (Adams, Shu, & Lada 1988; Beckwith et al. 1990; Dutrey et al. 1996; Mundy et al. 1996). We assume that the disk is circular and geometrically thin. The emergent flux from an element of the disk is then given by

$$dS = B_\nu(T)(1 - e^{-\tau}) \cos i \, \frac{dA}{D^2},$$

where $B_\nu(T)$ is the Planck function, τ is the optical depth, i is the inclination angle between the line of sight and the disk axis, and D is the distance to the source. The optical depth can be written as function of the surface density, $\Sigma(r)$, the dust opacity at frequency ν, κ_ν, and the inclination angle, i,

$$\tau = \frac{\Sigma(r)\kappa_\nu}{\cos i}.$$

Since the disk is typically inclined to the line of sight, the disk appears elliptical on the plane of the sky. To generalize the orientation of the circumstellar disk, we also need to define the position angle γ, measured east of north of the major axis of the ellipse.

1.7.1 Disk Density, Temperature, Inclination Angle, and Position Angle

In our model, five quantities are needed to calculate the expected flux from a circumstellar disk: the surface density $\Sigma(r)$, the dust opacity κ_ν, the disk temperature $T(r)$, the inclination i, and the principal axis of the projected disk on the sky γ. However, there are strong cross correlations between the parameters (Thamm, Steinhacker, & Henning 1994). The standard model uses power-laws for the $\Sigma(r)$, κ_ν, and $T(r)$ (Adams, Shu, & Lada 1988; Beckwith et al. 1990; Adams, Emerson, & Fuller 1990; Beckwith & Sargent 1991; Dutrey et al. 1996).

For the surface density profile, we adopt a power-law

$$\Sigma(r) = \Sigma_o\left(\frac{r}{r_o}\right)^{-p},$$

for all radii, where Σ_o is the surface density at radius r_o. This p is not the same as the envelope volume density index p. Current theoretical models include power-law surface density profiles, but the power-law index varies depending upon the angular momentum distribution in the original molecular cloud and the viscosity in the circumstellar disk. The surface density profile is predicted to range between $r^{-0.5}$ to $r^{-1.75}$ (Cassen & Moosman 1981; Cassen & Summers 1983; Lin & Pringle 1990; Ruden & Pollack 1991; Stahler et al. 1994).

For the temperature profile, we adopt a power-law of the form

$$T(r) = T_o\left(\frac{r}{r_o}\right)^{-q},$$

for all radii, where T_o is the temperature at a radius r_o. A temperature power-law index of q=0.75 is expected theoretically from both an active, self-luminous accretion disk and a passive photon heated disk (Lynden-Bell & Pringle 1974). In both cases, the temperature is derived from balancing the energy absorbed and emitted by the dust. For an active disk the heating is dominated by viscous dissipation, and for a passive disk the absorbed energy is dominantly radiation from the central source. However, multi-wavelength surveys have shown that $q = 0.5$ is more typical of real systems (e.g. Adams, Lada, & Shu 1987; Beckwith et al. 1990). It has been proposed that the smaller value of q could be due to flared disks (Kenyon & Hartmann 1987), gravitational instabilities within the disk (Adams, Ruden, & Shu 1989), or backheating by the envelope (Natta 1993). For our modeling, we adopt a power-law index of $q = 0.5$ and $T_o = 350$ K.

1.8 Thesis Aim

The primary goals of this thesis are to examine closely some of the fundamental questions that remain in the "cartoon" evolution of a low mass star sketched in §1.3 and to address the placement of binary systems within that sequence. Specifically,

- What structures are observed in the youngest sources compared to the older sources? What are their size scales? How can we characterize the structures?
- What is the density profile in the envelopes of the youngest sources? Does it follow the density profile of an isothermal sphere $\rho \propto r^{-2}$, collapse region $\rho \propto r^{-1.5}$, or something else?
- Do embedded sources have distinct circumstellar disks? Or are their disks small enough to be indistinguishable from the extension of the envelope down to small size scales?
- What constraints can we place on the earliest binary systems?
- Can we observationally place binary systems into the cartoon version of star formation?
- What is the surface density profile of circumstellar disks in optical systems?
- How does disk mass and size evolve with time?

We address these problems utilizing high resolution $\lambda = 2.7$ mm continuum interferometry. This thesis included an involvement in the state-of-the-art instrumentation needed to achieve sub-arcsecond resolution with the Berkeley-Illinois-Maryland-Association (BIMA) millimeter aperture synthesis array located in Hat Creek California[1] (Welch et al. 1996). A major facet of this thesis was participation in the designing, building, and implementation of the long baseline fiber-optic links, which has increased BIMA's longest baseline from 300 m to almost 2 km. Although I will not discuss the hardware aspects in this thesis, the effort has provided us with the highest angular resolution of any millimeter array in the world. With this unprecedented sub-arcsecond resolution, we have made a survey of 24 young stellar systems at various stages of evolution.

Since this is a physics thesis and not an astronomy thesis, I will briefly review radio interferometry and some of the basic tools one can use for modeling interferometric data in Chapter 2. If more depth is required on radio interferometry or its application, a detailed reference is "Interferometry and Synthesis in Radio Astronomy" by Thompson, Moran, & Swenson (1986).

Chapter 3 highlights L1551 IRS5, one of the first objects observed with BIMA's high resolution ($0\farcs31$) configuration. With the increased resolution, we determined that this archetypical isolated Class I object is actually a close binary system. The system is found to consist of three dust emission structures: a large-scale envelope, a circumbinary structure, and two small-scale circumstellar disks.

Chapter 4 introduces our sub-arcsecond survey of young stellar systems. The source morphology and the general trends that can be drawn from the sample are presented. The $\lambda = 2.7$ mm emission of the optical/near-infrared objects is dominated by emission from the circumstellar disks; the circumstellar disks are resolved in three systems. The $\lambda = 2.7$ mm emission of the embedded objects is dominated by the large-scale circumstellar envelopes, which typically contain

---

[1] The BIMA Array is operated by the Berkeley Illinois Maryland Association under funding from the National Science Foundation.

$\sim 75\%$ of the system mass. All of the embedded objects in the sample are binary or multiple systems on scales of $30''$ or less. The multiplicity of these objects can be broken down into three groups: separate envelope systems, common envelope systems, and common disk systems.

Chapter 5 details the modeling of six embedded systems (L1448 IRS3, NGC 1333 IRAS2 A, SVS 13 A, SVS 13 B, NGC 1333 IRAS4 A, AND NGC 1333 IRAS4 B) and three optical systems (HL Tauri, DG Tauri, and GG Tauri). We find that the standard power-law description for the circumstellar envelope and the circumstellar disk fit the data. We examine the optically thin temperature assumption for the circumstellar envelope by utilizing the self-consistent radiative transfer model of Wolfire & Cassinelli (1986). The disk of HL Tauri provides significant constraints on the surface density power-law index and the disk size. The circumbinary disk of GG Tauri is fit by a range of surface density power-law indices and inner and outer radii, but there is a 2.5σ detection in the outer u,v data bin that suggests the presence of compact structure in the system, possibly one or two circumstellar disks.

Chapter 6 draws overall conclusions for this thesis and examines some of the future directions of the work, including new techniques which will be available with the addition of the new $\lambda = 1.3$ mm receivers at BIMA.

Chapter 2

Interferometry: Theory and Application

2.1 Introduction

Since interferometry plays a major role in this thesis, we will briefly review the basic concepts and equations of interferometry. More detailed descriptions of astronomical radio interferometry can be found in numerous sources (e.g. Bracewell 1965; Kraus 1966; Thompson, Moran, & Swenson 1986; Rohlfs 1986). We will also discuss the characteristics of various emission structures in the *u,v* plane with a detailed description of power-law emission distributions.

Since a significant amount of the modeling in this thesis is done in the Fourier space, we strive to convey an understanding of the *u,v* plane that will be useful for discussions in subsequent chapters. For the envelope and disk, we will discuss the correlation of the density power-law index and the slope in the *u,v* plane, which is intended to provide a context for the more extensive modeling in later chapters. The more detailed modeling will accommodate geometries, size scales, and optical depth effects, but the general ideas conveyed in this chapter are important to understand how various models are demonstrated in the *u,v* plane.

2.2 Interferometric Basics

The basic interferometer consists of two antennas separated by a baseline vector $\mathbf{D}$ (Figure 2.1). The two antennas convert electromagnetic radiation into voltages $V_1(t) = V_1 e^{i\phi_1(t)}$ and $V_2(t) = V_2 e^{i\phi_2(t)}$. Correlation between the two signals is obtained by multiplying and time averaging. The output of the correlator is $\left\langle V_1(t) V_2^*(t) \right\rangle$, which is the mutual coherence function of the two voltages.

When this simple two element array observes a point source along the normal unit vector $\hat{\mathbf{s}}$, the voltages at antenna 1 and 2 are $V_1(t) = ae^{i\left(2\pi\nu t\right)}$ and $V_2(t) = ae^{i\left(2\pi\nu t + \Phi(t)\right)}$ respectively. Here, a is related to the point source amplitude, ν is the signal frequency, and $\Phi(t)$ is the phase difference at antenna 2 due to the path difference $\left(\Phi(t) = \frac{2\pi}{\lambda}\mathbf{D} \cdot \hat{\mathbf{s}}\right)$. The path difference is from the extra time required for the signal to reach antenna 2. This delay is called the geometric delay, $\tau_g = (\mathbf{D} \cdot \hat{\mathbf{s}})/c$.

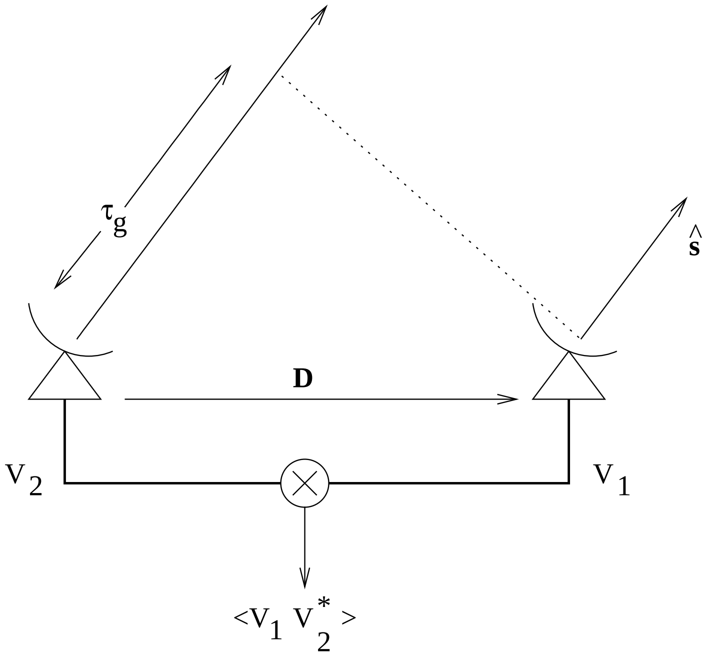

Fig. 2.1. A simple two element interferometer.

The real part of the time average of antenna 1 multiplied by the complex conjugate of antenna 2 is

$$Re\Big(\Big\langle V_1(t)V_2^*(t)\Big\rangle\Big) = a^2\cos\Phi(t),$$

where a^2 is the flux of the point source. This relation illustrates that the response of the interferometer to a point source is a fringe pattern similar to the classic double-slit experiment. In addition, the cosine interference pattern has a λ/D angular spacing between maxima. Thus, the natural unit for baseline length is wavelengths, and the baseline length sets the angular resolution of the interferometer. The farther apart the antennas, the smaller the fringe pattern on the sky, and the higher the angular resolution of the array.

This result can be generalized to an extended source structure with a brightness $B(x, y)$ (Figure 2.2), where x and y are coordinates in radians. Note that Figure 2.2 defines a left-hand coordinate system so that a positive displacement in x is equivalent to an eastern displacement on the sky, an astronomical convention. The antennas point to a position defined such that $x = y = 0$. This position is also called the pointing center of the observation. The antenna pair have a primary beam power pattern $P(x, y)$ which is due to the cross power pattern of the two antennas. The primary beam pattern of a typical interferometer can be approximated as a normalized Gaussian.

Since the radiation from different parts of the extended structure is incoherent, the source brightness is equivalent to a collection of point sources. The correlation, or visibility V, from each point source is then

$$dV = B(x, y)P(x, y)e^{i\Phi(t)}dxdy,$$

where $\Phi(t) = \frac{2\pi}{\lambda}\mathbf{D}\cdot\hat{\mathbf{s}}$. We define a position on the sky called the phase center. In this example, and for most interferometers, the phase center and the pointing center are at the same location on the sky, but such coincidence is not required.

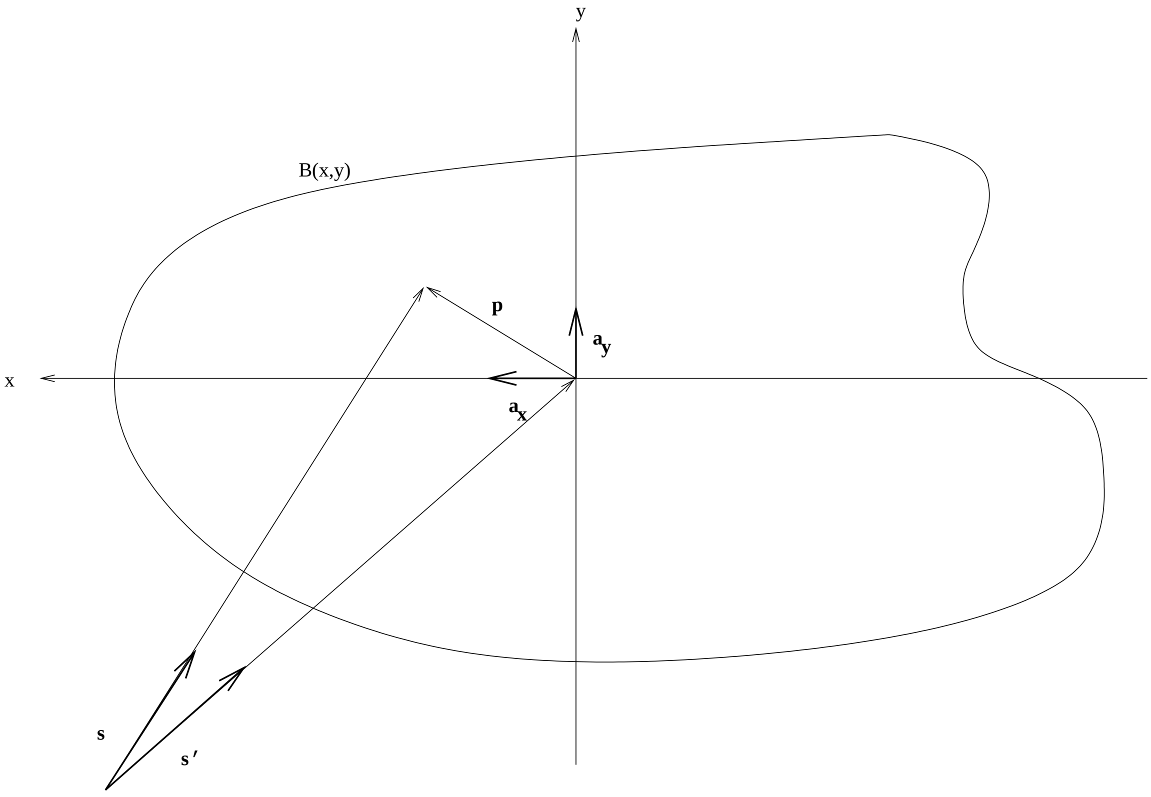

Fig. 2.2. Vectors for observing an extended brightness structure.

The phase of the phase center, $\Phi' = \frac{2\pi}{\lambda}\mathbf{D} \cdot \hat{\mathbf{s}}'$, is subtracted from the visibility phase, Φ. This is done in practice by adding a delay, called the instrumental delay τ_i, to the antenna 1 signal path, such that $\tau_i = \tau_g$ for the phase center. The instrumental delay sets the phase to zero for the phase center. In other words, the phases of other objects in the field are measured with respect to the phase center, so a point source located exactly at the phase center will have zero phase.

Putting all of this together the visibility dV can be written as

$$dV = B(x,y)P(x,y)e^{-i(\Phi-\Phi')}dxdy.$$

Since

$$\Phi - \Phi' = \frac{2\pi}{\lambda}\mathbf{D} \cdot (\hat{\mathbf{s}} - \hat{\mathbf{s}}')$$

and

$$\hat{\mathbf{s}} - \hat{\mathbf{s}}' = \mathbf{p} = x\mathbf{a_x} + y\mathbf{a_y},$$

where $\mathbf{a_x}$ and $\mathbf{a_y}$ are unit vectors along the x and y axes, respectively. Then,

$$\Phi - \Phi' = \frac{2\pi}{\lambda}\mathbf{D} \cdot (x\mathbf{a_x} + y\mathbf{a_y}).$$

If we define

$$u = \frac{\mathbf{D} \cdot \mathbf{a_x}}{\lambda} \quad \text{and} \quad v = \frac{\mathbf{D} \cdot \mathbf{a_y}}{\lambda}$$

then

$$\Phi - \Phi' = 2\pi(ux + vy),$$

and the visibility function is

$$dV = B(x,y)P(x,y)e^{-2i\pi(ux+vy)}dxdy.$$

By integrating over the entire sky, we obtain

$$V(u,v) = \int_{-\infty}^{+\infty}\int_{-\infty}^{+\infty} B(x,y)P(x,y)e^{-i2\pi(ux+vy)}dxdy.$$

This result is the general interferometric equation. The response of an antenna pair is the Fourier Transform of the sky brightness distribution times the primary beam pattern. Equivalently, the response is the Fourier transform of the brightness distribution convolved with the Fourier transform of the primary beam pattern. The *u,v* plane is simply the Fourier transform space of the sky, and the actual measurement of any antenna pair is the complex visibility at a specific point in the *u,v* plane determined by the baseline vector projected onto the sky.

There are five important points evident from this simple review.

(1) The baseline vector can point from antenna 1 to antenna 2 or the other way around, depending upon an arbitrary choice. The consequence of swapping the orientation of the baseline vector is that the phase difference changes sign since u and v change sign. Thus, the visibility function is intrinsically Hermitian: $V(u,v) = V^*(-u,-v)$. This Hermitian property is also evident from a property of Fourier Transforms: the Fourier Transform of a real function, in this case the sky brightness $B(x,y)$, is Hermitian.

(2) The *u,v* plane can be sampled by following the source as it rises and sets. Since *u,v* positions are defined as the baseline lengths projected onto the sky, an interferometer tracking an astronomical source will sample different *u,v* values as the projected baseline varies. As the source rises in the sky, the projected baseline length will be foreshortened. At transit, the projected baseline length will be the maximum length of the antenna separation. As the source sets, another foreshortened projected baseline length will specify *u,v* points in another quadrant of *u,v* space.

(3) In principle, we can recover the sky brightness distribution from the interferometer output by Fourier transforming the *u,v* visibility data. However, in practice, an interferometer can only sample a limited amount of *u,v* space, making

a direct inverse Fourier transform to recreate the sky brightness distribution difficult. The brightness function is typically reconstructed by gridding the u,v data and using a Fast Fourier Transform (FFT) routine. Since the u,v plane is never fully sampled, sidelobes are introduced into the restored map. In other words, a point source in the sky would not be a point source in the image plane, but rather have a structure equivalent to the point source convolved with the Fourier transform of the u,v sampling pattern. The reconstructed image can be "cleaned-up" using a deconvolution algorithm, such as CLEAN (Högbom 1974).

(4) The interferometer filters out structures that are large compared to the fringe spacing. A brightness distribution that overlaps the negative and positive amplitude lobes of the fringe pattern will average out to zero correlated power. This can be demonstrated by thinking of the central hole in the sampling of u,v space by the interferometer; practical antennas have a finite diameter which limits the interferometer from sampling the smallest u,v distances. For the BIMA antennas (diameter = 6.1 meters), the smallest u,v distance measured is 2.1 kλ. A very extended object on the sky will have a very compact Fourier transform. If the object's Fourier transform falls inside the u,v sampling of an antenna pair, the object will not be detected. This can be a very useful feature of the interferometer: the antenna pairs are essentially bandpass filters for spatial scales. A specific u,v range gives source brightness information on a specific spatial scale; larger structure is resolved out. Unlike an optical telescope, an interferometer is excellent at filtering out large scale emission, even if it is brighter than the compact emission.

(5) Longer baselines provide the resolution to see smaller scale structure in the source. One of the main motivations behind the expansion of the BIMA baselines was to gain the ability to image objects with angular sizes of order 1 arcsecond—specifically, circumstellar disks. With the current system (a longest

projected baseline of 1.9 km), the BIMA array is sensitive to spatial scales as small as $0\farcs2$.

2.3 How do Simple Structures Transform to the *u,v* Plane?

The *u,v* distance versus amplitude plot will be common in this thesis, so we will briefly explain three simple source characteristics in the *u,v* plane, and §2.4 will discuss a power-law distribution in more rigor. Figure 2.3 presents three simple emission structures on the sky and the Fourier transform *u,v* space. The horizontal axis is the *u,v* distance measured in kλ (1000s of wavelengths), and the vertical axis is the amplitude in Janskys (1 Jy = $10^{-23}\frac{ergs}{cm^2\ Hz}$). In this example, the horizontal axis is only u to illustrate the basic features of specific brightness distributions.

In the top plot of Figure 2.3, the interferometer response is shown for a 1 Jy point source offset from the phase and pointing center. The solid line is the visibility amplitude and the dashed line is the visibility phase. In the *u,v* plane, a point source corresponds to a constant amplitude for all *u,v* distances. If the point source were at the map center, the expected phase would be zero for all *u,v* points, as explained in §2.2. The spatial offset in this figure illustrates that an offset on the sky does not alter the amplitude of the measured visibility. However, as the plotted visibility phase shows in this figure, an offset from the phase center is equivalent to a visibility phase shift. The phase is a ramping function that is wrapped to stay within $\pm\pi$.

In the second plot of Figure 2.3, the interferometer response is shown for two 0.5 Jy point sources separated by $3''$ in x and y. The Fourier transform has

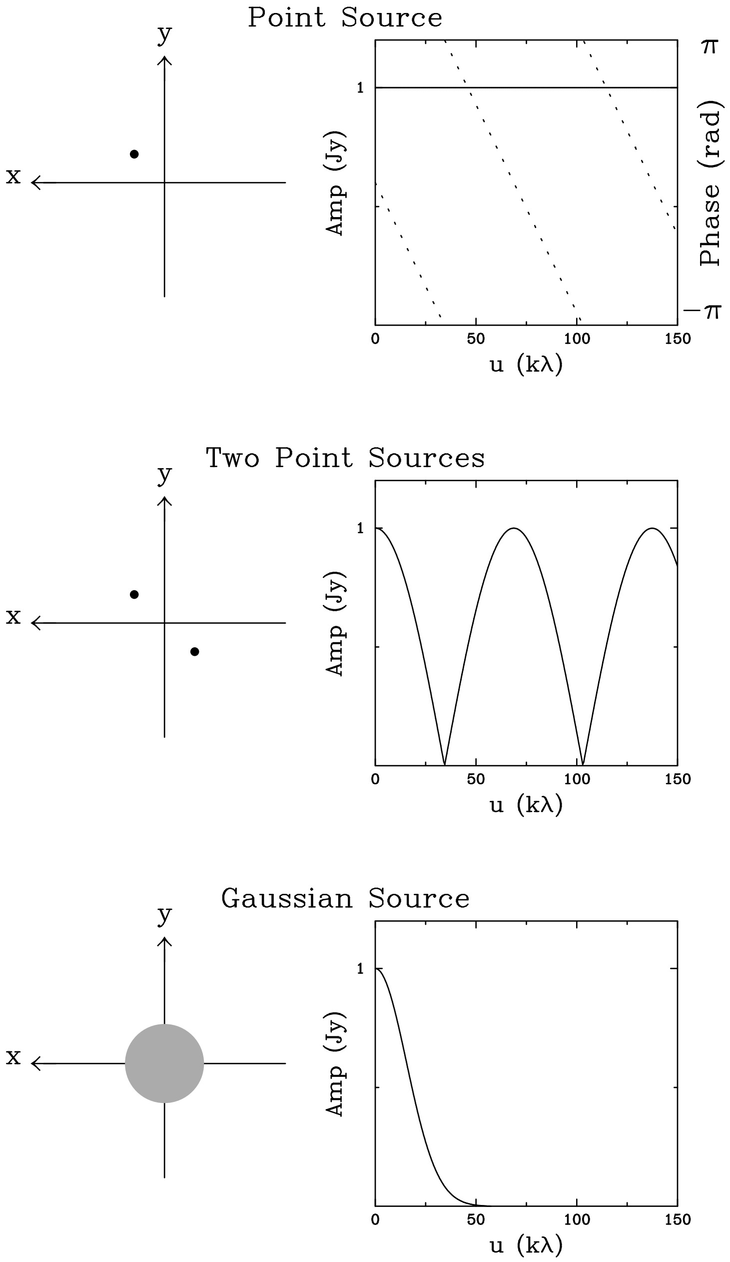

Fig. 2.3. Comparison of three emission structures in the sky plane and the Fourier transform plane.

regions of constructive and destructive interference in both the *u* and *v* directions. Since we are only showing the response with respect to *u*, the amplitude varies sinusoidally with a wavelength that is inversely proportional to the separation in x (in radians). The maximum is the addition of the two point sources, and the minimum is $\left|\frac{A1-A2}{A1+A2}\right|$, where A1 and A2 are the point source amplitudes. In the case shown, where the two amplitudes are equal, the two point sources can completely interfere to give zero amplitude.

In the bottom plot of Figure 2.3, the interferometer response is shown for a Gaussian source with a Full-Width-Half-Maximum (FWHM) of $5''$. Since the Fourier transform of a Gaussian is a Gaussian, the visibility amplitude curve is a Gaussian. The FWHM in *u,v* space is inversely proportional to the FWHM on the sky, $u_{\frac{1}{2}} = \ln(2)/(\pi x_{\frac{1}{2}})$; the larger the Gaussian on the sky, the narrower the Gaussian in the *u,v* plane.

2.4 Implications for Power-Law Emission

The standard model for circumstellar envelopes and disks is a power-law in temperature, density, and dust opacity (Adams, Shu, & Lada 1988; Beckwith et al. 1990; Adams, Emerson, & Fuller 1990; Keene & Masson 1990; Beckwith & Sargent 1991; Terebey, Chandler, & André 1993), resulting in a power-law emission distribution on the sky. Since we expect power-law emission from the objects to be studied in this thesis, this section will explore the relationship between power-law emission models and their Fourier transforms.

As shown in §2.2, a source brightness $B(x, y)$ has a visibility of

$$V(u, v) = \int_{-\infty}^{+\infty} \int_{-\infty}^{+\infty} B(x, y) e^{-i2\pi(ux+vy)} dx dy.$$

This assumes that the brightness distribution $B(x, y)$ is much smaller in extent than the primary beam pattern so that $P(x,y) \sim 1$. If we assume the emission is circularly symmetric,

$$B(x,y) \rightarrow B(r) \quad \text{and} \quad dxdy \rightarrow rdrd\theta$$

with

$$x = r\cos\theta \qquad y = r\sin\theta,$$

and in the *u,v* plane we can substitute u and v with *u,v* distance, β, and an angle, α.

$$u = \beta\cos\alpha \qquad v = \beta\sin\alpha.$$

We can rewrite the visibility as a function of β,

$$V(\beta) = \int_0^{+\infty} \int_0^{2\pi} B(r) e^{-i2\pi(\beta\cos\alpha\ r\cos\theta + \beta\sin\alpha\ r\sin\theta)} rdrd\theta.$$

Recombining some terms,

$$V(\beta) = \int_0^{+\infty} B(r) \int_0^{2\pi} e^{-i2\pi\beta\ r\left(\cos(\theta-\alpha)\right)} d\theta\ rdr.$$

The second term can be rewritten as a zeroth-order Bessel, which is by definition

$$J_0(z) = \frac{1}{2\pi}\int_0^{2\pi} e^{-iz\cos\theta} d\theta.$$

Since the integration is over 2π, the α is only a phase offset that does not affect the integration. So, we can rewrite the integral as,

$$V(\beta) = 2\pi \int_0^{+\infty} B(r) J_0(2\pi r\beta) rdr.$$

This is simply the Hankel transform of the brightness distribution.

Since we expect the brightness distribution to have a power-law form of $B(r) = B_o(\frac{r}{r_o})^{-A}$, the Hankel transform can be written as

$$V(\beta) = 2\pi \int_0^{+\infty} B_o r_o^A r^{1-A} J_0(2\pi r\beta) dr.$$

This integral has a solution of the form (Gradshteyn & Ryzhik 1980),

$$\int_0^{+\infty} x^\mu J_0(ax)dx = 2^\mu a^{(-\mu-1)}\,\frac{\Gamma(\frac{1}{2}+\frac{1}{2}\mu)}{\Gamma(\frac{1}{2}-\frac{1}{2}\mu)}$$

$$\text{for} \quad -1 < \mu < \frac{1}{2} \qquad a > 0.$$

Then,

$$V(\beta) = 2\pi B_o r_o^A\ 2^{(1-A)}\ (2\pi r\beta)^{(A-2)}\ \frac{\Gamma\Big(\frac{1}{2}+\frac{1}{2}(1-A)\Big)}{\Gamma\Big(\frac{1}{2}-\frac{1}{2}(1-A)\Big)}$$

for

$$\frac{1}{2} < A < 2.$$

So the Fourier transform of a spherically symmetric power-law brightness distribution ($B \propto r^{-A}$ for $\frac{1}{2} < A < 2$) is a power-law in the *u,v* plane ($V \propto \beta^{(A-2)}$).

2.4.1 Circumstellar Envelopes

As discussed for circumstellar envelopes in §1.6, we expect power-laws in temperature and density of the form $\rho \propto r^{-p}$ and $T \propto r^{-q}$ (e.g. Adams, Shu, & Lada 1988; Terebey, Chandler, & André 1993). Then, the three dimensional, optically thin envelope emission can be represented on the sky as approximately $B(r) \propto r^{-(p+q)+1}$ and the restrictions on the power law index A in §2.4 become $1.5 < p+q < 3$. The expected value for q in the optically thin case is 0.4 (e.g. Rowan-Robinson 1980; Wolfire & Cassinelli 1986), and the theoretical expected value for p is either 2 or $\frac{3}{2}$ (e.g. Larson 1969; Hunter 1977; Shu 1977; Terebey, Shu, & Cassen 1984); the restrictions on p+q are not violated. Thus, the power-law emission will have a power-law form of $V(\beta) \propto \beta^{(p+q-3)}$ in the *u,v* plane.

This formulation argues that an interferometer can easily measure the density power-law index, or at least the combination of p+q. However, the treatment assumes an infinite power-law. What sort of modification does an envelope with a finite outer boundary make to the solution? To address this question, we compare the result from the above derivation with simple radiative transfer numerical models. The simple model uses the same standard power-law description for the density and temperature, but it is truncated at an outer radius.

Figures 2.4 thru 2.6 show the results for a temperature power-law index of q=0.4 and density power-law indexes of p=1.0, p=1.5, and p=2.0 respectively. In each figure, the visibility amplitude is plotted for envelopes with outer radii of 1000, 2000, 3000, 6000, and 10000 AU (at an assumed distance of 140 pc). The 1000 AU envelope is at the top in each figure and the 10000 AU envelope is at the bottom. For comparison purposes, the expected slope for an infinite power-law $V(\beta) \propto \beta^{(p+q-3)} = \beta^{(p-2.6)}$ is shown by the line at the bottom of the figures.

As can be seen in these figures, the outer radius cutoff strongly affects the measured slope in the *u,v* plane. There is a very pronounced ringing in amplitude with *u,v* distance. This behavior can be explained in the Fourier plane. On the sky, a finite envelope can be described as an infinite power-law envelope multiplied with a circular step function. Thus, in the Fourier domain the power-law of the infinite envelope is convolved with the Fourier transform of the circular disk— a modified first-order Bessel function ($\sim J_1(\beta)/\beta$). The quasi-asymptotically sinusoidal behavior of the Bessel function gives rise to the ringing effect.

The amount of ringing depends upon the density power-law index (Figures 2.4 thru 2.6). The shallower the power-law index the more pronounced the Bessel function influence. A shallow density distribution has a significant amount of mass at the outer radii, giving it a well defined edge, leading to ringing in the Fourier plane due to the number of frequencies required to define the sharp edge.

In contrast, a steep density distribution (p=2.0) has very low density at large radii, and the edge is less important. Although a sharp edged envelope is probably not physical, this assumption will affect the modeling of the data.

The slope of the inner *u,v* plane is also dependent upon the outer radius. A small outer radius flattens out the inner *u,v* spacing amplitude– equivalent to a point source response. Once the envelope begins to become resolved, the power-law slope expected from the Hankel transform of an infinite power-law envelope is asymptotically approached with the ringing effect, due to the edge, superimposed. In fact, for a large envelope and steep density profile, there is very little difference in the slope of the truncated envelope and the infinite power-law (Figure 2.6).

Figures 2.7 and 2.8 present models where the envelopes were modified to have two density power-laws: an inner region (radii out to 500 AU or 3000 AU) with p=1.5 and an outer region (radii from the inner region out to 10000 AU) with p=2.0. In Figure 2.7, the slope resembles the p=2.0 slope for the shorter *u,v* distances, but once the 500 AU inner region is resolved, around 30 kλ, the slope converges toward the p=1.5 slope. The measured slope near the transition region is somewhere between the p=2 and p=1.5 slopes. In Figure 2.8, the inner region is resolved at very short *u,v* spacings, about 3 kλ, and the slope quickly resembles the p=1.5 slope.

Thus, interferometric measurements provide a very direct technique for probing the density structure in the envelope. However, there are many aspects of real envelope structure that complicate the practical application. With limited *u,v* sampling and signal-to-noise, the slope in the *u,v* plane can be significantly modified by the ringing effect due to a sharp edge or by the outer cutoff flattening the slope in the inner *u,v* plane. If the structure has a density profile described by two power-laws, one needs to have adequate sampling of both power-laws.

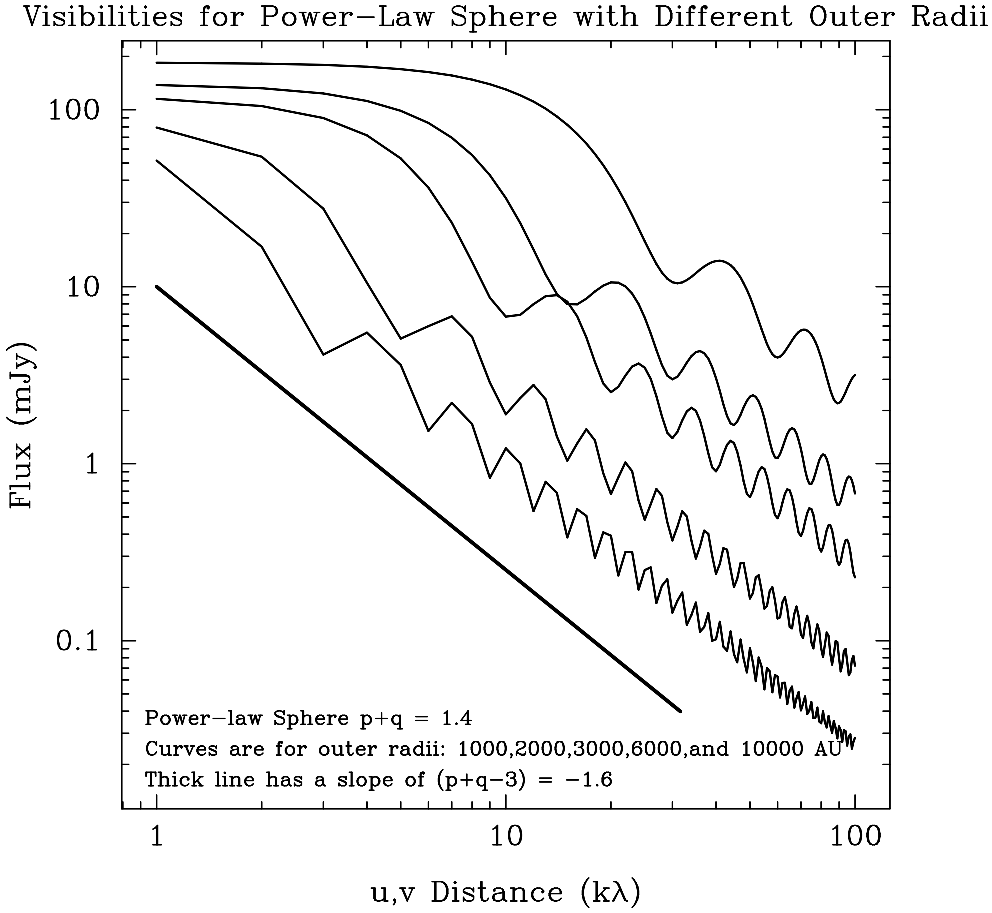

Fig. 2.4. Visibility of a power-law envelope with p=1.0 and various outer radii.

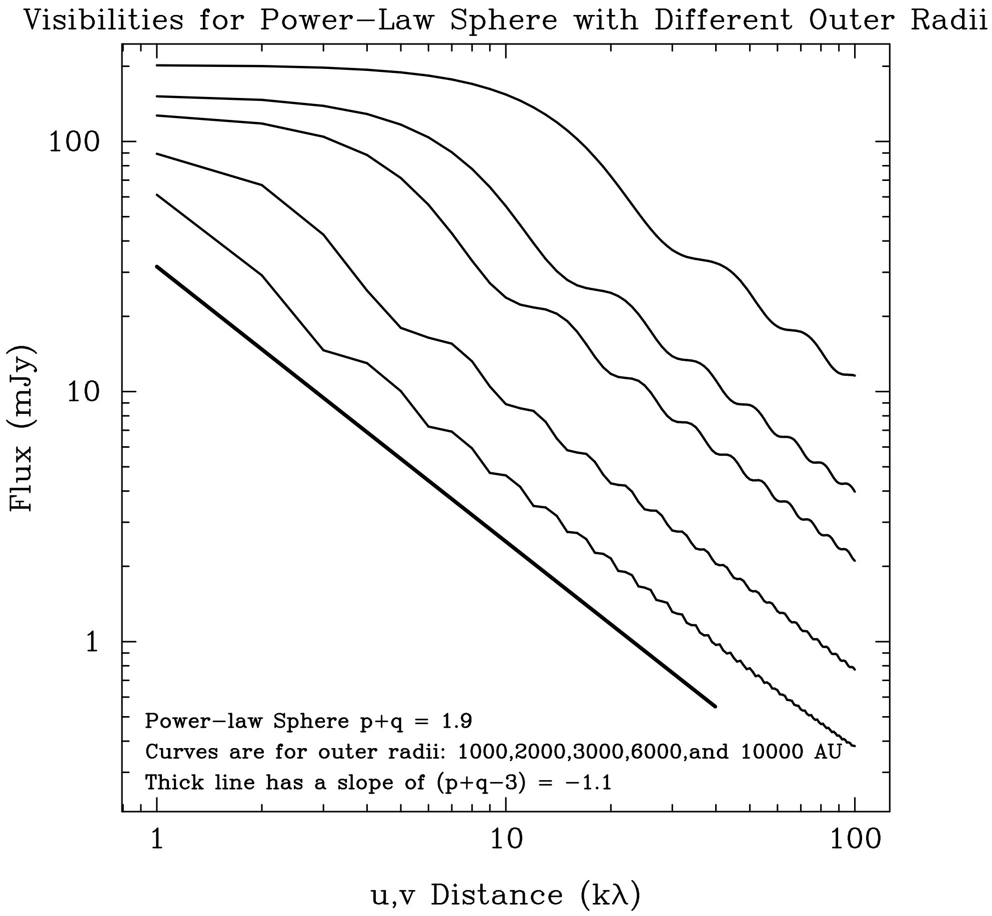

Fig. 2.5. Visibility of a power-law envelope with p=1.5 and various outer radii.

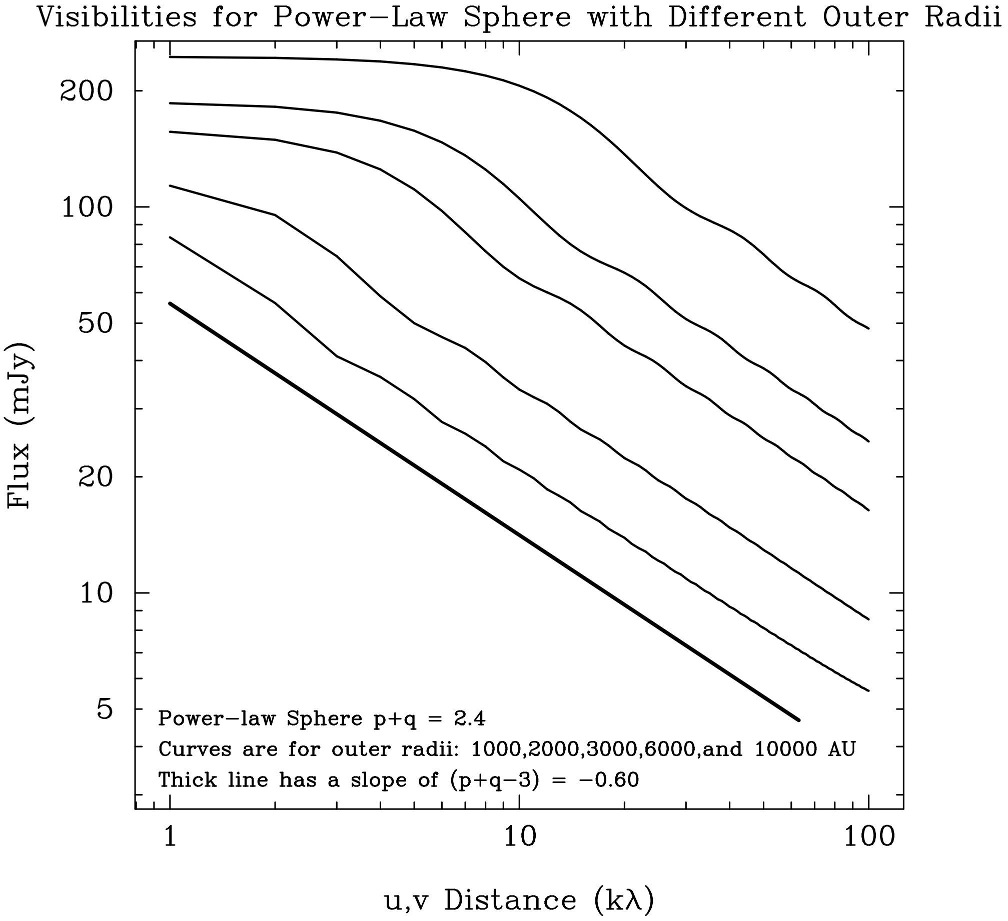

Fig. 2.6. Visibility of a power-law envelope with p=2.0 and various outer radii.

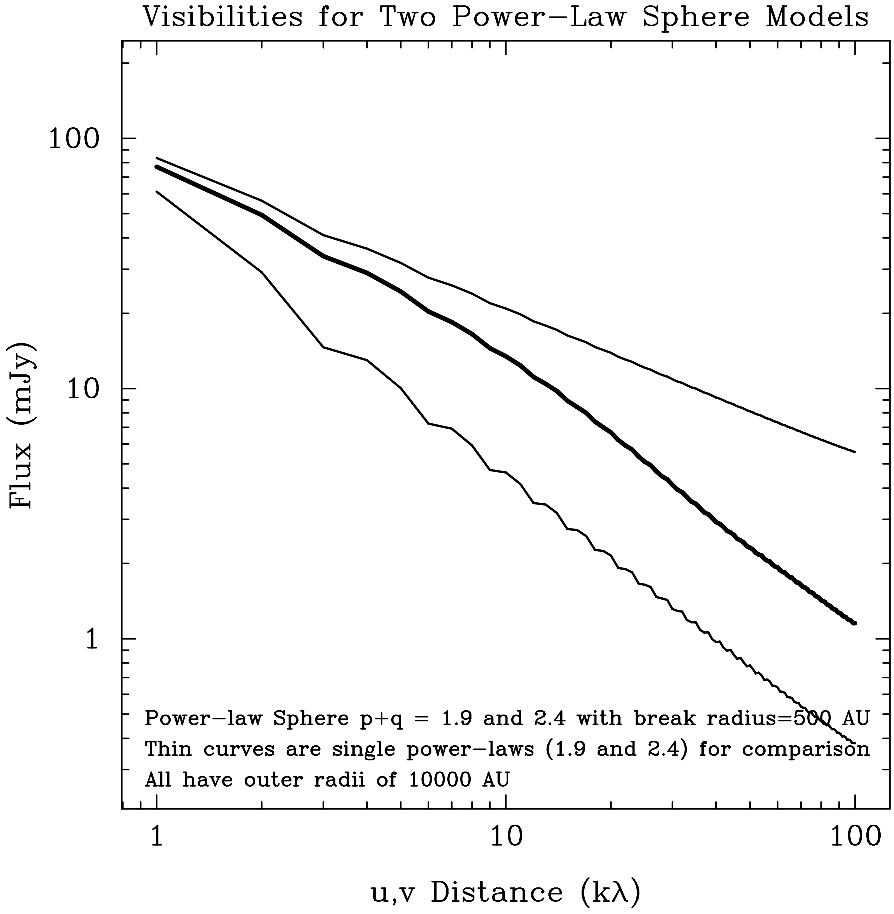

Fig. 2.7. Visibility of an envelope with two power-laws. The inner region (out to 500 AU) has a power-law of p=1.5 and an outer region (out to 10000 AU) with a power-law of p=2.0.

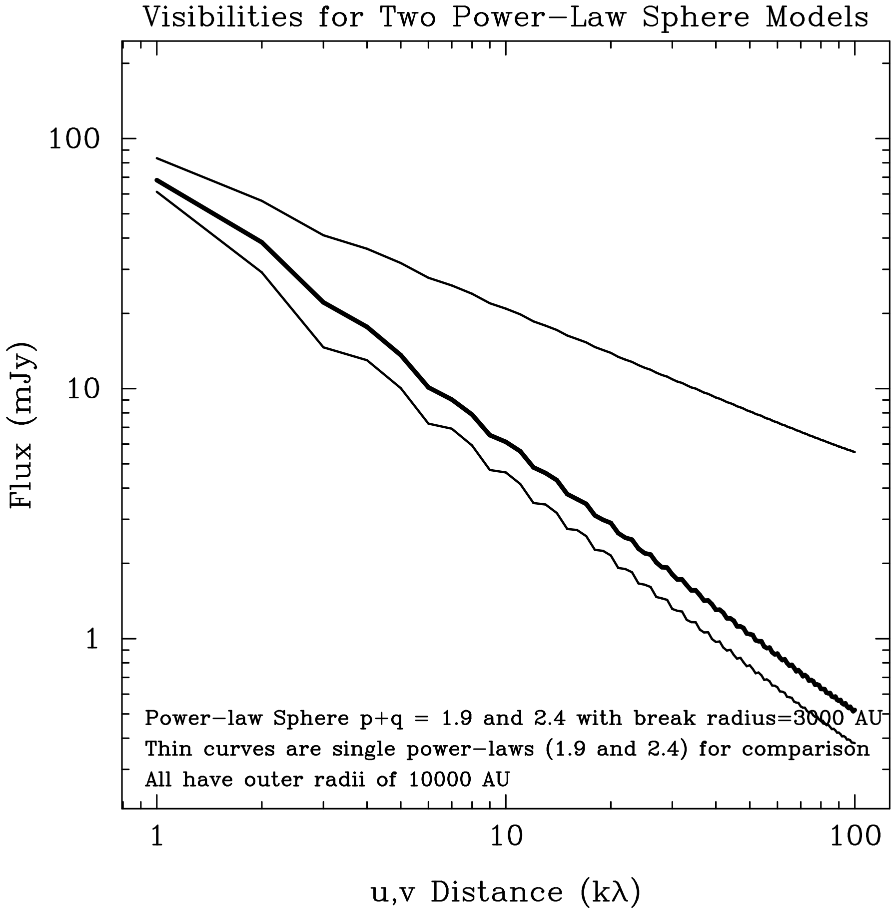

Fig. 2.8. Visibility of an envelope with two power-laws. The inner region (out to 3000 AU) has a power-law of p=1.5 and an outer region (out to 10000 AU) with a power-law of p=2.0.

The bottom line is that one needs good SNR data that covers a wide range of u,v distances, in order to accurately measure the density structures of envelopes.

2.4.2 And Circumstellar Disks

Although the discussion so far has been limited to circumstellar envelopes, the formalism is also valid for circumstellar disks. As discussed in §1.7, the standard model of circumstellar disks has power-law distributions in surface density and temperature of the form $\Sigma \propto r^{-p}$ and $T \propto r^{-q}$ (e.g. Adams, Shu, & Lada 1988; Beckwith et al. 1990). Then, the two dimensional, optically thin emission distribution on the sky for a face-on circumstellar disk is $B(r) \propto r^{-(p+q)}$.

As is shown in §2.4, the Fourier transform of a power-law brightness distribution is a power-law,

$$B(r) \propto r^{-A} \rightarrow V(\beta) \propto \beta^{(A-2)}$$

where

$$\frac{1}{2} < A < 2,$$

or for an optically thin face-on disk

$$B(r) \propto r^{-(p+q)} \rightarrow V(\beta) \propto \beta^{(p+q-2)}$$

where

$$\frac{1}{2} < p + q < 2.$$

The surface density power-law index (p) has a range of theoretical expectations spanning 0.5 to 1.75 for viscous disks (Cassen & Moosman 1981; Cassen & Summers 1983; Lin & Pringle 1990). A temperature power-law index of q = 0.75 is expected from both an active, self-luminous disk that is accreting and a passive disk that is only reprocessing the radiation from a central star

(Lynden-Bell & Pringle 1974). However, geometrical properties such as disk flaring and heating from a surrounding envelope, can strongly affect the temperature profiles; q values of 0.4 to 0.75 might be more realistic. Thus, the majority of expected $p + q$ combinations will be within this range. However, as shown in Figures 2.4 thru 2.8 for a finite envelope, the outer radius and power-law index of the surface density can affect the slope measured in the *u,v* plane. Since circumstellar disks (radii of $\sim$ 100 AU) are much smaller than circumstellar envelopes, it is much more vital to have sub-arcsecond resolution in order to accurately measure the slope of the visibility in the *u,v* plane. Again, the bottom line is that one needs good SNR data that covers a wide range of *u,v* distances. However, the above description of the circumstellar disk depends upon a face-on geometry, which is unlikely for a realistic circumstellar disk.

Chapter 3

High Resolution $\lambda = 2.7$ mm Observations of L1551 IRS5: A Protobinary System?

3.1 Introduction

First detected in an infrared survey of the L1551 cloud (Strom, Strom, & Vrba 1976), L1551 IRS5 is an archetypical young stellar system, with a strong bipolar molecular outflow (Snell, Loren, & Plambeck 1980), an optical jet (Mundt & Fried 1983), HH objects (Herbig 1974), and an envelope-disk structure in the surrounding material (Keene & Masson 1990). Located at a distance of 140 pc (Elias 1978) and exhibiting a luminosity of $\sim 28 L_{\odot}$ (Butner et al. 1991), L1551 IRS5 was one of the defining examples for Class I sources in the classification scheme of Adams, Lada, and Shu (1987) and has been used as an archetype in the current paradigm for single-star formation (Shu et al. 1993). But is it really a single-star system?

High resolution $\lambda = 2$ cm continuum observations of L1551 IRS5 show two compact sources with a separation of $\sim 0\farcs28$ (Bieging & Cohen 1985; Rodríguez et al. 1986) which have been interpreted as either a protobinary system (Bieging & Cohen 1985), or the inner ionized edges of a gas and dust toroid surrounding a single star (Rodríguez et al. 1986). The latter is the most widely accepted interpretation, but comparisons with $\lambda = 2$ cm emission from other young binary systems such as T Tau and Z CMa (Bieging, Cohen, & Schwartz 1984; Schwartz, Simon, & Zuckerman 1983), suggest that the binary interpretation is also viable.

Under the assumption that L1551 IRS5 is a single star system, Keene and Masson (1990) modeled $\lambda = 2.7$ mm interferometric observations to deduce the presence of a 45 AU radius circumstellar disk within an envelope. This envelope, which extends out ~1000 AU from IRS5, contains 0.1 to 1 $M_\odot$ of material (Ladd et al. 1995; Fuller et al. 1995). High resolution JCMT-CSO interferometric observations at $\lambda = 870$ μm resolved the compact central emission (Lay et al. 1994), and the emission was modeled as arising from an 80 AU radius Gaussian source, inferred to be an accretion disk around the young star.

In this chapter, we present sub-arcsecond imaging of the $\lambda = 2.7$ mm continuum emission from the L1551 IRS5 system. These observations re-open questions about the binarity of the system and the distribution of the surrounding material.

3.2 Observations and Data Reduction

L1551 IRS5 was observed in three array configurations of the 9-element BIMA Array[1] (Welch et al. 1996). The longest baselines were 1 km N-S and 900 m E-W, yielding a maximum projected baseline of 480 kλ (1.4km); the shortest baselines were limited by the antenna size of 6.1 m, yielding a minimum projected baseline of 2.2 kλ. This range in projected baselines provides images with a minimum resolution of $0\farcs3$, fully sampled to sizes as large as $60''$.

For the high resolution configuration (March 1, 1996), atmospheric phase fluctuations were tracked by switching the antennas between source, phase calibrator, and a nearby weak quasar on a two minute cycle. The usefulness of this quick switching technique has been demonstrated at the VLA (Holdaway & Owen 1995). The main phase calibrator (0530+135) was used to track rapid atmospheric phase fluctuations. The secondary quasar (0449+113) was used to track slow phase drifts due to the difference in airmass between the primary calibrator and source and, more importantly for this array, phase drifts due to uncertainties in baseline length.

The digital correlator was configured with two 700 MHz bands centered at 107 GHz and 109 GHz. The flux amplitude calibration assumed a flux of 6.8 Jy for 0530+135, as observed in the following month's compact array. The coherence of the atmosphere was checked on the quasars; the uncertainty in the amplitude calibration is 20%. Absolute positions in our map have uncertainty due to the uncertainty in the antenna baselines and the statistical uncertainty from the signal-to-noise of the observation. These two factors add in quadrature to give an absolute positional uncertainty of $0\farcs14$. The lower resolution data (acquired on October 3, 1996, February 2, 1997, and March 8, 1997) used 0530+135 to track phase variations and Mars for amplitude calibration.

The L1551 IRS5 data were imaged in four ways which stress structures present on different spatial scales. Figure 3.1 shows four maps: two with robust weightings of the visibilities (robust = 0.5 yielding a $3\farcs25 \times 3\farcs04$ beam and robust = -0.25 yielding a $1\farcs11 \times 0\farcs84$ beam), one with natural weighting of only

---

[1] The BIMA Array is operated by the Berkeley Illinois Maryland Association under funding from the National Science Foundation.

the high resolution A array data restored with the fitted "clean" beam ($0\farcs73 \times 0\farcs31$ beam), and one with the A array data restored with a circular $0\farcs31$ "clean" beam. The latter technique strongly emphasizes the high resolution information present in the A array *u,v* data. With maximum projected baselines ranging from 320 kλ to 480 kλ, the smallest fringe spacings in our dataset ranges from $0\farcs64$ to $0\farcs44$; hence information down to size scales of $0\farcs2$ to $0\farcs3$ is present in the *u,v* data. High resolution maps of the secondary quasar 0449+113, using the standard technique and using the $0\farcs31$ "clean" beam, were consistent with a point source.

3.3 Results

Figure 3.1a ($3''$ resolution) has a peak flux of 122$\pm$3 mJy beam^{-1}, and the integrated flux in a $8''$ box centered on the source is 162$\pm$6 mJy. A Gaussian fit to the image gives a deconvolved Gaussian source size of $1\farcs78 \times 1\farcs75$ and PA=68°. Figure 3.1b ($1''$ resolution) has a peak flux of 78$\pm$3 mJy beam^{-1}, and the integrated flux in a $3''$ box centered on the source is 143$\pm$10 mJy. A Gaussian fit to the image gives a deconvolved Gaussian source size of $0\farcs92 \times 0\farcs61$ and PA=157°. Figure 3.1c shows the map of the A array data alone restored with the Gaussian fitted clean beam. The peak flux in the map is 45$\pm$5 mJy beam^{-1}, and the integrated flux in a $1\farcs3$ box centered on the source is 75$\pm$11 mJy. Although it is not obvious in Figure 3.1c, over $\frac{1}{2}$ of the flux present in the lowest resolution map is now gone and the peak flux is roughly $\frac{1}{3}$ of that in Figure 3.1a. Despite the elongated "clean" beam, the remaining emission is clearly extended north-south in the CLEANed image; a Gaussian fit to the image gives a deconvolved Gaussian source size of $0\farcs53 \times 0\farcs32$ and PA=7.2°. Figure 3.1d shows the A array data restored with the circular $0\farcs31$ beam. The north-south

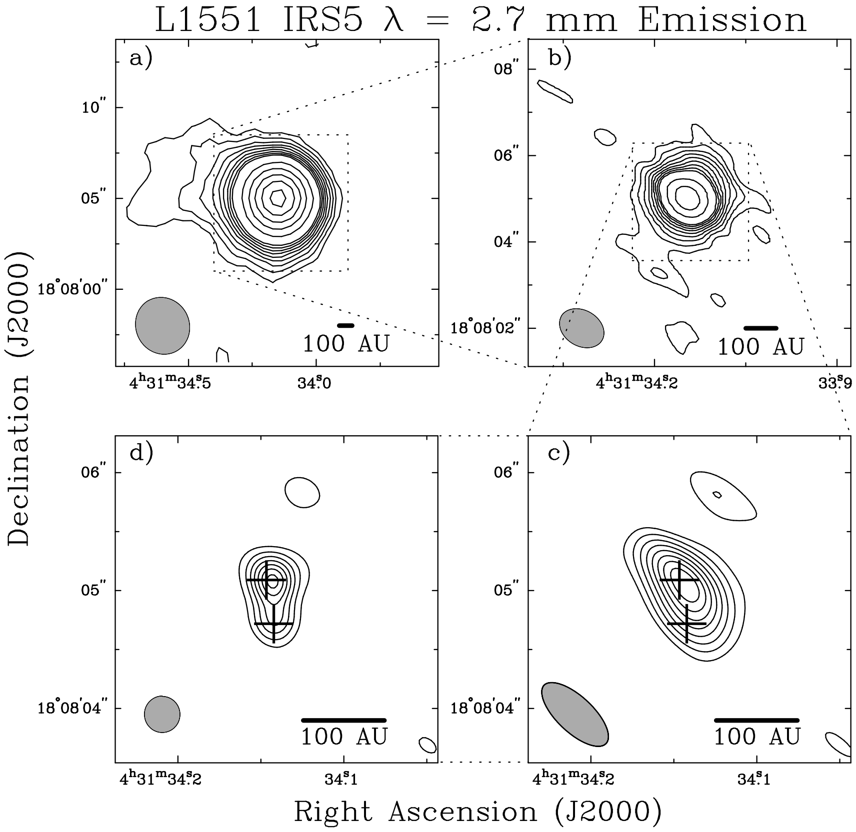

Fig. 3.1. $\lambda = 2.7$ mm maps of the continuum emission from L1551 IRS5. a) Map made with data from three arrays, Robust weighting of 0.5. The beam is $3.''25 \times 3.''04$ PA = 29°, and the RMS noise is 2.5 mJy beam^{-1}. The contours are -3,-2,2,3,4,5,6,7,8,9,10,15,20,25,30,35 times 3.3 mJy beam^{-1} (the RMS from Panel b). b) Map made with data from three arrays, Robust weighting of -0.25. The beam is $1.''11 \times 0.''84$ PA = 60°, and the RMS noise is 3.3 mJy beam^{-1}. The contours are the same as in Panel a. c) Naturally weighted map made from only the A array data. The beam is $0.''73 \times 0.''31$ PA=47° and the RMS is 4.5 mJy beam^{-1}. The contours are in steps of 1 σ starting at ± 2 σ. d) A array naturally weighted data, restored with a circular $0.''31$ beam. The contours and RMS are the same as in Panel c. The two crosses in Panels c and d mark the $\lambda = 1.3$ cm source positions from Koerner & Sargent 1997. The restoring beam in each panel is shown in the lower left-hand corner.

extension is obvious in this map and there is no hint of east-west extension. The peak flux is 38 mJy beam^{-1} corresponding to a brightness temperature of 41 K.

The images in Figure 3.1a and 3.1b emphasize the overall emission from the L1551 system. The reconstructions in Figure 3.1c and Figure 3.1d highlight the small scale emission which is more compact than expected for the disk size estimates of Keene and Masson (1990) and Lay et al. (1994). The compact emission is consistent with arising from two point sources, as seen at $\lambda = 2$ cm and $\lambda = 1.3$ cm (Rodríguez et al. 1986; Koerner & Sargent 1997). A two Gaussian fit to the $\lambda = 2.7$ mm emission in Figure 3.1d yields the following positions hereafter labeled IRS5 A and IRS5 B: IRS5 A: $\alpha(\mathrm{J2000}) = 04^h31^m34^s.143$, $\delta(\mathrm{J2000}) = 18^\circ08'05''.09$ and IRS5 B: $\alpha(\mathrm{J2000}) = 04^h31^m34^s.141$, $\delta(\mathrm{J2000}) = 18^\circ08'04''.74$. These positions agree to within $0''.05$ with the $\lambda = 1.3$ cm source positions of Koerner and Sargent (1997). The separation of the two sources is $0''.35$, corresponding to 49 AU. Both sources have deconvolved sizes of $\leq 0''.3$. A two point source fit yields flux densities of 45±6 mJy for IRS5 A and 23±6 mJy for IRS5 B. The total flux density in the compact sources is then 68±9 mJy.

3.4 Comparisons with Centimeter High Resolution Data

High resolution centimeter wavelength images of L1551 IRS5 show two point-like sources and an extended jet (Bieging & Cohen 1985). The jet is detected only at long centimeter wavelengths; the two point sources dominate the flux at shorter wavelengths. The $\lambda = 2$ cm flux densities are 1.2 mJy for IRS5 A and 0.93 mJy for IRS5 B (Rodríguez et al. 1986). Recent VLA observations also resolved the two sources at $\lambda = 1.3$ cm (Koerner & Sargent 1997) and yielded flux densities of

2.0±0.2 mJy and 1.5±0.2 mJy, respectively. The spectral indices between $\lambda = 2.0$ and 1.3 cm are then $\alpha_A \sim 1.25$ and $\alpha_B \sim 1.04$, consistent with $\alpha \sim 1$ estimated by Bieging and Cohen (1985). Extrapolating to 109 GHz, this emission could contribute as much as ~14.4 mJy and ~7.8 mJy, respectively, to the observed fluxes. Hence, the $\lambda = 2.7$ mm flux is dominated by dust emission.

The proposal of Rodríguez et al. (1986) that the $\lambda = 2$ cm emission traces the ionized inner edge of a larger dusty torus is not consistent with the observed compact $\lambda = 2.7$ mm emission. Since the millimeter emission directly probes the dust, we should easily see the torus in our high resolution maps. If there were a torus, the $\lambda = 2.7$ mm emission would extend beyond the $\lambda = 2$ cm sources and, in fact, peak outside of them. The binary interpretation of Bieging & Cohen is consistent with our image if the $\lambda = 2.7$ mm emission arises from circumstellar disks within the binary system, while the $\lambda = 2$ cm emission traces ionized gas associated with stellar winds or jets.

3.5 The Structure of the L1551 IRS5 System

Combining all observations to date, the L1551 IRS5 system consists of three main circumstellar components: a large-scale envelope (Keene and Masson 1990; Ladd et al. 1995), a disk or extended structure with a size scale of $\sim 1''$ (Lay et al. 1994; Keene and Masson 1990), and an inner binary system as argued in §3.4. How do these components fit together? To answer this question, we compare our *u,v* data binned in annuli with simulated observations of models for the system, binned similarly. In the following subsections we discuss each component and derive characteristic masses.

3.5.1 Binary Circumstellar Disks

Figure 3.2a compares our *u,v* data with the Gaussian model from Lay et al. (1994) scaled to match the $\lambda = 2.7$ mm flux at 50 kλ. Above 100 kλ, the Gaussian model is resolved out and does not fit the data; below 20 kλ the data diverge from the model due to flux from the envelope. Figure 3.2b shows a two point source model with the separation and amplitudes given in §3.3. The two point sources beat together to cause the variations in flux seen past 100kλ. The proposed binary disk system is evident only in our data; its separation is too small to be resolved in the data of Lay et al. (1994) or Keene and Masson (1990). In fact, due to the small angular size and the embedded nature of the binary system, the properties of the proposed disks are poorly constrained by observations to date. The projected separation and extent of the $\lambda = 2.7$ mm emission suggests a maximum outer radius of 25 AU for the disks. To estimate the masses of the disks, we assume a standard power-law disk with parameters characteristic of the HL Tau disk, $T_{disk} = 330(\frac{1AU}{r})^{0.5}$ and $\Sigma_{disk} \propto r^{-1}$ (Mundy et al. 1996; Beckwith & Sargent 1991). For dust properties, we adopt κ=0.1($\frac{\nu}{1200\ GHz}$) cm^2 g^{-1}, which is consistent with other recent works (e.g. Osterloh and Beckwith 1995; Ohashi et al. 1991; Beckwith & Sargent 1991). With these assumptions, the disk masses are $M_A \sim 0.024\ M_\odot$ and $M_B \sim 0.009\ M_\odot$.

3.5.2 The Envelope

The excess emission in our robust weighted maps (Figures 3.1a and 3.1b) compared to our highest resolution map (Figure 3.1d) and the rise in flux on baselines shorter than 15 kλ (Figure 3.2), are due primarily to the extended envelope. Our flux densities in the larger beams are consistent with previous measurements at similar resolutions: Keene and Masson (1990) find a peak flux

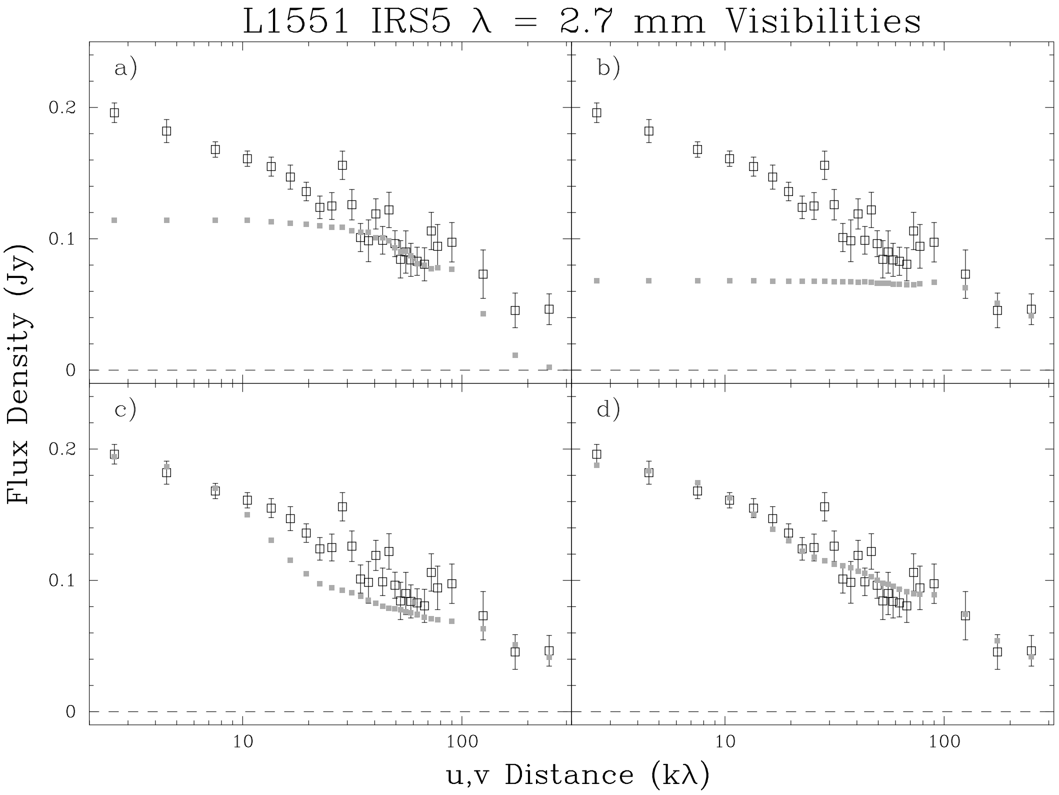

Fig. 3.2. The measured $\lambda = 2.7$ mm visibilities binned in annuli (open squares) compared with different model visibilities (gray, closed squares). a) The Lay et al. (1994) model Gaussian scaled to match the $\lambda = 2.7$ mm fluxes around 50 kλ. b) Two point source model constrained by fitting Figure 3.1d. c) Characteristic model fit with an envelope (0.44 $M_\odot$, $\rho(r) \propto r^{-1.5}$, $T(r) \propto r^{-0.5}$, and 1300 AU radius) and the two point sources from Panel b. d) Characteristic fit for a model with an envelope (0.28 $M_\odot$, $\rho(r) \propto r^{-1.5}$, $T(r) \propto r^{-0.5}$, and 1100 AU radius), a Gaussian (30 mJy, $1\farcs2 \times 0\farcs7$ PA = 160°), and the two point sources from Panel b.

of 130 mJy beam^{-1} at $\lambda = 2.73$ mm in a $2''.6$ beam and a total flux of 150 mJy; Ohashi et al. (1996) measure a total flux of 160 mJy at $\lambda = 2.73$ mm using a $4''.5$ beam. Our *u,v* data in Figure 3.2 and Figure 2 of Keene and Masson (1990), show similar fluxes around 10 kλ, but our data has 20% to 30% less flux from 40 kλ to 70 kλ. These differences are within the calibration uncertainties.

The differences in flux densities at different resolutions, or equivalently the drop in flux density with *u,v* distance, can be used to estimate the properties of the envelope. Our data are broadly consistent with the envelope parameters determined by Ladd et al.(1995) and Fuller et al.(1995). Fitting the drop in flux between 2.6 kλ and 15 kλ with a power-law envelope model ($\rho(r) \propto r^{-1.5}$ and $T(r) \propto r^{-0.5}$) combined with the two point source model from §3.5.1, reasonable results are obtained for an envelope mass of ~0.44 $M_\odot$, an outer radius of ~1300 AU, and an inner envelope radius of 30 AU (Figure 3.2c). Steeper envelope density laws ($\rho(r) \propto r^{-2}$) also fit the data with a characteristic mass and outer radius of 0.43 $M_\odot$ and 1800 AU, respectively.

3.5.3 The Circumbinary Structure

Finally, an intermediate-sized structure, perhaps a circumbinary disk such as seen around GG Tau (Dutrey, Guilloteau, Simon 1994) or a "pseudo-disk" (Galli and Shu 1993), is needed to account for the structure resolved by Lay et al. (1994) and the compact structure deduced by Keene and Masson (1990). In our data, this structure is evident as the excess emission between 30 kλ and 90 kλ in Figure 3.2c. As shown in Figure 3.2d, this excess can be fitted with a Gaussian model consistent with that of Lay et al. ($1''.2 \times 0''.7$ PA = 160°) with a flux of 30 mJy plus an envelope model with a mass of 0.28 $M_\odot$ ($\rho(r) \propto r^{-1.5}$) and a radius of 1100 AU. The parameters of the envelope and the circumbinary structure are interdependent and hence only crudely determined. If the circumbinary structure has dust properties similar to the envelope parameters in §3.5.2, the circumbinary structure has a rough mass of 0.04 $M_\odot$.

To test the consistency of the above model with the Lay et al. (1994) data, we fit two different source structures to their $\lambda = 870$ μm data: a single elliptical Gaussian (a single circumstellar disk) and a single elliptical Gaussian with two central point sources (a circumbinary disk with two small circumstellar disks), following the fitting procedure of Lay et al. (1994; also see Lay 1994). The model did not include envelope emission since the JCMT-CSO baselines ranged from 50 kλ to 200 kλ, where the envelope emission is completely resolved out. The single elliptical Gaussian model fits the $\lambda = 870$ μm data very well, with parameters comparable to those found by Lay et al. (1994). The addition of two point sources to the single Gaussian model produces as good a fit as the single Gaussian model, but the FWHM of the Gaussian increases slightly. Hence, the data cannot distinguish between the single Gaussian and single Gaussian with point source models. If the circumbinary material is optically thick at $\lambda = 870$ μm, the Lay et al. data would not even see the embedded circumstellar disks. If the circumbinary material is not optically thick, the Lay et al. data place a limit on the flux from the circumstellar disks: at a 95% confidence level the circumstellar disks emit ≤ 1.3 Jy at $\lambda = 870$ μm.

3.6 Young Binary systems

Our data present the first direct detection of a close, embedded binary system. Proposed wider binary systems have been identified among embedded sources, e.g. IRAS 16293-2422 (Wootten 1989), NGC 1333 IRAS4 (Sandell et al. 1991; Lay et al. 1995), and L1527 (Fuller, Ladd, & Hodapp 1996), but the number of such systems is actually quite small compared to the number of known embedded sources. Surveys of pre-main sequence (PMS) stars find that binary systems are at least as common among young visible stars as among main-sequence stars (Simon et al. 1992; Ghez, Neugebauer & Matthews 1993; Leinert et al. 1993; Reipurth & Zinnecker 1993); so binaries should be common among young, deeply embedded systems. That they have not often been seen is probably due to the lack of sub-arcsecond resolution observations which are necessary to resolve close binaries. The separation of the L1551 IRS5 system is near the median separation for main sequence binaries (~30 AU, Duquennoy & Mayor 1991). The low detection rate of wide embedded binaries is in rough agreement with the fraction of main sequence binaries with separations between 300 and several 1000 AU.

L1551 IRS5 also ranks as one of the few close binary systems with significant dust emission associated with both components. Submillimeter wavelength surveys have generally found lesser amounts of dust emission associated with PMS binary systems than with young single stars systems (Simon et al. 1992, 1995). In a statistical comparison of binaries and single stars, Jensen, Mathieu & Fuller (1996) found that binaries with separations $\leq$ 50-100 AU statistically have lower submillimeter fluxes than wider binaries, but wide binaries are indistinguishable from single stars; hence, the L1551 IRS5 system may be unusual. However, these studies concentrate on T Tauri stars and exclude the youngest sources, Class I or younger. It is possible that embedded close binaries, which are still accreting mass, have substantial circumstellar or circumbinary disks which disappear later when the envelope is no longer feeding-in material.

3.7 Conclusions

Sub-arcsecond $\lambda = 2.7$ mm observations of L1551 IRS5 have resolved a compact central structure, which is most plausibly interpreted as a young binary system. The $\lambda = 2.7$ mm continuum emission shows two peaks which are similar, in absolute position and separation, to the free-free emission observed at centimeter wavelengths. Our interpretation is that we are detecting thermal dust emission from small disks around the individual stars in a binary system and that the centimeter emission arises in the associated stellar winds. We propose that the L1551 IRS5 system is composed of two circumstellar disks, located inside a circumbinary structure, embedded in a large-scale envelope. Simple modeling yields masses for these components: circumstellar disk masses of 0.024 $M_\odot$ and 0.009 $M_\odot$ for the northern and southern sources respectively, a circumbinary structure mass of 0.04 $M_\odot$, and an envelope mass of 0.28 $M_\odot$. The binary separation for L1551 IRS5 is about 50 AU, close to the median separation for main sequence binaries. The small number of young embedded binaries detected to date probably reflects the inadequate angular resolution available in the earlier studies, rather than an intrinsic sparsity of binaries.

Chapter 4

Unveiling the Envelope and Disk: A Sub-arcsecond Survey

4.1 Introduction

Young stellar systems exhibit excess infrared and millimeter emission that arises primarily from circumstellar dust in two basic evolutionary structures: envelopes and disks. The current observations and theories of star formation (e.g. Larson 1969; Penston 1969; Shu 1977; Cassen & Moosman 1981; Lada & Wilking 1984; Adams, Lada, & Shu 1987; Shu et al. 1993; André, Ward-Thompson, & Barsony 1993) outline an evolutionary sequence that begins with a density enhancement which quasi-statically contracts to form a centrally concentrated core. The core then gravitationally collapses forming an infall region which feeds a central protostar and a surrounding disk supported by centrifugal forces. Initially, the envelope contains most of the mass, but as the system evolves, the disk and protostar grow, and the disk becomes a significant mass reservoir. In time, the prenatal envelope is depleted of material and progressively blown away by the powerful stellar outflow, revealing the young star and disk system. Detailed modeling of young stellar objects has shown that the observed excess infrared through millimeter wavelength emission can be reproduced by thermal dust emission from a combination of a large-scale envelope, a spatially thin disk, and a central star (Adams, Lada, & Shu 1987; Kenyon & Hartmann 1987; Bertout, Basri, & Bouvier 1988; Calvet et al.1994) or, in some cases, by just a disk and central star (Beckwith et al. 1990; Osterloh & Beckwith 1995; Dutrey et al. 1996).

Surveys of main-sequence stellar systems find that most stars are in binary or multiple systems (Duquennoy & Mayor 1991) with the separation distribution ranging from a few $R_{\odot}$ to 10^4 AU with the probability distribution peaking around 30 AU. Recent surveys of the nearby star-forming regions of Taurus and Ophiuchus find that the occurrence of binaries in the young visible systems is about twice as common as among main-sequence stars (Simon et al. 1992; Ghez, Neugebauer, &, Matthews 1993; Leinert et al. 1993; Reipurth & Zinnecker 1993; Ghez, White, & Simon 1997). How is the above star formation process altered to form binary systems, and how does the younger, deeply embedded system binary occurrence compare to the young visible systems?

In this paper, we present a $\lambda = 2.7$ mm continuum survey of 24 nearby Young Stellar Objects that represent a sample of young stellar systems at various stages of evolution. The survey highlights the large dynamic range of u,v spacings available with the Berkeley-Illinois-Maryland Association (BIMA) millimeter Array— covering both the largest and smallest u,v spacings currently available at $\lambda = 2.7$ mm. With a combination of low and high resolutions, we are able to map the envelopes of the embedded sources and resolve out the large-scale structure in order to peer inside the envelopes and image the central regions. The purpose of this paper is to present our images with the discussion focusing on differences and similarities between the various evolutionary stages and several broad trends in the data. In additional papers, we will discuss individual sources in detail and extensively model the emission structures of these sources as arising from extended envelopes, circumstellar disks, and circumbinary disks.

4.2 Sample, Observations, and Mapping

4.2.1 Sample

The goal of the survey was to image a broad range of young stellar systems at sub-arcsecond resolution. We concentrated on known, bright, and nearby sources which were most likely to produce high dynamic range images. The criteria for selecting the sample were: (1) for the best sensitivity to solar-system-sized spatial scales, we focused on the closest sources ($\leq$ 350 pc); (2) to insure sufficient surface brightness at sub-arcsecond resolution, we chose among the brightest sources in the nearby star forming regions; (3) to survey an assortment of evolutionary stages, our sample included the youngest, most deeply embedded sources (Class 0), as well as the typical optical T Tauri stars (Class I/II); (4) finally, to achieve the best map fidelity, we required that the sources have both a bright phase reference calibrator and a weaker point source calibrator nearby on the sky. This combination of criteria introduces two strong biases in our sample: (1) we favor bright millimeter sources which should be systems with more circumstellar material than average (e.g. Beckwith et al. 1990) and (2) as a result of our distance limit, our sources are drawn from just the three local clouds—Taurus, Ophiuchus, and Perseus. Table 1 lists the sources, adopted distances, whether they are optically visible (in this category we also include objects which are visible in the near-infrared) or embedded, adopted SED class, main calibrator, and secondary calibrator. The distance to the Perseus objects has been in dispute

Table 4.1. Source List

Source	Distance (pc)	Optical/IR or Embedded	Class	Main Calibrator	Secondary Calibrator	Refs
L1448 IRS3 A	300	Embedded	0	3C111	0336+323	2
L1448 IRS3 B	300	Embedded	0	3C111	0336+323	2
L1448 IRS3 C	300	Embedded	0	3C111	0336+323	2
NGC1333 IRAS2 A	350	Embedded	0	3C111	0336+323	2
NGC1333 IRAS2 B	350	Embedded	0	3C111	0336+323	2
SVS 13 A1	350	Optical/IR	···	3C111	0336+323	2
SVS 13 A2	350	Embedded	···	3C111	0336+323	2
SVS 13 B	350	Embedded	···	3C111	0336+323	2
SVS 13 C	350	Embedded	···	3C111	0336+323	2
NGC1333 IRAS4 A1	350	Embedded	0	3C111	0336+323	2
NGC1333 IRAS4 A2	350	Embedded	0	3C111	0336+323	2
NGC1333 IRAS4 B	350	Embedded	0	3C111	0336+323	2
NGC1333 IRAS4 C	350	Embedded	···	3C111	0336+323	2
DG Tauri	140	Optical/IR	II	3C111	0431+206	1
DG Tauri B [a]	140	Optical/IR	I	3C111	0431+206	1
L1551 IRS5	140	Optical/IR	I	3C111	0336+323	1

Table 4.1—Continued

Source	Distance (pc)	Optical/IR or Embedded	Class	Main Calibrator	Secondary Calibrator	Refs
HL Tauri	140	Optical/IR	II	0530+135	0431+206	1
GG Tauri	140	Embedded	II	0530+135	0431+206	1
GM Aurigae	140	Optical/IR	II	3C111	3C123	1
VLA 1623	160	Embedded	0	1733-130	1625-254	3
IRAS 16293-2422 A	160	Embedded	0	1733-130	1625-254	3
IRAS 16293-2422 B	160	Embedded	0	1733-130	1625-254	3

[a] DG Tauri B observed near the FWHM of primary beam.

References. — (1) Elias 1978; (2) Herbig & Jones 1983; (3) Whittet 1974 lately, 350 pc (Herbig & Jones 1983) and more recently 220 pc (Cernis 1990). We adopt the previous value, allowing an easier comparison to earlier works.

The frequency of multiple systems will be addressed in §4.6, but the number of objects in the embedded source group is misleading since all of the observed embedded sources are in multiple systems. For example, the Perseus objects include 13 sources which were mapped in only 4 pointings, whereas in the optical group, only DG Tauri and DG Tauri B (which is an embedded object not thought to be related to DG Tauri except by projected proximity; Jones & Cohen 1986) were mapped in the same observation.

4.2.2 Observations

All sources were observed in three configurations of the 9-element BIMA Array[1] (Welch et al. 1996). The observations were acquired from 1996 May to 1998 March. The digital correlator was configured with two 700 MHz bands centered at 106.04 GHz and 109.45 GHz. The $C^{18}O(1-0)$ line was observed simultaneously; those results will be discussed elsewhere. The two continuum bands were checked for consistency, then combined into the final images. The system temperatures during the observations ranged from 150-700 K (SSB).

In the compact C array (typical synthesized beam of $\sim 8''$), the shortest baselines were limited by the antenna size of 6.1 m, yielding a minimum projected baseline of 2.1 kλ and good sensitivity to structures as large as $\sim 50''$. In the mid-sized B array (typical synthesized beam of $\sim 2''$) the observations are sensitive to structures as large as $\sim 10''$. In the long baseline A array (typical

---

[1] The BIMA Array is operated by the Berkeley Illinois Maryland Association under funding from the National Science Foundation.

synthesized beam of $\sim 0\farcs6$), the longest baselines were typically 450 kλ with a sensitivity to structures as large as $\sim 3''$. The combination of these three arrays provides a well sampled *u,v* plane from 2.1 kλ out to 400 kλ.

The uncertainty in the amplitude calibration is estimated to be 20%. In the B and C arrays, the amplitude calibration was boot-strapped from Mars. In the A Array, amplitude calibration was done by assuming the flux of the quasar 3C273 to be 18.8 Jy at the end of 1996 October, 23.0 Jy at the end of 1996 November, and 27.0 Jy until the end of 1997 January. Absolute positions in our map have uncertainty due to the uncertainty in the antenna baselines and the statistical variation from the signal-to-noise of the observation. These two factors add in quadrature to give a typical absolute positional uncertainty of $0\farcs1$ in the highest resolution maps.

The A array observations required careful phase calibration. On long baselines, the interferometer phase is very sensitive to atmospheric fluctuations. We employed rapid phase referencing; the observations switched between source and phase calibrator on a two minute cycle, to follow the atmospheric phase (Holdaway & Owen 1995; Looney, Mundy, & Welch 1997). To monitor the coherence of the atmosphere, or the "seeing", we included a nearby weaker quasar in the observation cycle. This quasar was imaged along with the target source as a check of the point source response and for accurate image registration. In the observations presented here, the secondary quasar was always a point source within statistical uncertainties.

4.2.3 Mapping

The observational data span *u,v* distances from 2.1kλ to 450kλ, providing information of the brightness distribution on spatial scales from $0\farcs4$ to $50''$. In order to display this information in the image plane, we have mapped the emission with four different *u,v* weighting schemes which stress structures on spatial scales of roughly $5''$, $3''$, $1''$, and $0\farcs6$. These resolutions were typically obtained with natural weighting, robust weighting (see Briggs 1995) of 1.0, robust weighting of 0.0, and robust weighting of -0.5, respectively.

4.3 Results

The $\lambda = 2.7$ mm continuum images from the survey are shown in Figures 1 through 16. In each figure, the four panels display the same multi-configuration data with different *u,v* weighting schemes to emphasize structures on size scales comparable to the synthesized beam. Table 2 lists, at each resolution, the peak flux, the integrated flux, and the box used for the integrated flux measurement. The error bars on the flux measurements represent the statistical uncertainties.

In Figure 17, the source fluxes are presented in a plot comparing the total integrated flux to the ratio of the visibility amplitude at two specific fringe spacings. The horizontal axis is the integrated flux of each object taken from Table 2 and adjusted to the distance of the Taurus Molecular Cloud (140 pc). For the vertical axis, the *u,v* data were binned in annuli stretching from 2.2 kλ to 7.8 kλ and from 22 kλ to 78 kλ, corresponding to average spacings of 5 kλ and 50 kλ for the distance of Taurus. The vertical axis plots the ratio of the vector averaged amplitudes in the two bins or 5kλ/50kλ. In order for the ratio to consistently probe the same spatial scales for all objects, we adjusted the bin range to take into account the various distances: for ρ Ophiuchi we used annuli averaging of 5.7 kλ and 57 kλ, respectively, and for Perseus we used annuli averaging 12.5 kλ and 125 kλ, respectively. This ratio provides a measure of the relative emission on spatial scales of ~6000 AU and ~600 AU and quantitatively measures the

Table 4.2. Source Flux

Source	Panel	Peak Flux Jy/beam	Integrated Flux Jy	Box Size
L1448 IRS3 A	(a)	26.5±1.6	23.1± 2.6	11.″2 × 6.″3
	(b)	14.5±1.5	26.7± 3.3	8.″3 × 5.″8
	(c)	6.8±1.6	19.3± 3.7	2.″3 × 2.″9
	(d)	<6.7	···	···
L1448 IRS3 B	(a)	101.5±1.6	134.6± 3.9	17.″0 × 9.″8
	(b)	84.9±1.5	135.6± 4.8	11.″0 × 9.″0
	(c)	41.1±1.6	135.2± 6.7	4.″5 × 4.″9
	(d)	22.5±2.3	115.7± 9.5	2.″8 × 2.″4
L1448 IRS3 C	(a)	14.9±1.6	31.7± 4.1	10.″7 × 17.″0
	(b)	11.7±1.5	31.9± 3.7	5.″0 × 12.″0
	(c)	9.8±1.6	14.3± 3.2	2.″5 × 2.″0
	(d)	8.7±2.3	8.7± 2.3	0.″7 × 0.″5
N1333 IRAS2A	(a)	46.5±1.3	82.8± 4.0	16.″4 × 16.″3
	(b)	36.2±1.2	74.4± 4.0	11.″0 × 12.″0
	(c)	22.3±1.7	36.1± 4.4	2.″9 × 2.″2
	(d)	18.4±2.7	22.4± 4.8	1.″4 × 0.″9
N1333 IRAS2B	(a)	21.3±1.3	27.7± 3.2	12.″8 × 13.″0
	(b)	19.6±1.2	24.4± 2.7	6.″6 × 9.″2
	(c)	18.9±1.7	24.7± 3.5	1.″9 × 2.″2
	(d)	16.9±2.7	24.3± 5.1	1.″2 × 1.″2

Table 4.2—Continued

Source	Panel	Peak Flux Jy/beam	Integrated Flux Jy	Box Size
SVS 13 A	(a)	47.3±1.1	101.3± 4.2	$26\farcs0 \times 15\farcs0$
	(b)	37.4±1.1	100.3± 4.7	$20\farcs7 \times 10\farcs2$
	(c)	19.2±1.5	38.7± 4.1	$2\farcs9 \times 2\farcs9$
	(d)	11.0±2.2	38.0± 6.6	$1\farcs7 \times 2\farcs2$
SVS 13 B	(a)	52.0±1.1	123.0± 4.5	$31\farcs5 \times 14\farcs0$
	(b)	41.7±1.1	110.4± 3.7	$10\farcs1 \times 13\farcs0$
	(c)	25.3±1.5	41.4± 3.6	$2\farcs2 \times 3\farcs0$
	(d)	19.4±2.2	48.2± 6.6	$1\farcs5 \times 2\farcs5$
SVS 13 C	(a)	11.7±1.1	21.0± 2.5	$14\farcs0 \times 10\farcs0$
	(b)	9.6±1.1	19.8± 2.7	$9\farcs1 \times 7\farcs6$
	(c)	8.5±1.5	8.5± 1.5	$1\farcs1 \times 1\farcs0$
	(d)	11.1±2.2	11.1± 2.2	$0\farcs7 \times 0\farcs5$
N1333 IRAS4A	(a)	351.2±3.1	544.2±13.6	$25\farcs0 \times 24\farcs0$
	(b)	280.4±1.9	525.6± 9.2	$12\farcs0 \times 18\farcs5$
	(c)	172.2±2.1	449.7± 9.8	$5\farcs4 \times 6\farcs2$
A1 Only	(d)	107.0±2.9	324.1±12.0	$2\farcs9 \times 2\farcs2$
A2 Only	(d)	23.0±2.9	81.2± 8.1	$1\farcs8 \times 1\farcs6$
N1333 IRAS4B	(a)	143.3±3.1	180.3± 7.9	$12\farcs0 \times 17\farcs0$
	(b)	129.1±1.9	172.1± 6.0	$8\farcs5 \times 11\farcs0$
	(c)	94.0±2.1	148.9± 5.9	$3\farcs4 \times 3\farcs6$
	(d)	57.6±2.9	128.8± 7.9	$1\farcs7 \times 1\farcs6$

Table 4.2—Continued

Source	Panel	Peak Flux Jy/beam	Integrated Flux Jy	Box Size
N1333 IRAS4C	(a)	47.8±3.1	49.8± 5.5	9″.0 × 11″.0
	(b)	48.5±1.9	50.7± 3.8	5″.5 × 7″.0
	(c)	39.9±2.1	57.0± 4.9	3″.0 × 2″.8
	(d)	26.9±2.9	51.6± 6.9	1″.4 × 1″.5
DG Tauri	(a)	57.7±2.7	66.0± 5.8	11″.4 × 11″.2
	(b)	53.6±2.0	73.8± 6.2	9″.0 × 10″.4
	(c)	46.0±1.9	71.3± 4.8	2″.9 × 2″.9
	(d)	34.6±1.6	68.9± 5.1	2″.1 × 2″.5
DG Tauri B [a]	(a)	45.0±4.8	78.4±11.3	13″.0 × 12″.0
	(b)	38.8±3.5	72.7±10.9	7″.8 × 11″.8
	(c)	30.6±3.4	47.8± 7.2	1″.9 × 3″.1
	(d)	22.7±2.8	49.4± 8.8	1″.4 × 1″.8
L1551 IRS5	(a)	133.9±2.6	173.3± 7.5	17″.0 × 14″.0
	(b)	120.7±2.5	177.2± 7.9	12″.0 × 8″.8
	(c)	77.9±3.3	145.2± 9.1	2″.7 × 3″.5
	(d)	56.0±3.9	107.0±11.1	1″.3 × 1″.9
HL Tauri	(a)	102.7±1.7	108.6± 4.6	19″.0 × 17″.8
	(b)	90.9±1.7	113.6± 4.8	9″.0 × 9″.6
	(c)	70.3±2.4	106.2± 6.0	2″.6 × 2″.9
	(d)	48.8±2.9	106.9± 7.8	1″.8 × 1″.5

Table 4.2—Continued

Source	Panel	Peak Flux Jy/beam	Integrated Flux Jy	Box Size
GG Tauri	(a)	56.7±1.8	73.5± 4.4	12″.6 × 12″.4
	(b)	27.2±1.2	72.5± 3.6	7″.5 × 6″.7
	(c)	10.3±1.2	78.0± 5.0	4″.8 × 4″.9
	(d)	10.8±1.5	95.2± 6.8	4″.4 × 4″.5
GM Aurigae	(a)	20.3±1.1	22.0± 2.6	12″.0 × 14″.0
	(b)	19.2±0.9	22.3± 2.0	7″.8 × 6″.2
	(c)	13.6±1.6	19.6± 3.0	2″.0 × 2″.2
	(d)	13.4±2.5	13.4± 2.5	0″.6 × 0″.5
VLA 1623 A&B	(a)	54.2±3.0	72.1± 6.8	9″.4 × 18″.0
	(b)	44.2±2.2	53.5± 4.3	5″.4 × 8″.0
A Only	(c)	22.8±2.0	34.4± 4.3	1″.6 × 3″.4
B Only	(c)	25.0±2.0	32.5± 4.3	1″.6 × 3″.4
A Only	(d)	22.4±3.5	25.5± 6.3	0″.9 × 1″.7
B Only	(d)	25.8±3.5	25.8± 3.5	0″.4 × 0″.9

Table 4.2—Continued

Source	Panel	Peak Flux Jy/beam	Integrated Flux Jy	Box Size
IRAS 16293-2422	(a)	412.6±5.8	1017.9±26.5	$22\farcs2 \times 27\farcs2$
A Only	(b)	176.4±4.2	441.2±14.1	$12\farcs1 \times 10\farcs0$
B Only	(b)	305.3±4.2	551.4±14.1	$12\farcs5 \times 9\farcs7$
A Only	(c)	60.1±4.1	358.3±18.5	$5\farcs2 \times 5\farcs1$
B Only	(c)	154.1±4.1	498.4±17.2	$6\farcs0 \times 3\farcs8$
A Only	(d)	43.6±4.8	276.2±22.9	$3\farcs1 \times 4\farcs8$
B Only	(d)	112.7±4.8	424.2±24.2	$3\farcs4 \times 4\farcs9$

---

[a] DG Tauri B fluxes were corrected for primary beam attenuation; thus fluxes given have a larger overall uncertainty than the rest of the survey.

“embedded-ness” of the objects. An object with spatially extended structure, such as an envelope with size scales of 1000 AU or larger will have a 5/50 ratio >1, and an object that is entirely compact, such as a circumstellar disk with radius of $\sim$ 100 AU, will not be resolved and the expected ratio will be $\sim$ 1.

The general trend of Figure 17 is, as expected, that most of the optical sources (solid triangles) are compact sources (5/50 ratio of $\sim$ 1) and most of the embedded sources (solid squares) are surrounded by envelopes that are being significantly resolved at 50 kλ (5/50 ratio >1). However, there are a couple of exceptions worth discussing. First, there are two optical stars with unusually large 5/50 ratio— GG Tauri and SVS13 A. GG Tauri is a close binary system with a separation of $0\farcs255$ (Leinert et al. 1991) and a large circumbinary disk (diameter $\sim$ 400 AU; Simon & Guilloteau 1992; Dutrey, Guilloteau, & Simon 1994). Thus in GG Tauri, the 5/50 ratio is resolving the large scale circumbinary disk. SVS13 A, first detected in the infrared at 2.2 μm (Strom, Grasdalen, & Strom 1974; Strom, Vrba, & Strom 1976) is also know to have optical/infrared outbursts (Eislöffel 1991); yet it has a very large 5/50 ratio. There are two possible explanations: (1) the envelope of the nearby, younger embedded object SVS13 A2 is contributing to the flux of SVS13 A1 at 5 kλ, or (2) the optical/infrared emission is a reflection nebula and the source should be classified as embedded. A second set of exceptions are two embedded sources (NGC 1333 IRAS2-B and IRAS4-C) that have unusually small 5/50 ratios. Since these sources are not detected in the optical or the near-infrared they are classified as embedded sources, but their 5/50 ratio and their integrated fluxes in Table 2 indicate that they are compact. These two sources could be optical/near-infrared sources that are viewed through intervening obscuration. The following ten subsections discuss each of the sources in more detail.

4.3.1 DG Tauri and DG Tauri B

DG Tauri is a well studied classical T Tauri star system. Through modeling of the system's SED, Adams, Emerson, & Fuller (1990) estimated a radius of 75 AU for the circumstellar disk. The source was observed in the near-infrared during a lunar occultation (Leinert et al. 1991), and it was determined that the star was a single system with an extended "shell" 6.8 AU in diameter. In addition, near-infrared speckle observations revealed the presence of a "halo" with a diameter of 130 AU (Leinert et al. 1991). In panel (d) of Figure 1, the circumstellar disk around DG Tauri is marginally resolved. Fitting an elliptical Gaussian to the image in panel (d), we obtain a deconvolved Gaussian size of $0\farcs61 \pm 0\farcs1 \times 0\farcs57 \pm 0\farcs1$ with a principal axis of $167^\circ \pm 10^\circ$. This result is different from the measurement at $\lambda = 2.0$ mm from Kitamura, Kawabe, & Saito (1996), which found a deconvolved size of $1\farcs56 \times 0\farcs54$ at a principal axis of 99° and from the measurement at $\lambda = 2.7$ mm from Dutrey et al. (1996), which found a deconvolved size of $1\farcs1 \times 0\farcs6$ at a principal axis of 150°. The extension to the southwest in panel (d) lies along the optical jet (Kepner et al. 1993; Lavalley et al. 1997; Stapelfeldt et al. 1997).

DG Tauri B, located $53''$ southwest of DG Tauri, was observed near the half power point of our beam during the observation of DG Tauri; therefore measured fluxes have a significant additional uncertainty. The fluxes listed in Table 2 were corrected for the primary beam attenuation. DG Tauri B has a molecular outflow (principal axis of $\sim 295^\circ$; Mitchell et al. 1994; Mitchell, Sargent, & Mannings 1997) that is driven by a jet seen at optical (Mundt, Brugel, & Bührke 1987) and centimeter (Rodríguez, Anglada, & Raga 1995) wavelengths. In Figure 2, the emission from DG Tauri B changes morphology with increasing resolution. The extended emission in panel (d) resembles the $\lambda = 3.6$ cm image (Rodríguez, Anglada, & Raga 1995), suggesting that it is tracing ionized gas in jet.

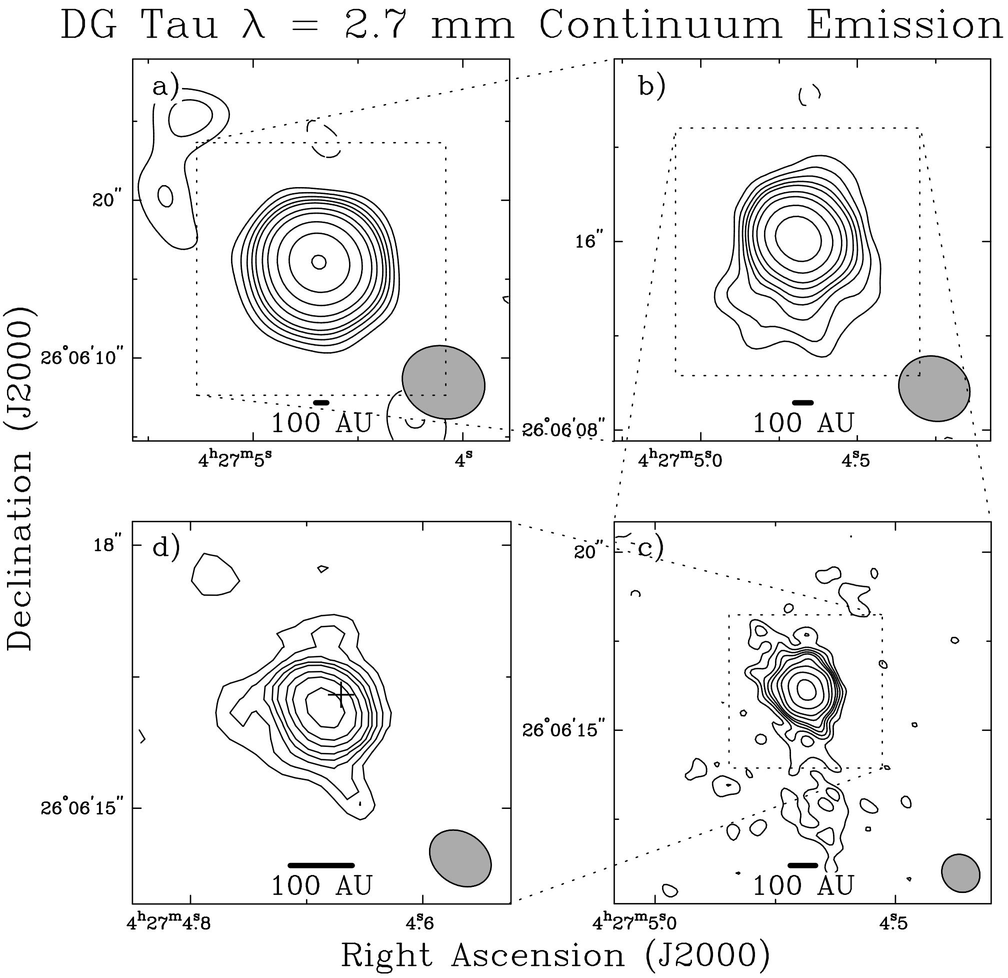

Fig. 4.1. DG Tauri maps of the $\lambda = 2.7$ mm continuum emission. All panels are contoured in steps of (-4 -3 -2 2 3 4 5 6 8 10 14.14 20 28.28) × a rms noise of 2.0 mJy/beam. (a) $\sigma = 2.7$ mJy/beam; beam is $5''.37 \times 4''.57$ P.A. = 72°. (b) $\sigma = 2.0$ mJy/beam; beam is $3''.12 \times 2''.72$ P.A. = 68°. (c) $\sigma = 1.9$ mJy/beam; beam is $1''.12 \times 1''.02$ P.A. = 45°. (d) $\sigma = 1.6$ mJy/beam; beam is $0''.76 \times 0''.58$ P.A. = 56°. The cross in panel (d) is the $\lambda = 6$ cm peak from Bieging, Cohen, & Schwartz (1984).

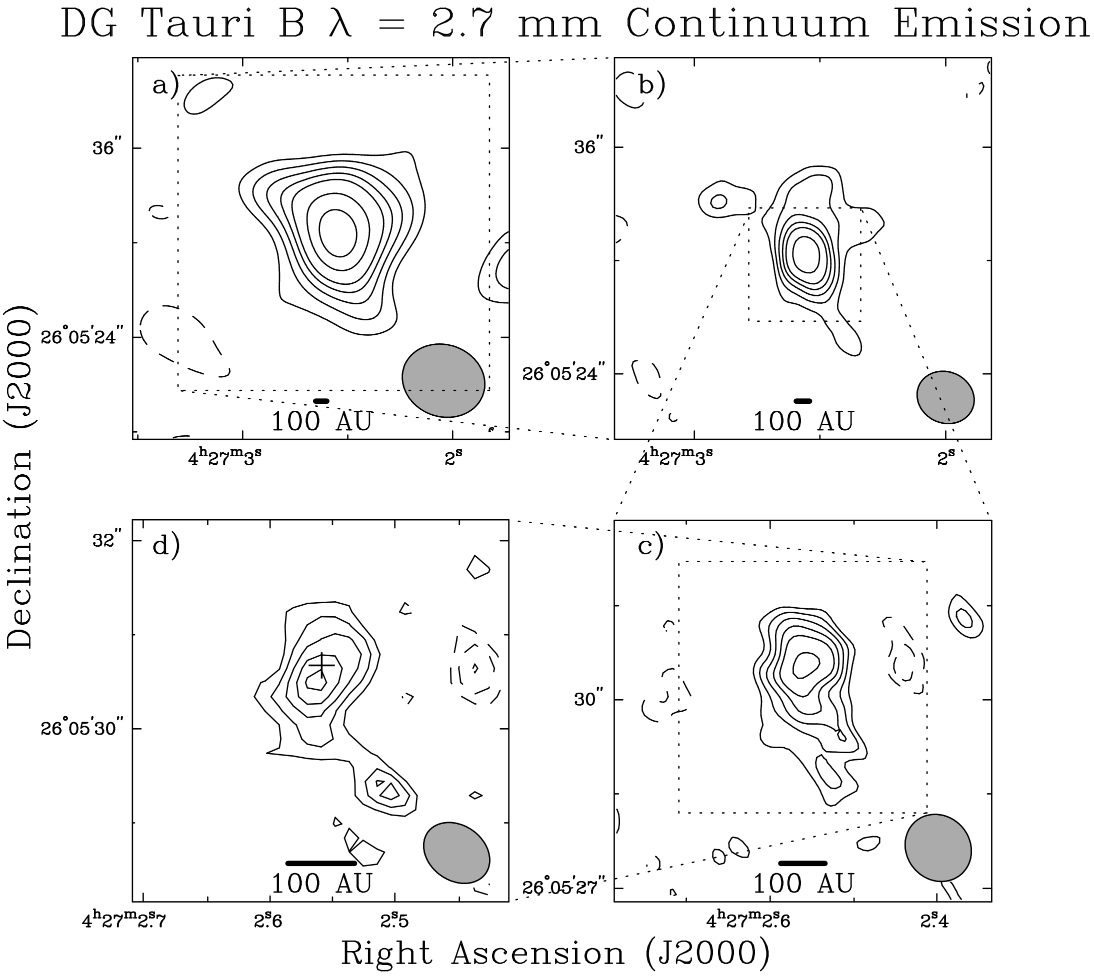

Fig. 4.2. DG Tauri B maps of the $\lambda = 2.7$ mm continuum emission. All panels are contoured in steps of (-4 -3 -2 2 3 4 5 6 8 10 14.14 20 28.28) × a rms noise of 2.0 mJy/beam. (a) $\sigma = 2.7$ mJy/beam; beam is $5\farcs37 \times 4\farcs57$ P.A. = 72°. (b) $\sigma = 2.0$ mJy/beam; beam is $3\farcs12 \times 2\farcs72$ P.A. = 68°. (c) $\sigma = 1.9$ mJy/beam; beam is $1\farcs12 \times 1\farcs02$ P.A. = 45°. (d) $\sigma = 1.6$ mJy/beam; beam is $0\farcs76 \times 0\farcs58$ P.A. = 56°. The cross in panel (d) is the $\lambda = 3.6$ cm peak from Rodríguez, Anglada, & Raga (1995).

Going from panel (d) to panel (c) to panel (b), the major elongation of the emission changes from northwest to north to slightly northeast. In panel (a) the emission is triangular with extension to the northwest, northeast, and southwest. The simplest interpretation is that the high resolution image traces the ionized gas, while the lower resolution images trace both ionized gas and dust. The position angle for the larger scale dust emission is then ~35°, which is consistent with the optical extinction lane (Stapelfeldt et al. 1997) and perpendicular to the outflow jet. The relative flux numbers in Table 2 suggest that roughly half of the flux arises from dust and half from ionized gas in the jet.

4.3.2 L1551 IRS5

L1551 IRS5, one of the prototypical class I sources in the classification scheme of Adams, Lada, & Shu (1987), has the most spectacular bipolar molecular outflow in the Taurus cloud (principal axis of ~ 50°; Snell, Loren, & Plambeck 1980). The $\lambda = 2.7$ mm continuum data presented here were discussed in detail in Looney, Mundy, & Welch (1997), who argued that the source is a proto-binary system with a large-scale envelope, circumbinary disk, and two circumstellar disks. In Figure 3 panels (a) and (b), the emission is dominated by the large-scale envelope, while panel (c) clearly shows the circumbinary envelope. In panel (d), the two point-source-like circumstellar disks are still convolved with the low-level emission from the circumbinary envelope which is extended along a principal axis of ~ 160°. The higher resolution image from Looney, Mundy, & Welch (1997) is not shown.

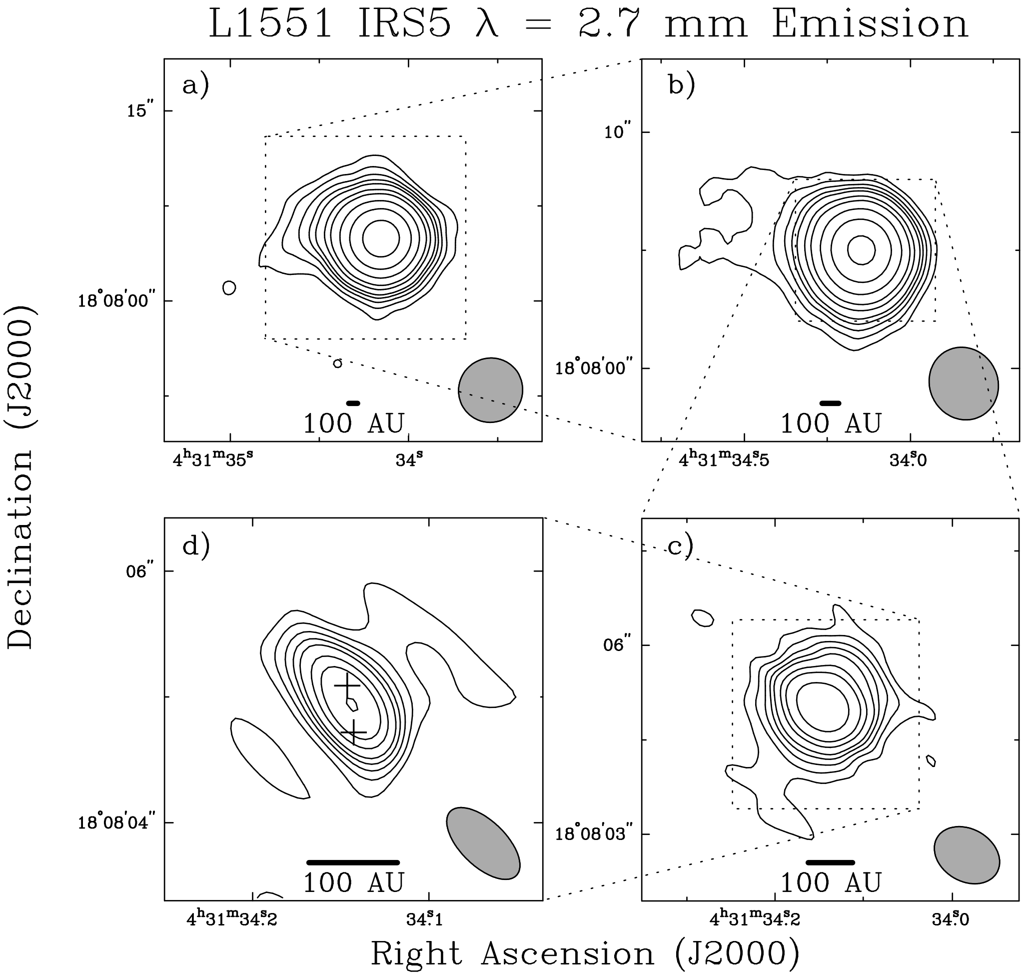

Fig. 4.3. L1551 IRS5 maps of the $\lambda = 2.7$ mm continuum emission. All panels are contoured in steps of (-4 -3 -2 2 3 4 5 6 8 10 14.14 20 28.28) × a rms noise of 3.9 mJy/beam. (a) $\sigma = 2.6$ mJy/beam; beam is $5\farcs15 \times 5\farcs05$ P.A. = -62°. (b) $\sigma = 2.5$ mJy/beam; beam is $3\farcs13 \times 2\farcs92$ P.A. = 31°. (c) $\sigma = 3.3$ mJy/beam; beam is $1\farcs11 \times 0\farcs85$ P.A. = 62°. (d) $\sigma = 3.9$ mJy/beam; beam is $0\farcs74 \times 0\farcs36$ P.A. = 46°. The two crosses in panel (d) are the $\lambda = 1.3$ cm peaks from Koerner & Sargent (1997).

4.3.3 HL Tauri

HL Tauri, perhaps the most studied of the optical/IR visible young stars, has a large-scale CO structure (Sargent & Beckwith 1991; Hayashi, Ohashi, & Miyama 1994) and a compact circumstellar disk ($\sim$ 100 AU) that has been resolved by the CSO-JCMT interferometer (Lay et al. 1994; Lay et al. 1997) and imaged by the BIMA array (Mundy et al. 1996). Figure 4 shows the new BIMA image which has both lower noise and higher resolution than the images of Mundy et al. (1996).

In panel (d), the circumstellar disk of HL Tauri is clearly evident. Fitting an elliptical Gaussian to the image, we obtain a deconvolved Gaussian size of $0''.88\pm0''.1 \times 0''.58\pm0''.1$ and principal axis of $111^\circ\pm10^\circ$, which agrees with the observations of Lay et al. (1994) and Mundy et al. (1996). However, fitting an elliptical Gaussian to the image is not the correct method for determining the true disk size. Recent modeling of the HL Tauri circumstellar disk found that simple models could not fit the CSO-JCMT single baseline interferometer $\lambda =$ 650 μm and 850 μm data and the $\lambda = 2.7$ mm and 7 mm data (Lay et al. 1997). More complicated disk models will be considered in a subsequent paper. The image in panel (d) shows an extension to the north-east along the axis of the optical jet, principal axis 46° (Mundt et al. 1990). This feature likely arises from free-free emission in the jet; such free-free emission dominates the high resolution maps at $\lambda = 7$ mm (Wilner et al. 1997).

HL Tauri is classified as an optical source, but has recently been shown to be embedded within a reflection nebula (Stapelfeldt et al. 1995); we do not see the star directly in optical light, but it can be seen directly in the near-infrared (Weintraub, Kastner, & Whitney 1995; Beckwith & Birk 1995) where optical light is scattered into our line of sight. Our data do not conclusively detect envelope

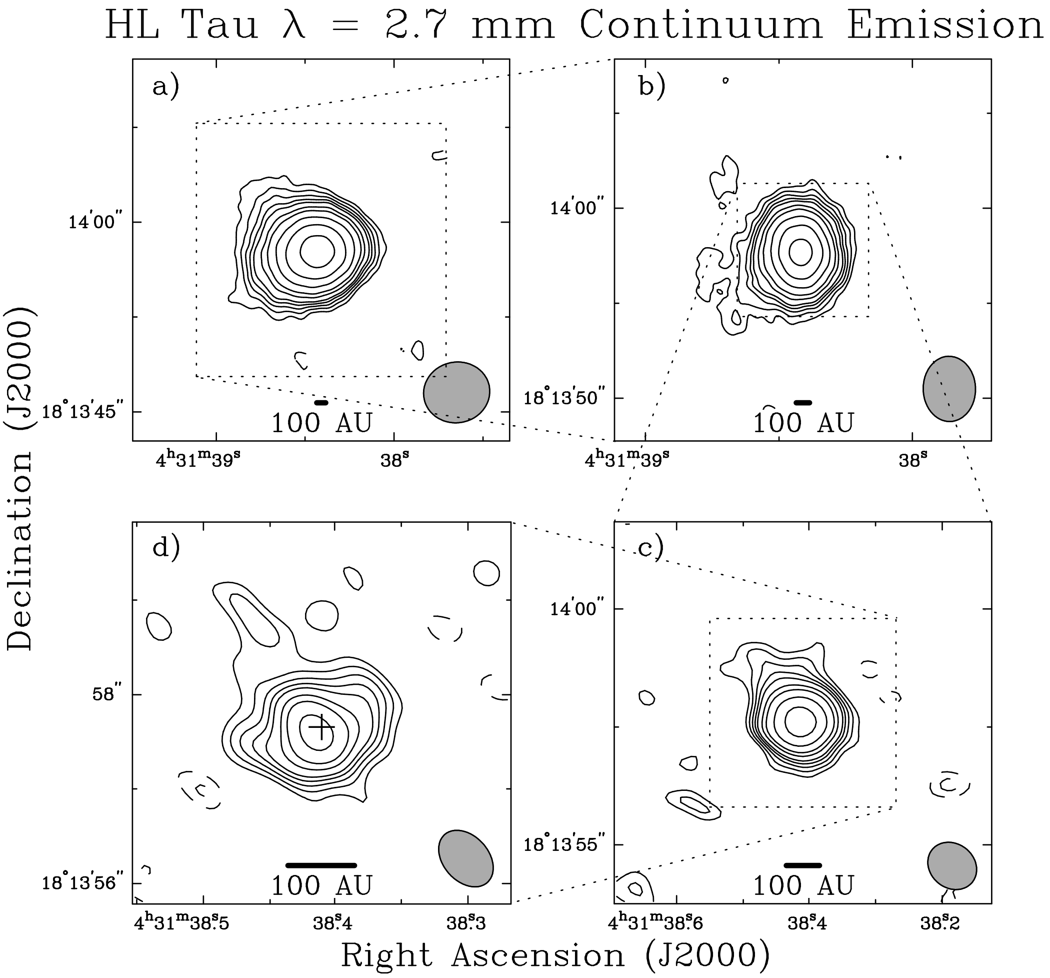

Fig. 4.4. HL Tauri maps of the $\lambda = 2.7$ mm continuum emission. All panels are contoured in steps of (-4 -3 -2 2 3 4 5 6 8 10 14.14 20 28.28) × a rms noise of 2.9 mJy/beam. (a) $\sigma = 1.7$ mJy/beam; beam is $5\overset{''}{.}31 \times 4\overset{''}{.}79$ P.A. = -81°. (b) $\sigma =$ 1.7 mJy/beam; beam is $3\overset{''}{.}43 \times 2\overset{''}{.}79$ P.A. = 1°. (c) $\sigma = 2.4$ mJy/beam; beam is $1\overset{''}{.}11 \times 0\overset{''}{.}94$ P.A. = 53°. (d) $\sigma = 2.9$ mJy/beam; beam is $0\overset{''}{.}68 \times 0\overset{''}{.}48$ P.A. = 43°. The cross in panel (d) is the $\lambda = 3.6$ cm peak from Rodríguez et al. (1994).

emission associated with the extended nebula. The envelope on size scales larger than $3''$ contributes less than 10% of the dust emission, where our precision is limited by the uncertainty of the relative amplitude calibration between arrays .

4.3.4 GG Tauri

GG Tauri is a close binary system with a separation of $0\farcs255$ (Leinert et al. 1991) and a large circumbinary disk (diameter $\sim$ 400 AU; Simon & Guilloteau 1992; Dutrey, Guilloteau, & Simon 1994). Our images presented in Figure 5, have different *u,v* weighting schemes from the rest of the surveyed objects stressing size scales of $5''$, $2''$, $1''$, and $0\farcs9$. Fitting an elliptical Gaussian to the image in panel (b), we obtain a deconvolved size of $3\farcs3 \pm 0\farcs1 \times 2\farcs7 \pm 0\farcs1$ at a position angle of $82° \pm 10°$, which is in good agreement with Dutrey et al. (1994).

There is substructure within the circumbinary disk, as seen in panel (d). These peaks and valleys represent a range of 2σ to 7σ in the emission; hence, they trace real variations in the surface density or temperature. The nature of these "clumps" is investigated in Mundy, Looney, & Welch (1998). No emission is detected at the $0\farcs6$ resolution; we place upper limits on the emission from any compact structures ($< 0\farcs6$), such as individual circumstellar disks within the binary system at a 3σ limit of 5 mJy. The companion binary system of this quadruple system, GG Tauri/c, was not detected at any resolution; the 3σ upper limit on its flux density is 4 mJy.

4.3.5 GM Aurigae

GM Aurigae is another classical T Tauri star system that has a large-scale CO structure (Koerner, Sargent, & Beckwith 1993). In Figure 6 panel (d), we do not see evidence that the disk is resolved, but the signal-to-noise is poor. Fitting an

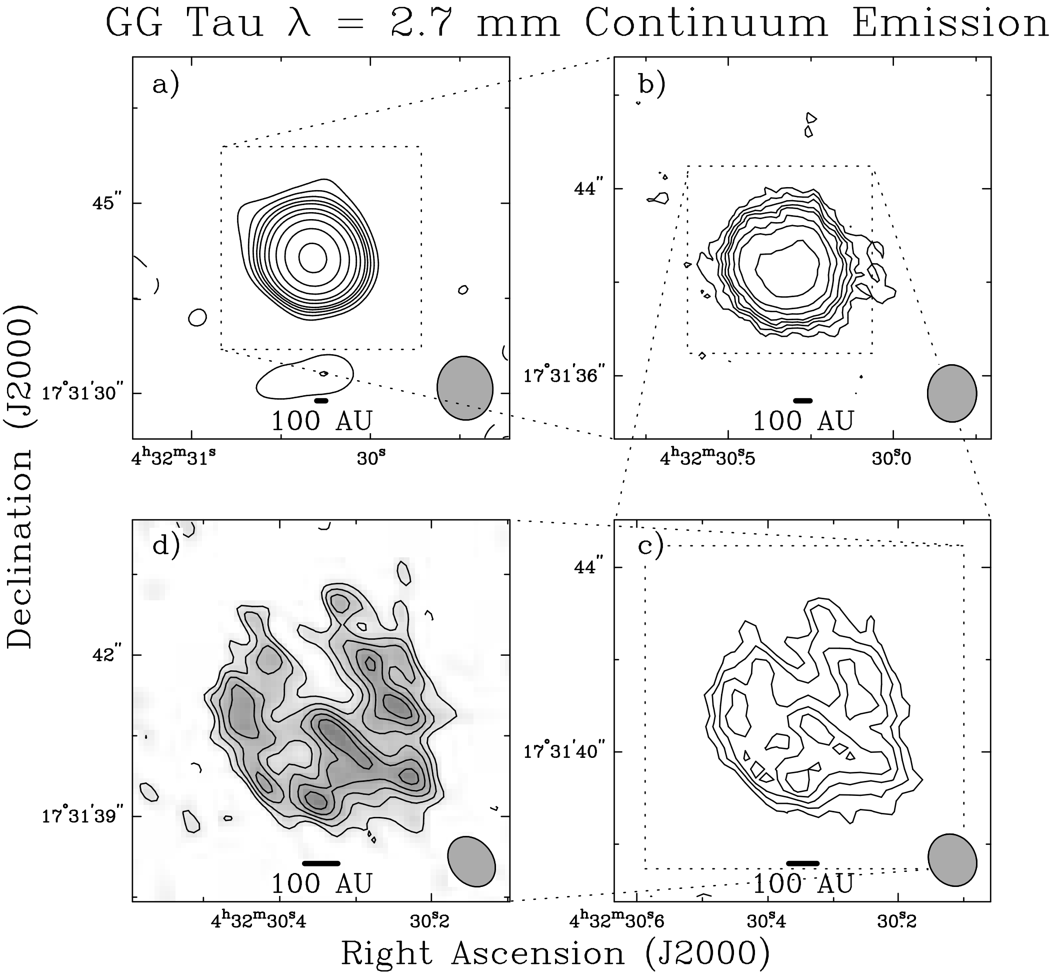

Fig. 4.5. GG Tauri maps of the $\lambda = 2.7$ mm continuum emission. Panel (a) is contoured in steps of (-4 -3 -2 2 3 4 5 6 8 10 14.14 20 28.28) × the rms of panel (a) of 1.8 mJy/beam. Panels (b) thru (d) are (-4 -3 -2 2 3 4 5 6 8 10 14.14) × a rms noise of 1.5 mJy/beam. (a) $\sigma = 1.8$ mJy/beam; beam is $5\farcs02 \times 4\farcs44$ P.A. = 7°. (b) $\sigma = 1.2$ mJy/beam; beam is $2\farcs44 \times 2\farcs12$ P.A. = 1°. (c) $\sigma = 1.2$ mJy/beam; beam is $1\farcs17 \times 1\farcs02$ P.A. = 31°. (d) $\sigma = 1.5$ mJy/beam; beam is $1\farcs02 \times 0\farcs80$ P.A. = 40°. The greyscale is to emphasize the hills and valleys of the "clumps" in the circumbinary disk.

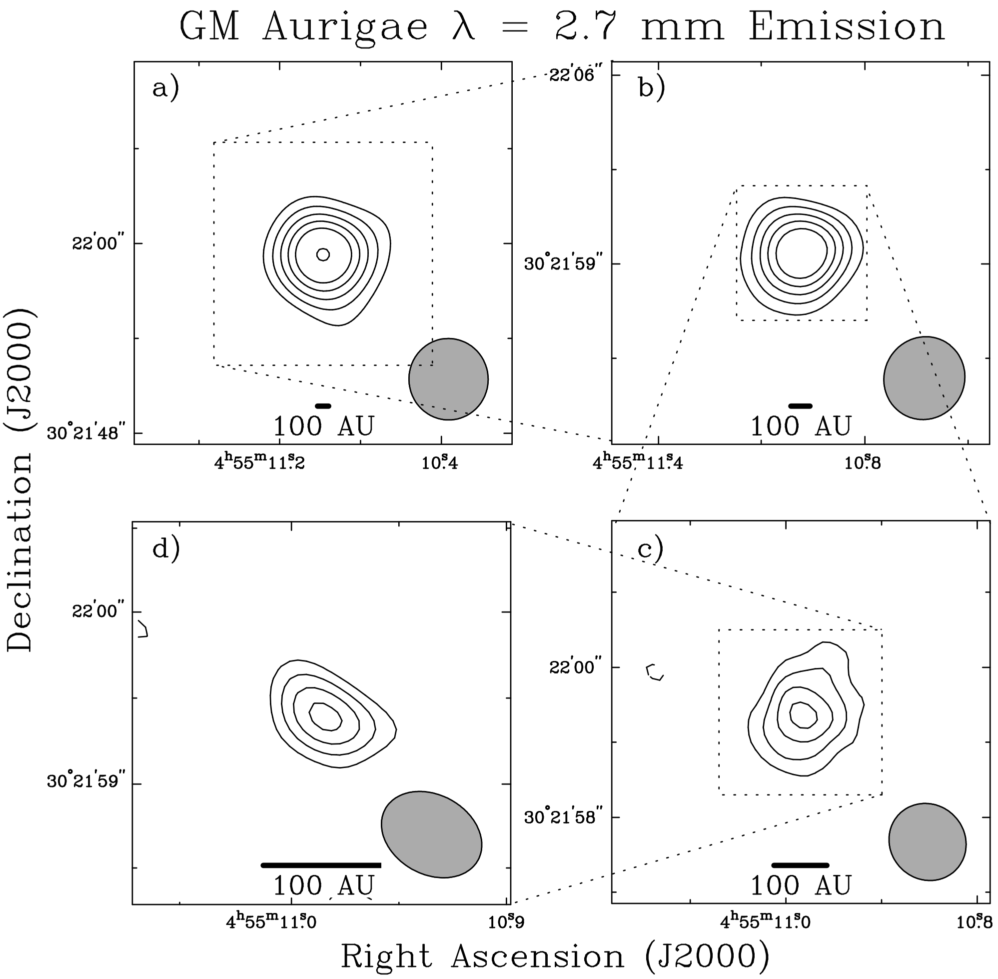

Fig. 4.6. GM Aurigae maps of the $\lambda = 2.7$ mm continuum emission. All panels are contoured in steps of (-4 -3 -2 2 3 4 5 6 8 10 14.14 20 28.28) × a rms noise of 2.5 mJy/beam. (a) $\sigma = 1.1$ mJy/beam; beam is $5\farcs15 \times 5\farcs08$ P.A. = 6°. (b) $\sigma = 0.9$ mJy/beam; beam is $3\farcs12 \times 3\farcs00$ P.A. = -30°. (c) $\sigma = 1.6$ mJy/beam; beam is $1\farcs07 \times 1\farcs00$ P.A. = 51°. (d) $\sigma = 2.5$ mJy/beam; beam is $0\farcs63 \times 0\farcs47$ P.A. = 62°.

elliptical Gaussian to the image in panel (d) yields a point source. We can place a limit on the deconvolved Gaussian size of the circumstellar disk, at the 95% confidence level, as $\leq 0\farcs4$. In panel (c), the emission seems slightly extended along the direction perpendicular to the larger scale CO structure which has a position angle of 55°.

The total flux density reported in Table 2 (22 mJy) is roughly consistent with that measured by Dutrey et al. (1996), 28 mJy. Unlike Dutrey et al., we do not directly resolve the disk. However, we do measure a 35% decrease in flux density between the $5''$ and $0\farcs6$ beams, indicating that some structure is present.

4.3.6 L1448 IRS3

The L1448 complex is located about $\sim$1° southwest from NGC 1333. IRAS revealed three strong infrared sources in the region, of which L1448 IRS3 was the brightest in the far infrared (Bachiller & Cernicharo 1986). IRS3 is projected within the blueshifted lobe of the impressive, highly collimated molecular outflow from L1448-mm which lies to the southeast (Bachiller et al. 1990; Bachiller, Andrè, & Cabrit 1991). Coinciding within the uncertainties of the L1448 IRS3 source is a very strong H_2O maser and $\lambda = 6$ cm compact emission (Anglada et al. 1989). Higher resolution maps in the $\lambda = 2$ cm and 6 cm continuum found that the source was composed of two sources L1448 N(A) and L1448 N(B) (Curiel et al. 1990). Curiel et al. separated the region into two areas: L1448 C, the center of the molecular outflow, and L1448 N corresponding to the IRS3 source. L1448 N(B) contributes most of the flux at millimeter wavelengths (Terebey, Chandler, & André 1993; Terebey & Padgett 1997). A third source is also seen at $\lambda = 2.7$ mm which lies to the north-west of L1448 N(B) (Terebey & Padgett 1997).

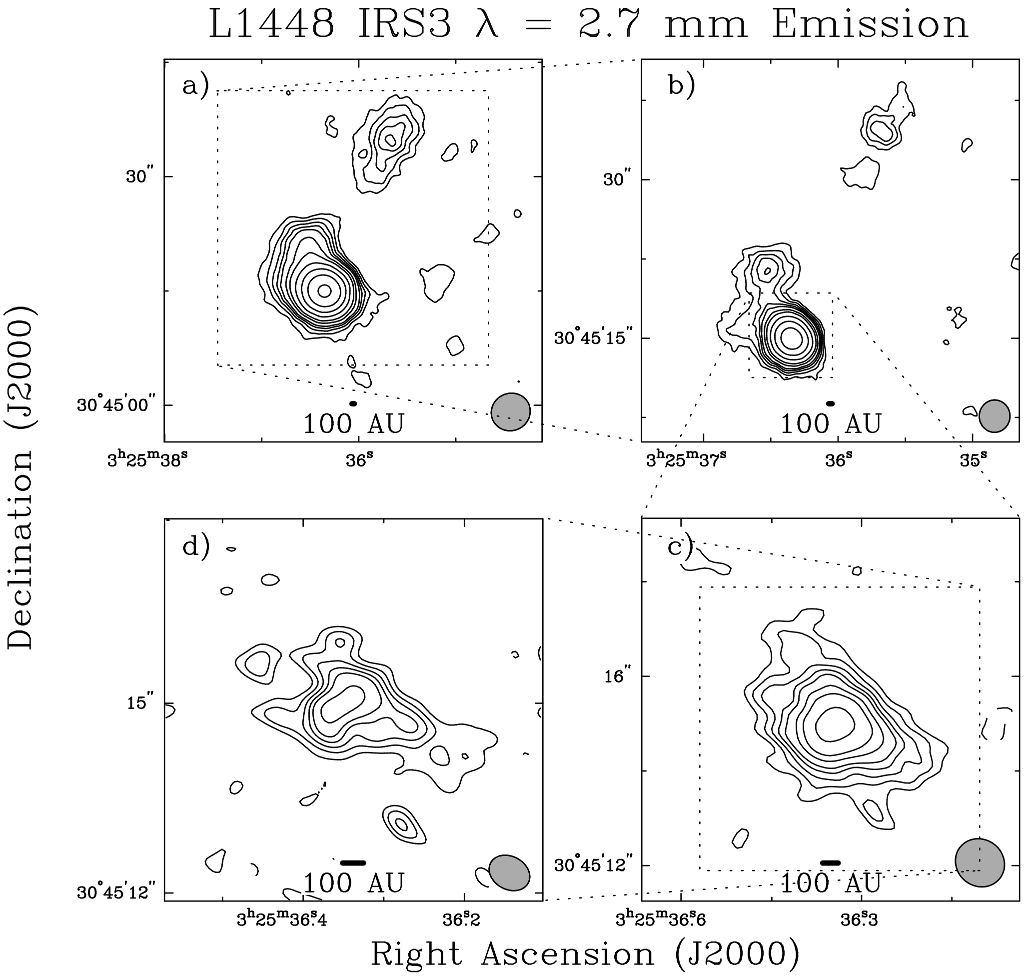

Fig. 4.7. L1448 IRS3 maps of the $\lambda = 2.7$ mm continuum emission. All panels are contoured in steps of (-4 -3 -2 2 3 4 5 6 8 10 14.14 20 28.28 40 56.56) × a rms noise of 2.3 mJy/beam. (a) $\sigma = 1.6$ mJy/beam; beam is $5''.22 \times 4''.89$ P.A. = -71°. (b) $\sigma = 1.5$ mJy/beam; beam is $3''.06 \times 2''.95$ P.A. = -61°. (c) $\sigma = 1.6$ mJy/beam; beam is $1''.08 \times 0''.99$ P.A. = 56°. (d) $\sigma = 2.3$ mJy/beam; beam is $0''.68 \times 0''.52$ P.A. = 63°.

In our images of the region, we clearly detect all three sources which we label: L1448 IRS3 A, B, and C, using the IAU nomenclature. The three sources are indicated in Figure 7 (b). Source A, which is the brightest source at centimeter wavelengths, is significantly weaker than source B at $\lambda = 2.7$ mm. In fact at the highest resolution, source A is not detected. Located to the north-west, source C is detected at all resolutions. Unfortunately, source C is too weak to be plotted on the 5/50 ratio figure. In panels (c) and (d), source B shows very complicated morphology on small scales. There is an outflow associated with the IRS3 region which is nearly parallel to the outflow from L1448-mm, at a position angle of $\sim$ -21° (Bachiller et al. 1995; Davis & Smith 1995). The extension that is seen in panel (c) and (d) is almost perpendicular with the outflow, but it is unclear if it is an envelope or a large disk. The peak flux density decreases by a factor of two in each step of resolution in Figure 7(b), to (c), to (d).

4.3.7 NGC 1333 IRAS2

The NGC 1333 star forming region in Perseus is an extremely active site of star formation with multiple infrared sources (Strom, Vrba, Strom 1976; Aspin, Sandell, & Russell 1994; Lada, Alves, & Lada 1996) and outflows (Sandell et al. 1994; Warin et al. 1996; Bally et al. 1996). NGC 1333 IRAS2 (Jennings et al. 1987) is located on the edge of the large cavity in NGC1333 (Langer, Castets, & Lefloch 1996). The region has a two outflows that originate near IRAS2: the "N-S" outflow with principal axis of $\sim 25°$ (Liseau, Sandell, & Knee 1988) and the "E-W" outflow with principal axis of $\sim 104°$ (Sandell et al. 1994). Recent millimeter interferometric observations show that there are two continuum peaks that are probably associated with the two outflows, and that the northern source (Source A) is responsible for the "E-W" outflow (Blake 1997).

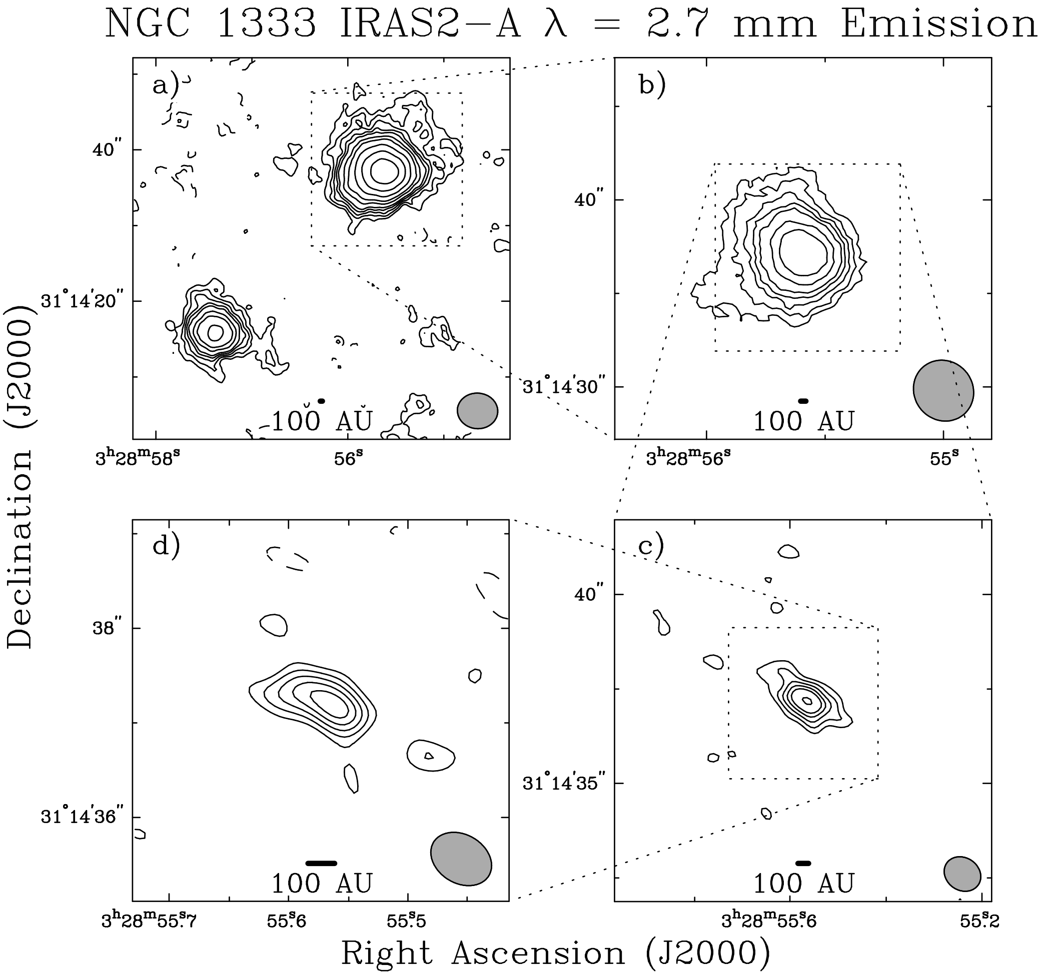

Fig. 4.8. NGC 1333 IRAS2 A maps of the $\lambda = 2.7$ mm continuum emission. Panel (a) is contoured in steps of (-4 -3 -2 2 3 4 5 6 8 10 14.14 20 28.28 40 56.56) × the rms of panel (a) of 1.3 mJy/beam. Panels (b) thru (d) are (-4 -3 -2 2 3 4 5 6 8 10 14.14 20 28.28) × a rms noise of 2.7 mJy/beam. (a) $\sigma = 1.3$ mJy/beam; beam is $5\farcs40 \times 4\farcs70$ P.A. = 86°. (b) $\sigma = 1.2$ mJy/beam; beam is $3\farcs36 \times 3\farcs16$ P.A. = 45°. (c) $\sigma = 1.7$ mJy/beam; beam is $1\farcs02 \times 0\farcs87$ P.A. = 57°. (d) $\sigma = 2.7$ mJy/beam; beam is $0\farcs69 \times 0\farcs52$ P.A. = 60°.

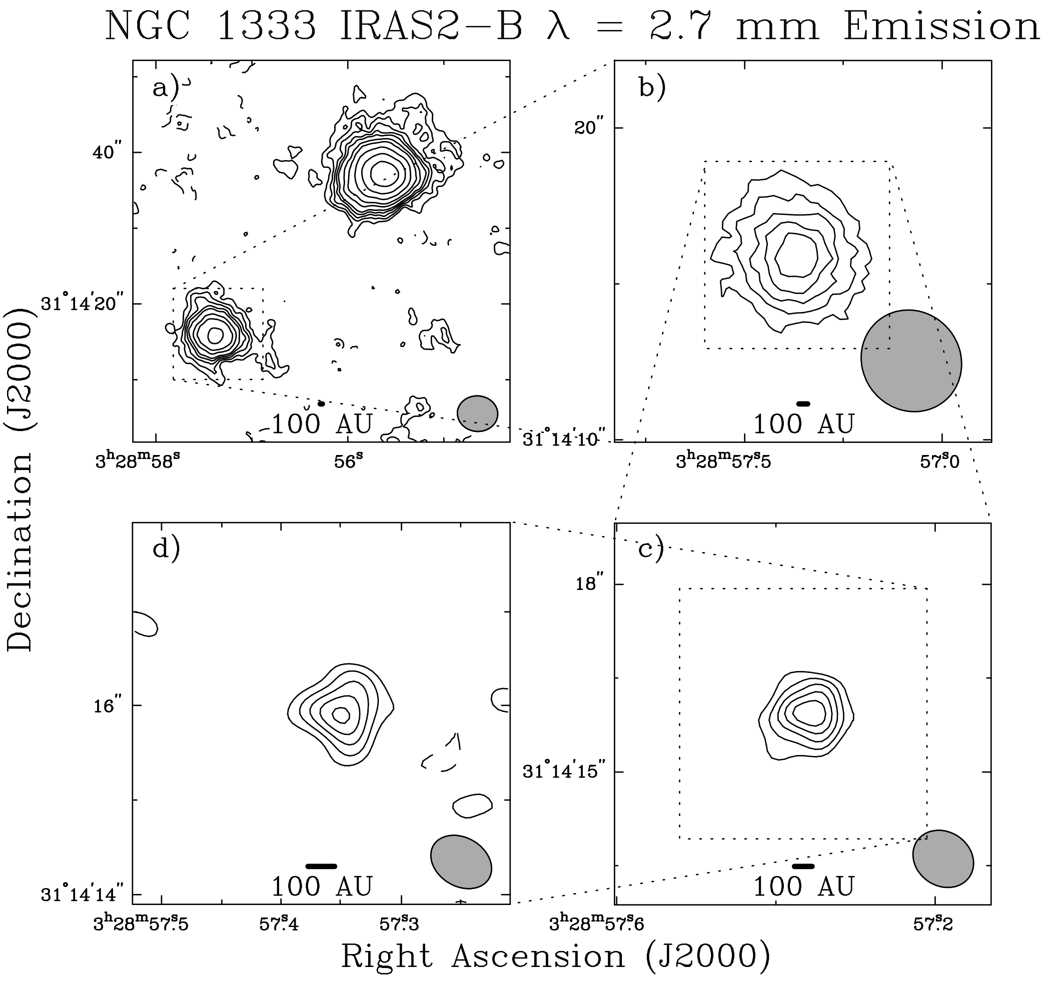

Fig. 4.9. NGC 1333 IRAS2 B maps of the $\lambda = 2.7$ mm continuum emission. Panel (a) is contoured in steps of (-4 -3 -2 2 3 4 5 6 8 10 14.14 20 28.28 40 56.56) × the rms of panel (a) of 1.3 mJy/beam. Panels (b) thru (d) are (-4 -3 -2 2 3 4 5 6 8 10 14.14) × a rms noise of 2.7 mJy/beam. (a) $\sigma = 1.3$ mJy/beam; beam is $5''.40 \times 4''.70$ P.A. = 86°. (b) $\sigma = 1.2$ mJy/beam; beam is $3''.36 \times 3''.16$ P.A. = 45°. (c) $\sigma = 1.7$ mJy/beam; beam is $1''.02 \times 0''.87$ P.A. = 57°. (d) $\sigma = 2.7$ mJy/beam; beam is $0''.69 \times 0''.52$ P.A. = 60°.

Figures 8 and 9 show NGC 1333 IRAS2 A and B respectively. Source A, the stronger of the two sources, is mostly extended emission, and the remaining flux in panel (d) is consistent with a point source. Source B is mostly compact emission. The extension of source B in panel (d) is nearly perpendicular with the "N-S" outflow, suggesting a possible circumstellar structure.

4.3.8 SVS 13

Located northwest of IRAS2, the young stellar object SVS13 (Strom, Vrba, Strom 1976; also referred to as SSV13 in the literature from Herbig & Jones 1983) is associated with the NGC 1333 IRAS3 region (Jennings et al. 1987). IRAS3 is comprised of at least 3 millimeter sources: source A located near the infrared position of SVS13, source B to the southwest (Grossman et al. 1987; Chini et al. 1997) and source C further to the southwest (Chini et al. 1997).

Figures 10 and 11 clearly show all three millimeter sources. In panel (b) of both figures there is another source located to the southwest of source A. This source (which we will call A2) is coincident with VLA source 3 from recent VLA observations of this region (Rodríguez et al. 1997). Located $\sim 6''$ from SVS13, Rodríguez et al. argue that A2 is a better candidate for the HH 7-11 outflow (Rodríguez et al. 1997). However, source A2 is only a 3σ detection in panel (c) and is not detected at higher resolution. We suggest that its lack of compact structure makes it a less likely candidate for driving the outflow, despite the fact that the centimeter emission of source A2 does suggest that is also has a jet. Source A1 is coincident with the infrared/optical source SVS13. Since source A1 is an optical source, we would expect it to be an older object. However, our data suggest that A1 is more deeply embedded. The SVS13 results are discussed in detail in Welch, Looney, & Mundy (1998).

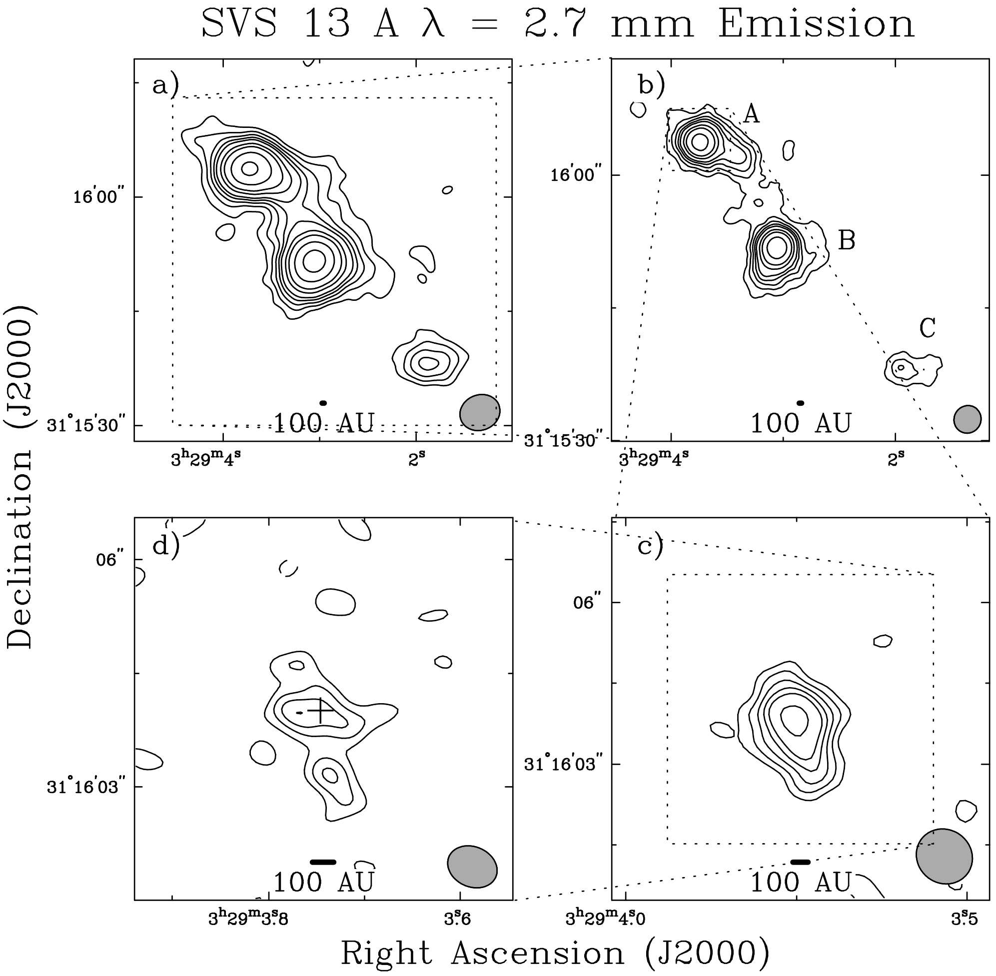

Fig. 4.10. SVS13 A maps of the $\lambda = 2.7$ mm continuum emission. All panels are contoured in steps of (-4 -3 -2 2 3 4 5 6 8 10 14.14 20 28.28 40) × a rms noise of 2.2 mJy/beam. (a) $\sigma = 1.1$ mJy/beam; beam is $5''.40 \times 4''.64$ P.A. = -70°. (b) $\sigma = 1.1$ mJy/beam; beam is $3''.17 \times 3''.05$ P.A. = -43°. (c) $\sigma = 1.5$ mJy/beam; beam is $1''.08 \times 1''.00$ P.A. = 57°. (d) $\sigma = 2.2$ mJy/beam; beam is $0''.68 \times 0''.53$ P.A. = 68°. The cross in panel (d) is the $\lambda = 3.6$ cm peak from Rodríguez, Anglada, & Curiel (1997).

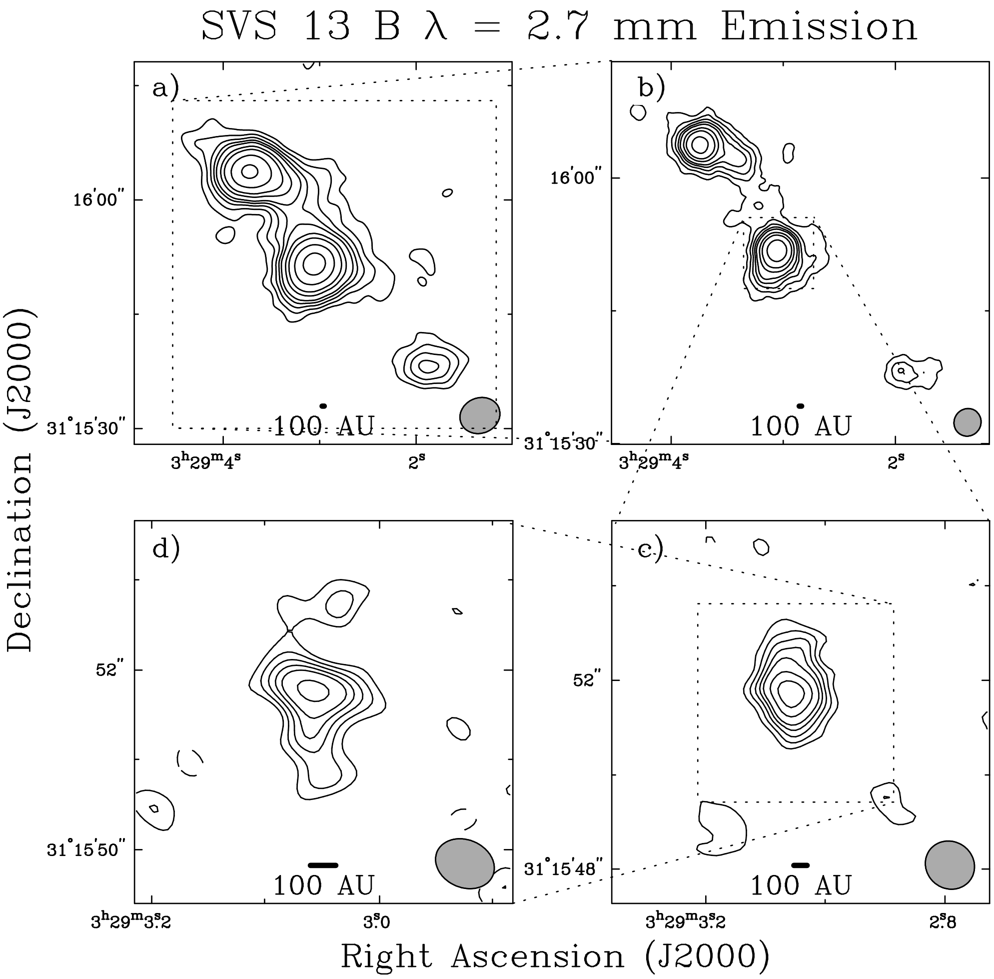

Fig. 4.11. SVS13 B maps of the $\lambda = 2.7$ mm continuum emission. All panels are contoured in steps of (-4 -3 -2 2 3 4 5 6 8 10 14.14 20 28.28 40) × a rms noise of 2.2 mJy/beam. (a) $\sigma = 1.1$ mJy/beam; beam is $5.''40 \times 4.''64$ P.A. = -70°. (b) $\sigma = 1.1$ mJy/beam; beam is $3.''17 \times 3.''05$ P.A. = -43°. (c) $\sigma = 1.5$ mJy/beam; beam is $1.''08 \times 1.''00$ P.A. = 57°. (d) $\sigma = 2.2$ mJy/beam; beam is $0.''68 \times 0.''53$ P.A. = 68°.

4.3.9 NGC 1333 IRAS4

One of the well known sources in the NGC 1333 region is the object NGC 1333 IRAS4, located to the southwest of SVS13. Unresolved in the IRAS images (Jennings et al. 1987), IRAS4 breaks into two bright objects at sub-millimeter wavelengths (Sandell et al. 1991). Our images, Figures 12, 13, and 14, show three objects: IRAS4 A, B, and C. Our data provide the first indication that source C may be a young star. Source C is detected at all resolutions; its 5/50 ratio is near 1; and in Table 2 the integrated flux is constant at all resolutions. The characteristics of source C are more like those of an optical/IR source than its IRAS4 companions.

NGC1333 IRAS4 A & B have been observed with the CSO-JCMT single baseline interferometer at $\lambda = 840\ \mu$m (Lay, Carlstrom, & Hills 1995). Their best fit for source A was two elliptical Gaussians, and indeed in our images source A is shown to be a binary system. It is interesting to note that the best fit fluxes from Lay et al. give a ratio of 0.78, while our two sources have a flux ratio of 0.25. This suggests that either the emissivity of these two objects vary differently with frequency or the optical depth is very different. For source B, the CSO-JCMT data could not be fit with a single star or binary model. Lay et al. suggest that source B may be a triple system; however, they were not aware of source C at that time, which may have confused their analysis. Our image of source B shows weak extensions to the north and southwest, but our data are not sufficient to determine the nature of these features. They could trace a multiple stellar system or inhomogeneities within the envelope.

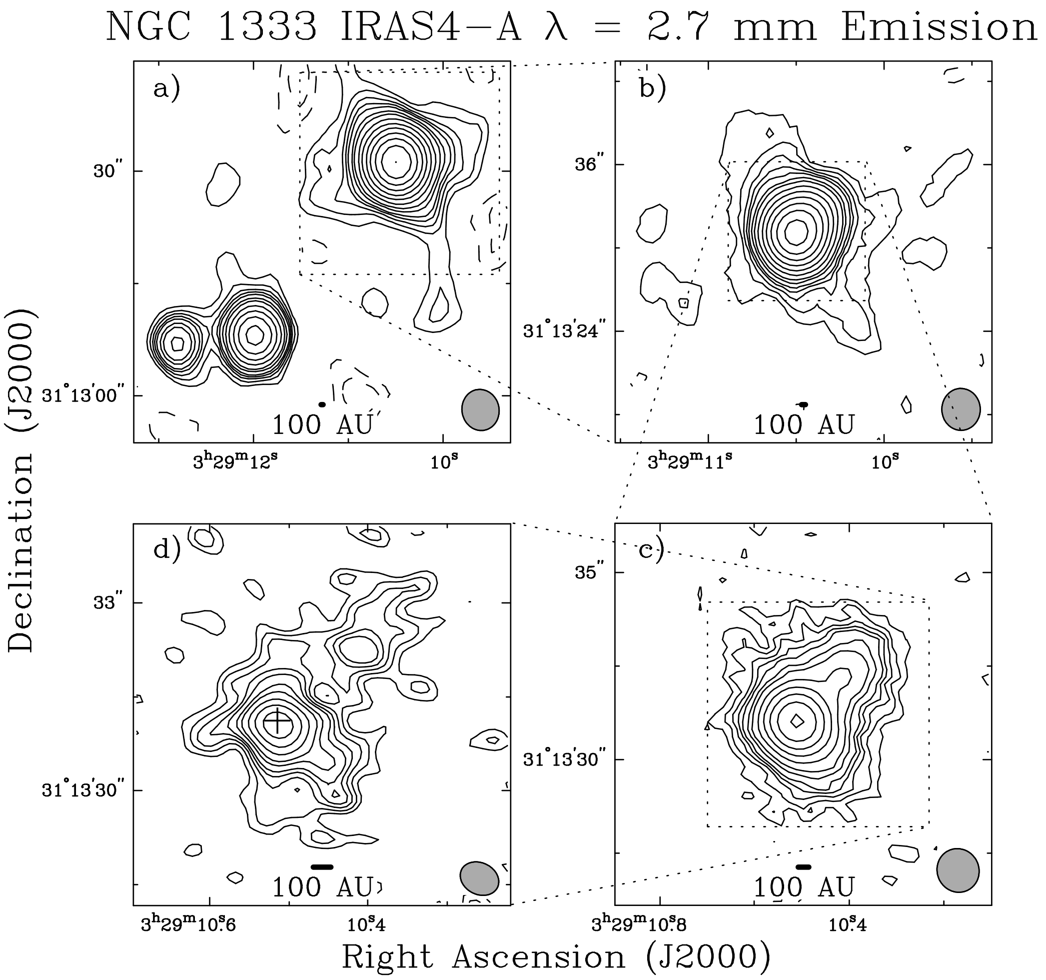

Fig. 4.12. NGC 1333 IRAS4 A maps of the $\lambda = 2.7$ mm continuum emission. Panel (a) is contoured in steps of (-4 -3 -2 2 3 4 5 6 8 10 14.14 20 28.28 40) × the rms of panel (a) of 3.1 mJy/beam. Panels (b) thru (d) are (-4 -3 -2 2 3 4 5 6 8 10 14.14 20 28.28 40 56.56) × a rms noise of 2.9 mJy/beam. (a) $\sigma = 3.1$ mJy/beam; beam is $5\farcs52 \times 5\farcs02$ P.A. = 12°. (b) $\sigma = 1.9$ mJy/beam; beam is $3\farcs02 \times 2\farcs81$ P.A. = 1°. (c) $\sigma = 2.1$ mJy/beam; beam is $1\farcs18 \times 1\farcs13$ P.A. = 30°. (d) $\sigma = 2.9$ mJy/beam; beam is $0\farcs65 \times 0\farcs51$ P.A. = 65°. The cross in panel (d) is the $\lambda =$ 1.3 cm peak from Mundy et al. (1993).

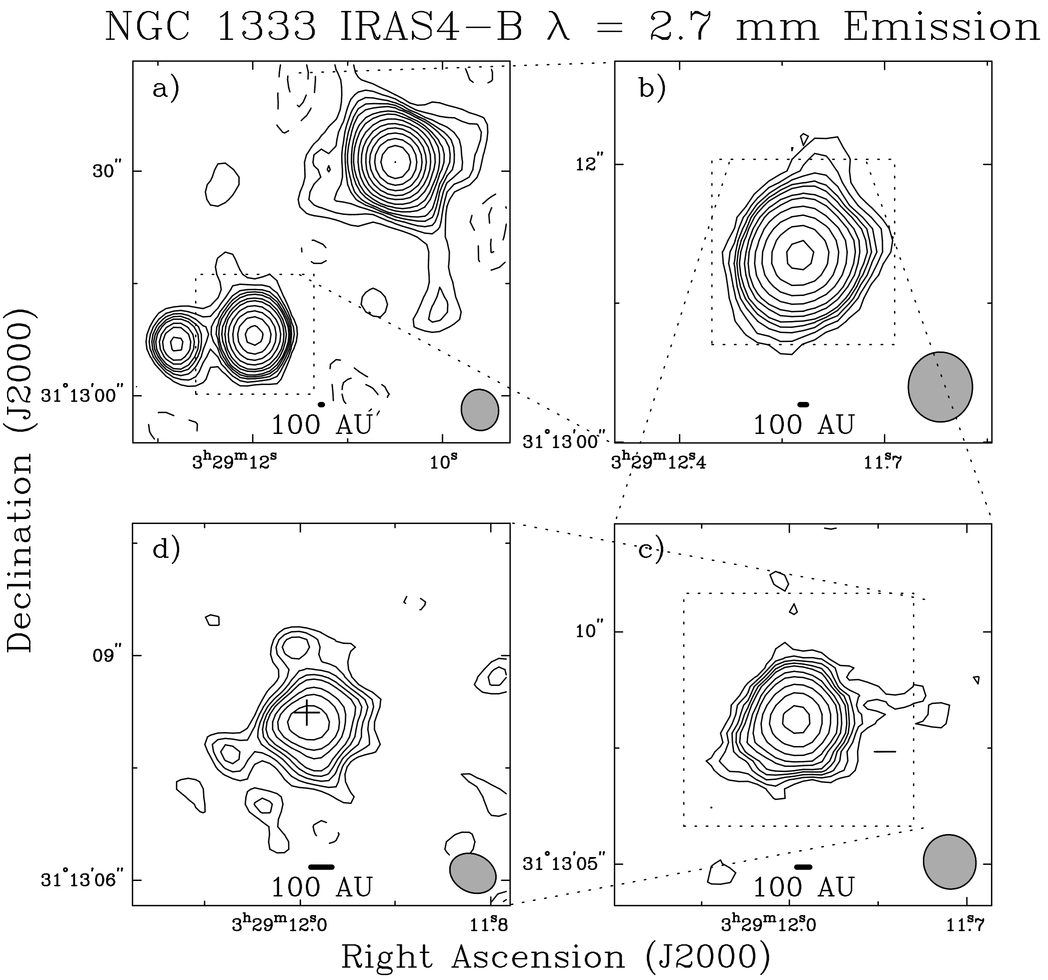

Fig. 4.13. NGC 1333 IRAS4 B maps of the $\lambda = 2.7$ mm continuum emission. Panel (a) is contoured in steps of (-4 -3 -2 2 3 4 5 6 8 10 14.14 20 28.28 40) × the rms of panel (a) of 3.1 mJy/beam. Panels (b) thru (d) are (-4 -3 -2 2 3 4 5 6 8 10 14.14 20 28.28 40 56.56) × a rms noise of 2.9 mJy/beam. (a) $\sigma = 3.1$ mJy/beam; beam is $5''\!.52 \times 5''\!.02$ P.A. = 12°. (b) $\sigma = 1.9$ mJy/beam; beam is $3''\!.02 \times 2''\!.81$ P.A. = 1°. (c) $\sigma = 2.1$ mJy/beam; beam is $1''\!.18 \times 1''\!.13$ P.A. = 30°. (d) $\sigma = 2.9$ mJy/beam; beam is $0''\!.65 \times 0''\!.51$ P.A. = 65°. The cross in panel (d) is the $\lambda =$ 1.3 cm peak from Mundy et al. (1993).

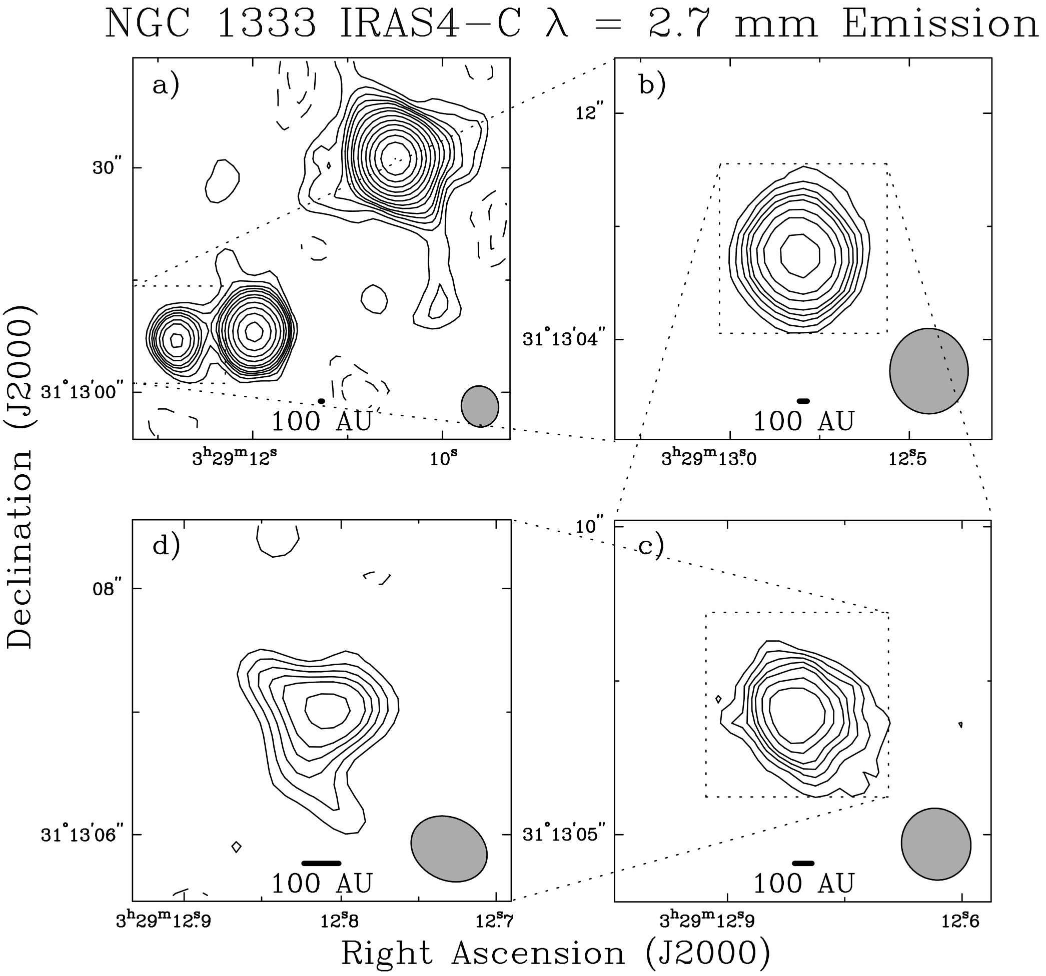

Fig. 4.14. NGC 1333 IRAS4 C maps of the $\lambda = 2.7$ mm continuum emission. Panel (a) is contoured in steps of (-4 -3 -2 2 3 4 5 6 8 10 14.14 20 28.28 40) × the rms of panel (a) of 3.1 mJy/beam. Panels (b) thru (d) are (-4 -3 -2 2 3 4 5 6 8 10 14.14 20 28.28 40 56.56) × a rms noise of 2.9 mJy/beam. (a) $\sigma = 3.1$ mJy/beam; beam is $5''.52 \times 5''.02$ P.A. = 12°. (b) $\sigma = 1.9$ mJy/beam; beam is $3''.02 \times 2''.81$ P.A. = 1°. (c) $\sigma = 2.1$ mJy/beam; beam is $1''.18 \times 1''.13$ P.A. = 30°. (d) $\sigma = 2.9$ mJy/beam; beam is $0''.65 \times 0''.51$ P.A. = 65°.

4.3.10 VLA 1623

The source VLA 1623, near the center of the ρ Ophiuchi cloud core A, is the prototypical Class 0 source (Andrè, Ward-Thompson, & Barsony 1993) that drives a large outflow with principal axis $\sim$60° (Andrè et al. 1990; Dent et al. 1995; Yu & Chernin 1997). This source has been observed with the CSO-JCMT single baseline interferometer at $\lambda = 1360$ and 845 μm (Pudritz et al. 1996). They modeled the source as a Gaussian and placed a 70 AU radius upper limit on the size of the compact circumstellar disk. Recent, high resolution VLA observations at $\lambda = 3.6$ cm (Bontemps & Andrè 1997) show a series of emission clumps that are interpreted as knots of a radio jet driving the large CO outflow. However the position angle of the radio jet and the CO outflow differ by $\sim 30°$. In our highest resolution images, Figure 15 panels (c) and (d), the millimeter emission breaks into nearly equal point sources. The two crosses mark the positions of the two point sources from Bontemps & Andrè (1997) that appear associated with the millimeter emission from VLA 1623; the positions agree to within the uncertainties. The total emission from the two sources at $\lambda = 3.6$ cm is less than 1 mJy. If the emission at $\lambda = 3.6$ cm is dominantly from free-free emission we would not expect very much contribution of this emission at $\lambda = 2.7$ mm. Thus, the emission at $\lambda = 2.7$ mm is dominated by dust emission. We have reanalyzed the data of Pudritz et al. (1996) and find that a binary interpretation is consistent with their data. VLA 1623 is most likely a very young binary system with two circumstellar disks. Like IRAS 16293-2422, we refer to the southern source as A and the northern source as B.

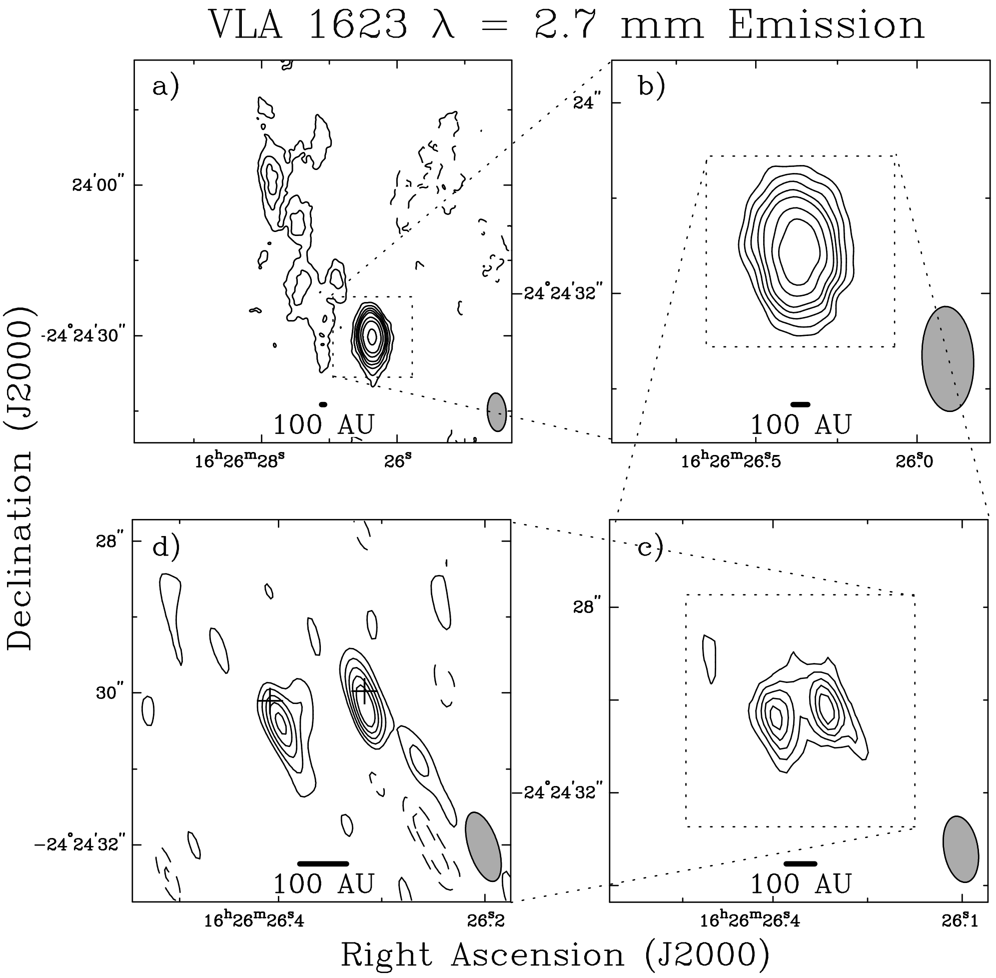

Fig. 4.15. VLA 1623 maps of the $\lambda = 2.7$ mm continuum emission. All panels are contoured in steps of (-4 -3 -2 2 3 4 5 6 8 10 14.14) × a rms noise of 3.5 mJy/beam. (a) $\sigma = 3.0$ mJy/beam; beam is $7''\!.65 \times 3''\!.80$ P.A. = 4°. (b) $\sigma = 2.2$ mJy/beam; beam is $4''\!.40 \times 2''\!.19$ P.A. = 3°. (c) $\sigma = 2.0$ mJy/beam; beam is $1''\!.44 \times 0''\!.74$ P.A. = 10°. (d) $\sigma = 3.5$ mJy/beam; beam is $0''\!.95 \times 0''\!.39$ P.A. = 18°. The crosses indicate the $\lambda = 3.6$ cm positions from Bontemps & Andrè (1997).

4.3.11 IRAS 16293-2422

IRAS 16293-2422 is a very well studied deeply embedded binary system with two molecular outflows (Walker et al. 1986; Wootten 1989; Mundy et al. 1992) in ρ Ophiuchi. The outflow from the southern source A has a principal axis of $\sim 50°$, and the outflow of the northern source B has a principal axis of $\sim 75°$. The outflow of source B does not extend down near the source, which may indicate that source B is no longer driving its outflow. In high resolution observations at $\lambda = 2$ cm, the system is comprised of three peaks: A1 and A2 to the southeast and B to the northwest (Wootten 1989). In Figure 16, we detect the two sources, A and B, that were detected previously at $\lambda = 2.7$ mm (Mundy et al. 1986; Mundy et al. 1992). In panel (c), there is still a clear connection between the two sources that is most likely a circumbinary envelope. In panel (d), the massive circumbinary envelope is mostly resolved out and the residual emission arises from two compact sources and some weak extensions that are probably attributed to density enhancements within the circumbinary structure. At high resolution, source A appears elongated along the position angle of the $\lambda = 2$ cm sources, which are indicated in panel (d) as crosses. IRAS 16293-2422 source A has the highest 5/50 ratio in the survey. In fact, the ratio is twice as large as the next highest 5/50 ratio source L1448 IRS3 B. Thus, source A is very extended; most of its mass is located in the envelope, perhaps making this the youngest source in this survey.

Our measurement of the integrated flux in this source is higher than previous observations. This is because we have shorter spacing *u,v* data which pick up the extended structure of the circumbinary envelope better than previous works. If we remove the shorter *u,v* spacings, the total integrated flux is ~750 mJy, which is more in agreement with other measurements.

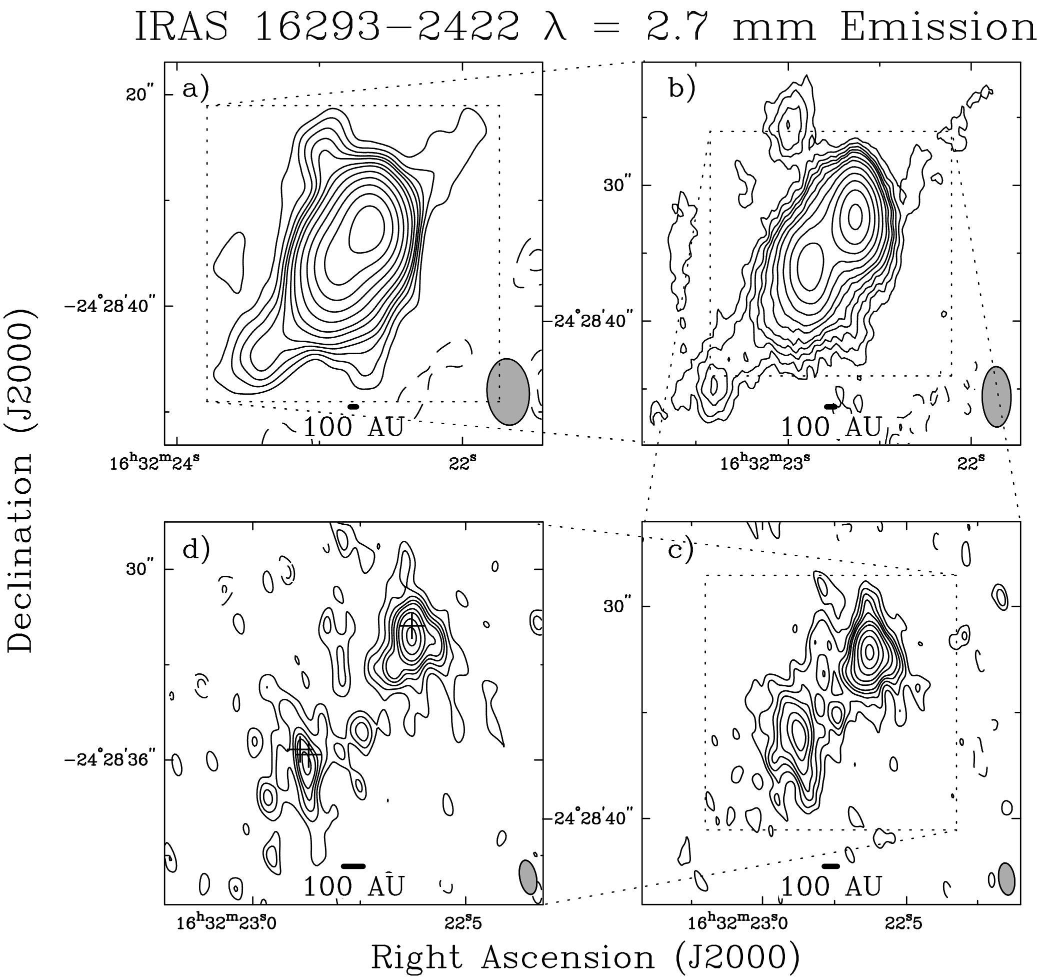

Fig. 4.16. IRAS 16293-2422 maps of the $\lambda = 2.7$ mm continuum emission. Panel (a) is contoured in steps of (-4 -3 -2 2 3 4 5 6 8 10 14.14 20 28.28 40 56.56) × the rms of panel (a) of 5.8 mJy/beam. Panels (b) thru (d) are (-4 -3 -2 2 3 4 5 6 8 10 14.14 20 28.28 40 56.56) × a rms noise of 4.8 mJy/beam. (a) $\sigma = 5.8$ mJy/beam; beam is 6.″29 × 4.″06 P.A. = 4°. (b) $\sigma = 4.2$ mJy/beam; beam is 4.″45 × 2.″16 P.A. = 1°. (c) $\sigma = 4.1$ mJy/beam; beam is 1.″52 × 0.″76 P.A. = 7°. (d) $\sigma = 4.8$ mJy/beam; beam is 1.″09 × 0.″53 P.A. = 11°. The crosses indicate the $\lambda =$ 2 cm positions from Wootten (1989).

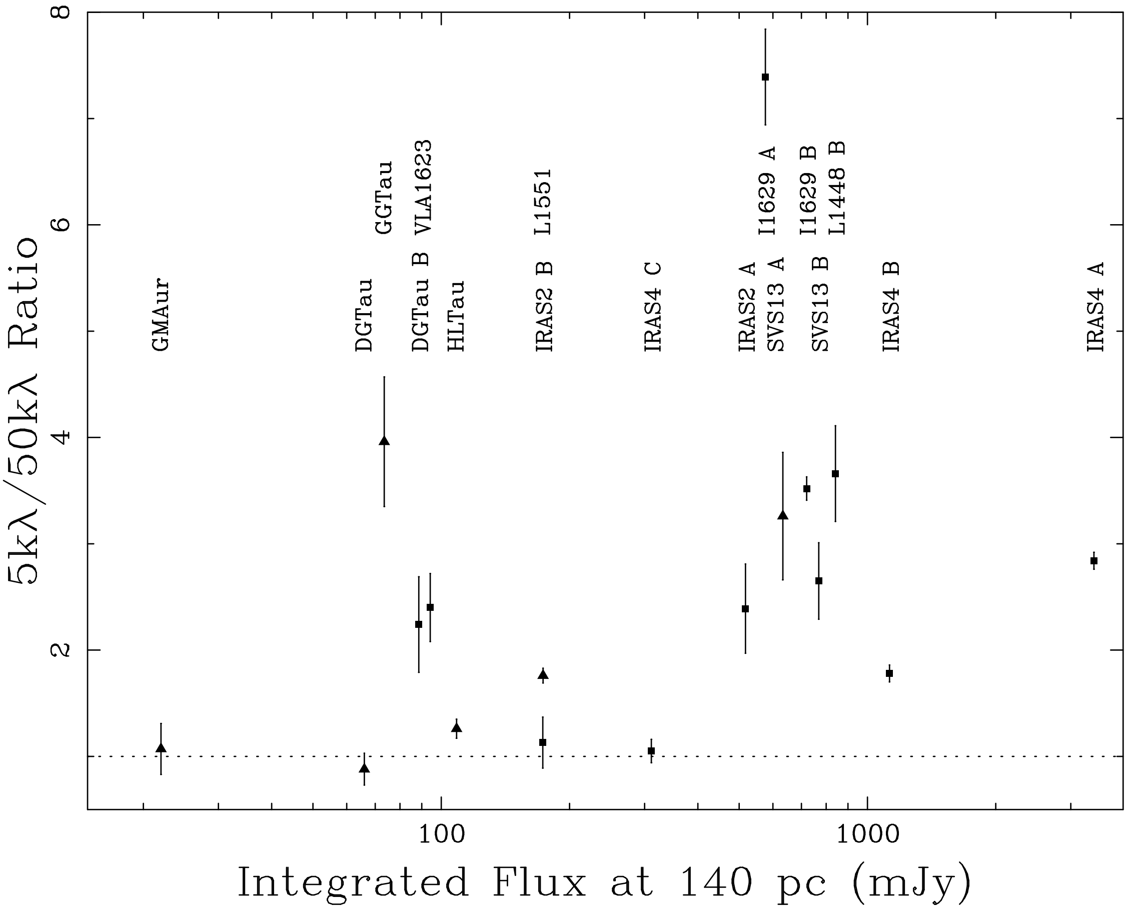

Fig. 4.17. Comparison of the ratio of the flux at 5kλ and 50kλ fringe spacings amplitude and the integrated flux of each object from Table 2, both adjusted to the distance of Taurus. The solid triangle symbols indicate optical/IR sources and the solid square symbols indicate the embedded sources. Each point is labeled with its corresponding source.

4.4 Comparison of Structure

There is a striking difference between the embedded objects and the optical/IR objects in our survey. The optical sources have compact central emission on spatial scales of $\sim 1''$ with little large-scale envelope emission. This is illustrated both in Figure 17 and by the peak/integrated fluxes in Table 2. The peak flux does not change significantly, even down to size scales of $\sim 1\farcs5$, until the resolution is sufficient to see the circumstellar disk. This contrasts strongly with the embedded objects which typically have $\geq 50\%$ of their emission in large scale structures. The embedded sources, Figures 7 thru 16, show dramatic variation in structure as the resolution is varied through the panels. Structures are resolved out as the shorter *u,v* spacings are down-weighted in the higher resolution panels. In the highest resolution panels, the embedded objects typically have a residual compact component, but the flux of this component is significantly less than the large scale extended emission. In addition, the images of the embedded objects show more complex sub-structures within the field.

How does the circumstellar structure evolve from the envelope dominated phase to the disk dominated phase? Should we expect to see circumstellar disks in the youngest sources or does the circumstellar envelope extend down to 10's of AU? Circumstellar disks are known to be common around young optical stars with typical disk masses of ~ 0.02 $M_\odot$ and masses as high as 0.1 $M_\odot$ (Osterloh & Beckwith 1995), but how common are circumstellar disks in the youngest sources? In the embedded systems, the circumstellar envelope dominates the emission and the mass. Indeed, with these observations it is difficult to isolate the circumstellar disk from the envelope even at $0\farcs5$ resolution. In general, at the smallest scales, residual emission could be from disks or extensions of the envelope. The emission does not show a discontinuity in flux between $1''$ and $3''$ scales; this indicates that any disk present cannot be significantly more massive than the mass of the envelope extended to small scales. In short, younger circumstellar disks are less prominent mass reservoirs than disks in the optical systems. One qualification on this point is that the embedded sources are typically a factor of two farther away than the optical sources. Thus, we cannot say that circumstellar disks in embedded systems are systematically less massive than typical disks around young optical stars. Higher resolution observations, a factor of two or more better, are needed to make a detailed comparison of disk properties.

Theoretical works support this picture in which the disk grows in prominence as the system evolves. Cassen & Moosman (1981) show that the detailed evolution of the disk is very dependent upon the distribution of mass and angular momentum in the original cloud and dissipative processes within the disk. For reasonable assumptions, they found that a circumstellar disk would grow more massive and larger with time. Building upon these results, Stahler et al. (1994) considered a disk with negligible viscosity that was formed as soon as the angular momentum in the infalling material causes it to "miss" the protostar. They found that the radius of the disk is a strong function of time, increasing as t^3. At the same time as the accretion rate onto the star begins to fall off, the mass of the disk increases. These papers suggest that embedded sources will typically have smaller, less massive disks than optical T Tauri systems.

4.5 Simple Mass Comparison

How does the circumstellar mass in the optical systems and embedded systems compare? The $\lambda = 2.7$ mm emission provides a valuable measure of circumstellar mass. Using a very simple emissivity model, we can make a rough comparison of masses in the different systems. The expected thermal emission from dust for a single-temperature, optically thin source is given by $F_\nu = B_\nu(T_{dust})\kappa_\nu M/D^2$, where $B_\nu(T)$ is the Planck function , T_{dust} is the temperature of the dust, κ_ν is the dust mass opacity, M is the mass of gas and dust, and D is the distance to the source. The dust mass opacity is poorly known and may have uncertainties of factors of 2-3 (Beckwith & Sargent 1991; Draine 1990; Pollack et al. 1994; Stognienko, Henning, & Ossenkopf 1995). We adopt a κ_ν that is consistent with other works (e.g. Beckwith & Sargent 1991; Ohashi et al. 1991; Osterloh & Beckwith 1995): $\kappa_\nu = 0.1(\nu/1200 \text{ GHz})$ cm^2 g^{-1}, corresponding to $\kappa_\nu = 0.009$ cm^2 g^{-1} at $\lambda = 2.7$ mm. We assume a constant temperature of 50K for all sources; this temperature is a median value between the hotter inner regions of circumstellar disks and the cooler outer regions of circumstellar envelopes. This single temperature approach likely overestimates the temperature in envelope dominated sources, making the deeply embedded objects under-massed and underestimates the temperature in disk dominated sources, making the optical objects over-massed. Although we do not expect this simple model to give accurate masses, it provides rough estimates that are adequate for qualitative comparisons and within a factor of 2 of the likely mass. More detailed modeling of the individual sources will be done in subsequent papers.

Table 3 lists the estimated mass for each source, as well as the best fitted position from the highest resolution image (typical uncertainties of $0\farcs15$). The simple estimate yields nearly a factor of a hundred range between the most and least massive region in our sample. Where there is overlap, there is good agreement between the simple model and published mass estimates. For example, the mass for HL Tauri in Table 3, 0.06 M$_\odot$, is within the range of masses previously found, 0.05 to 0.1 M$_\odot$ (Beckwith et al. 1990; Mundy et al. 1996, Wilner, Ho, & Rodríguez 1996; Close et al. 1997), and the mass of DG Tauri in Table 3, 0.04 M$_\odot$, is consistent with previous estimates of 0.02 to 0.04 M$_\odot$

(Beckwith et al. 1990; Dutrey et al. 1996). For the embedded systems IRAS 16293-2422 and L1448 IRS3 B, our estimated masses of 0.75 $M_\odot$ and 0.42 $M_\odot$ respectively, are similar to other estimates, 1 $M_\odot$ for IRAS 16293-2422 (e.g. Mundy et al. 1992) and 0.5 $M_\odot$ for L1448 IRS3 B (e.g. Terebey, Chandler, & André 1993).

The estimated circumstellar masses for the two categories, optical/infrared and deeply embedded sources, follow the expected broad trend: the embedded objects typically have a factor of 5 or so larger masses. From the circumstellar masses for the optical sources, it is clear, as expected, that the stars have already acquired most of their final mass. The luminosities of the optical/infrared systems range from ~1 to 30 $L_\odot$, suggesting central masses of 0.5 to 1.5 $M_\odot$, whereas their circumstellar masses in Table 3 range from 0.013 to 0.1 $M_\odot$. The embedded systems have typical circumstellar masses of $\sim$ 0.4 $M_\odot$, with the largest one, NGC 1333 IRAS 4 A, near 2 $M_\odot$. The luminosities of the embedded systems range from $\sim$ 1 $L_\odot$ for VLA 1623 to $\sim$ 50 $L_\odot$ for NGC 1333 SVS 13.

Given the star formation regions in which they are found (NGC 1333 and Ophiuchi) and their luminosities, it is likely that the embedded sources are forming a range of stellar masses similar to that of the optical/infrared sources. In this case, the circumstellar masses are comparable to, and in several cases significantly less than, the probable current stellar masses. To see this, once can calculate the current stellar mass required to generate the observed luminosity via accretion. We assume that the mass accretion rate is the current circumstellar mass divided by one million years, $\dot{M} = M_{circ}/10^6$ years. The current stellar masses estimated in this way range from 0.4 to ~10 $M_\odot$. In systems at the high mass end, this simple estimate likely indicates that not all of their luminosities derive from accretion. Thus, even the embedded sources are likely to have already attained a significant fraction of their final stellar masses.

Table 4.3. Positions and Simple Estimates of Mass

Source	α (J2000)	δ (J2000)	Mass ($M_\odot$)
L1448 IRS3 A	$03^h25^m36^s.532$	$+30^\circ45'21''.35$	0.06
L1448 IRS3 B	$03^h25^m36^s.339$	$+30^\circ45'14''.94$	0.42
L1448 IRS3 C	$03^h25^m35^s.653$	$+30^\circ45'34''.20$	0.08
NGC1333 IRAS2 A	$03^h28^m55^s.571$	$+31^\circ14'37''.22$	0.30
NGC1333 IRAS2 B	$03^h28^m57^s.349$	$+31^\circ14'15''.93$	0.10
SVS 13 A1	$03^h29^m03^s.750$	$+31^\circ16'03''.95$	0.37 [a]
SVS 13 A2	$03^h29^m03^s.374$	$+31^\circ16'01''.87$	0.37 [a]
SVS 13 B	$03^h29^m03^s.056$	$+31^\circ15'51''.67$	0.45
SVS 13 C	$03^h29^m01^s.951$	$+31^\circ15'38''.27$	0.08
NGC1333 IRAS4 A1	$03^h29^m10^s.510$	$+31^\circ13'31''.01$	1.98 [a]
NGC1333 IRAS4 A2	$03^h29^m10^s.413$	$+31^\circ13'32''.20$	1.98 [a]
NGC1333 IRAS4 B	$03^h29^m11^s.988$	$+31^\circ13'08''.10$	0.65
NGC1333 IRAS4 C	$03^h29^m12^s.813$	$+31^\circ13'06''.97$	0.18
DG Tauri	$04^h27^m04^s.686$	$+26^\circ06'16''.14$	0.04
DG Tauri B	$04^h27^m02^s.562$	$+26^\circ05'30''.53$	0.05 [b]
L1551 IRS5 A	$04^h31^m34^s.143$	$+18^\circ08'05''.09$	0.10 [a]
L1551 IRS5 B	$04^h31^m34^s.141$	$+18^\circ08'04''.74$	0.10 [a]

Table 4.3—Continued

Source	α (J2000)	δ (J2000)	Mass ($M_{\odot}$)
HL Tauri	$04^{h}31^{m}38^{s}.413$	$+18^{\circ}13^{\prime}57^{\prime\prime}.61$	0.06
GG Tauri	$04^{h}32^{m}30^{s}.322$	$+17^{\circ}31^{\prime}40^{\prime\prime}.65$	0.04
GM Aurigae	$04^{h}55^{m}10^{s}.983$	$+30^{\circ}21^{\prime}59^{\prime\prime}.37$	0.01
VLA 1623 A	$16^{h}26^{m}26^{s}.396$	$-24^{\circ}24^{\prime}30^{\prime\prime}.45$	0.03
VLA 1623 B	$16^{h}26^{m}26^{s}.318$	$-24^{\circ}24^{\prime}30^{\prime\prime}.12$	0.02
IRAS 16293-2422 A	$16^{h}32^{m}22^{s}.869$	$-24^{\circ}28^{\prime}36^{\prime\prime}.11$	0.33
IRAS 16293-2422 B	$16^{h}32^{m}22^{s}.624$	$-24^{\circ}28^{\prime}32^{\prime\prime}.20$	0.42

[a] Close binary systems whose mass estimates include both systems.

[b] DG Tauri B observed at FWHM point of primary beam; thus masses given have a larger uncertainty than the rest of the survey.

4.6 Young Multiple Systems

All of the embedded sources in our survey are either part of small groupings or are in close binary systems. Even though our sample may be biased toward multiple systems due to the flux criteria, binary systems appear to be common in the earliest stages of star formation. The most favored mechanism for the early formation of binary and multiple stellar systems is fragmentation within either the initial cloud core or the circumstellar disk. Fragmentation during the earliest stages of the isothermal collapse of a cloud core, due to perturbations or non-spherical cores, can form binary systems with separations ranging from 10 to 10^4 AU (Boss & Bodenheimer 1979; Monaghan & Lattanzio 1986; Bonnell et al. 1991; Bonnell & Bastien 1992; Boss 1993; Bate, Bonnell, & Price 1995). Fragmentation due to $m = 1$ mode instabilities in the circumstellar disk may form binary systems with separations ranging from 10 $R_\odot$ to 100 AU (Adams, Ruden, & Shu 1989; Shu et al. 1990; Bonnell 1994; Bonnell & Bate 1994). In our survey, the majority of the circumstellar mass in embedded systems is in the large-scale envelope, with very little mass, if any, in circumstellar disks. This would suggest that fragmentation occurred during the early evolution of the core.

It has been pointed out that binary formation mechanisms have a dependence on the initial conditions of the pre-collapse cloud, favoring binary production in low-temperature star formation regions (Durisen & Sterzik 1994). Since most of our deeply embedded systems are located in the Perseus or Ophiuchus regions, our survey may be biased toward objects resulting from early cloud fragmentation. In addition, the Perseus clouds are distant enough that we would not detect close (< 150 AU separation) binary systems, the primary regime of the disk fragmentation. Of the optical sources in our survey, all of which are located in the Taurus cloud, only two appear to be binary systems—GG Tauri and L1551 IRS5. Both of these sources could have been formed by disk fragmentation since they both share a common circumbinary structures.

Let's return now to the point that all of our embedded sources are multiples. This result follows the general trend of increasing multiplicity in younger systems (Ghez et al. 1997), but what does it mean? Two possible explanations for the large number of embedded binary systems are: (1) there is a selection effect in our sample, such that binary, embedded sources were preferentially chosen, or (2) the majority of stars form in multiple systems, some of which break apart as they evolve. On the first point, a selection effect may exist if binary systems typically have more massive envelopes than single star systems, making embedded binary systems brighter at millimeter wavelengths. This supposition is opposite to the trend seen in older, optical T Tauri binaries; studies of these systems (Beckwith et al. 1990; Jensen, Mathieu, & Fuller 1994, 1996; Osterloh & Beckwith 1995) provide statistical evidence that T Tauri binary systems have less millimeter emission than single systems. These works posit that binary systems may destroy, or truncate, the circumstellar disks in the system resulting in less circumstellar material. So, as a young binary system evolves, the emission properties might change dramatically— young embedded binary systems could be brighter millimeter sources than coeval single star systems, because they have more massive envelopes. As they evolve, their envelopes disappear and less material is maintained in circumstellar disks then in single star systems, and they become less bright at millimeter wavelengths than comparable single star systems. Data on more embedded systems are needed to test this possibility.

On the second point, even if stars are predominately formed in binary or multiple systems, they may evolve into both binary and single star systems. Our criteria for identifying multiple systems is lax; system separations of 2000 AU or more, are relevant for forming stars since the mass reservoir of cloud material that the forming star draws from must typically be several thousand or more AU.

In addition, reasonable radial velocity association is nearly guaranteed by the association with the molecular cloud. As the systems evolve, the loss of the envelope mass and interactions with other stars forming in the cloud provide mechanisms for unbinding loose binary systems. Recent speckle observations of the Hyades cluster, which is a young main-sequence cluster, find that the occurrence of binary systems is larger there than in the local solar neighborhood but less than the Taurus clouds (Patience et al. 1998). Since our survey of the youngest objects suggest that most are in binary systems, it is possible, that binaries and multiple systems become less common as the systems age. Confirmation of this trend requires broader survey work. A recent study of additional optical clusters did not confirm the trend of decreasing binary occurrence with age (Patience 1998); this leaves open the possibility that attrition of binary systems occurs during the embedded stage of evolution.

Morphologically, we can identify three types of multiple systems in our sample: independent envelope, common envelope, and common disk systems. The characteristics of the different systems are defined by the broad distribution of the circumstellar material. Independent envelope systems exhibit clearly distinct centers of gravitational concentration with separations of $\geq$6000 AU; the components are within a larger surrounding core of low density material. Common envelope systems have one primary core of gravitational concentration which breaks into multiple objects at separations of 100 - 3000 AU. Common disk systems have separations of $\leq$ 100 AU and typically have circumbinary disk-like distributions of material. Table 4 lists the binary systems with our classification, their association, and the projected separation. The number assigned in Table 4 identifies the members of common envelope or common disk systems. Our sample has nearly an equal number of independent envelope and common envelope or disk systems.

Table 4.4. Multiple System Morphology

Source	Type	Assoc.	Separation	
			Arcsec	AU
L1448 IRS3 A	common envelope	1	6.″87	2404
L1448 IRS3 B	common envelope	1	6.″87	2404
L1448 IRS3 C	separate envelope		17.″13	5995
NGC1333 IRAS2 A	separate envelope		31.″20	10920
NGC1333 IRAS2 B	separate envelope		31.″20	10920
SVS 13 A1	common envelope	2,3	5.″25	1838
SVS 13 A2	common envelope	2,3	5.″25	1838
SVS 13 B	common envelope	3	10.″98	3843
SVS 13 C	separate envelope		19.″50	6825
NGC1333 IRAS4 A1	common envelope	4	1.″72	602
NGC1333 IRAS4 A2	common envelope	4	1.″72	602
NGC1333 IRAS4 B	separate envelope		29.″74	10409
NGC1333 IRAS4 C	separate envelope		10.″64	3724
L1551 IRS5 A	common disk	5	0.″35	49
L1551 IRS5 B	common disk	5	0.″35	49
GG Tauri	common disk	6	0.″25	35
VLA 1623 A	common envelope	7	1.″11	178
VLA 1623 B	common envelope	7	1.″11	178
IRAS 16293-2422 A	common envelope	8	5.″14	822
IRAS 16293-2422 B	common envelope	8	5.″14	822

There are several clear connections between these morphological distinctions and other works. The study of the separation distribution of optical binary by Larson (1995) found a knee in the distribution at 0.04 pc (8250 AU) which was identified with the Jeans size. Larson suggested that systems on that scale and larger, formed by fragmentation and separate collapse, exactly the structure found in the independent envelope systems. This scenario of prompt initial fragmentation is not new (e.g. Larson 1978, Pringle 1989, Bonnell et al 1991); it was discussed recently by Bonnell et al (1997) in the context of small cluster formation. The critical issue is that the collapse is initiated in a system which contains multiple Jeans masses in a weakly condensed configuration; one example of such a system might be a prolate Gaussian distribution with several Jeans masses along the long axis and one Jeans mass across the short axes.

The common envelope systems can be linked with models for the fragmentation of moderately centrally-condensed spherical systems (Boss 1995, Boss 1997, Burkert & Bodenheimer 1993). In this case, the models find fragmentation in the dense central region within an overall single core. The primary requirement for fragmentation is that the central region have a fairly flat distribution, but evidence of this flat region is erased once the fragmentation and collapse occurs. Thus, the forming multiple system is embedded within a single centrally condensed core. Finally, the common disk systems are similar to models of high angular momenta systems (Artymowiez & Lubow 1994; Bate & Bonnell 1997). The close stellar systems represent the fragmentation of early disks. The distribution of material between circumstellar and circumbinary structures depends sensitively on the angular momentum of the infalling material.

4.7 Conclusions

We have presented the first sub-arcsecond millimeter wavelength survey of the dust continuum emission toward 24 young stellar systems. The target sources range from young embedded objects to older optical/infrared sources. The optical systems show compact emission from circumstellar disks that is less than 1 arcsecond. In two cases, the circumstellar disk is resolved. The embedded systems show continuum emission that is dominated by emission from circumstellar envelopes, with little residual emission at small scales. This suggests that the circumstellar envelopes of the embedded systems are the dominant mass reservoir of material. If there is a circumstellar disk in these systems, it is not over-massive compared to a power-law envelope extended to small scales.

We make simple mass estimates of the circumstellar mass (not including the star) in the systems. The embedded sources have more circumstellar mass in the system (from 0.06 to 1.98 $M_{\odot}$) than the optical/infrared sources (from 0.01 to 0.06 $M_{\odot}$). The optical sources must have already accreted most of their stellar mass since the remaining circumstellar mass reservoir is small. Through simple arguments, we suggest that the embedded systems have accreted a significant fraction of their final stellar mass due to their luminosity and circumstellar mass.

The survey has a large number of multiple systems; all of the embedded systems are in small groupings or binary systems. Morphologically we separate our sample into three types of multiple systems: independent envelope, common envelope, and common disk systems. The independent envelope multiple systems have separations $\geq$ 6500 AU, which is the size scale, as suggested by Larson (1995), of independent collapse of initially fragmented clouds. The common envelope systems have separations 100-3000 AU, which is an expectation of a moderately centrally condensed spherical system. Finally, the common disk systems have separations ≤ 100 AU, which is similar to high angular momentum systems (Artymowiez & Lubow 1994; Bate & Bonnell 1997).

We thank the Hat Creek staff for their efforts in the construction and operation of the long baselines array. We especially thank Pedro Safier for discussions on cloud collapse. We also thank Eve Ostriker and Steve Lubow for useful discussions. This work was supported by NSF Grants NSF-FD93-20238 and AST-9314847. LGM acknowledges support from NASA grant NAGW-3066.

Chapter 5

Detailed Modeling of Source Structures

5.1 Overview: Modeling Envelopes and Disks

In this chapter, we will discuss the modeling of the $\lambda = 2.7$ mm continuum emission for many of the sources in the survey presented in Chapter 4 (Looney, Mundy, & Welch 1998; hereafter called Paper I). All modeling of the emission is performed in the *u,v* plane, taking advantage of the inherent spatial filtering properties. The image plane is not as useful to constrain the models because images, such as those presented in Paper I, are processed by the non-linear CLEAN process, and the spatial sensitivity is driven by *u,v* sampling or weighting used to obtain the synthesized beam. By modeling in the *u,v* plane, we deal directly with the measurement made at the interferometer. The goal of the *u,v* modeling is to understand the model parameter space, determine which factors have the most impact on the models, and to explore the uncertainty in the results. Due the high resolution and signal-to-noise necessary to model the circumstellar disk, this chapter will focus upon the envelopes of the embedded systems and the circumstellar disks of the three brightest optical/infrared systems (HL Tauri, DG Tauri, and GG Tauri).

5.2 Introduction to Modeling of Envelopes

The gravitational contraction or collapse of a cloud core to form a star has been the subject of considerable theoretical study. Larson (1969) showed in numerical simulations that collapse solutions remain isothermal and self-similar over a wide range of density and spatial scales. Larson (1969), and independently Penston (1969), found an analytical solution (the LP solution) to the isothermal sphere collapse problem. The solution is characterized by an uniform density central region surrounded by a density profile of $\rho \propto r^{-2}$. As the collapse progresses, the uniform density region shrinks until the entire sphere has a density profile of $\rho \propto r^{-2}$. At this time, defined as t=0, a point source with finite mass has formed at r=0. In addition, the infall velocity, which began at zero, is 3.3 times the local sound speed in the outer radii. Hunter (1977) followed the LP solution in time through t=0 and found the central density profile tends toward a $r^{-3/2}$ law, and the velocity remains 3.3 times the local sound speed in the outer regions.

A different class of self-similar solutions was presented by Shu (1977). Shu starts with a singular isothermal sphere with density of $\rho = \frac{a^2 A}{4\pi G} r^{-2}$, where a is the local sound speed, A is a dimensionless constant, and G is the gravitational constant. The sphere is unstable due to the infinite central density, and a collapse wave begins in the center and moves outward at the local sound speed, often called the “inside-out” collapse. As the collapse wave moves outward, the density profile inside the wave approaches a free-fall density profile, $\rho \propto r^{-3/2}$. One of the most attractive aspects of this solution is that the collapse is characterized by a single variable: the local speed of sound, which is measurable in principle. In this model, the mass infall rate is constant with time, $\dot{M} = \frac{0.975 a^3}{G}$.

Hunter (1977) and Whitworth & Summers (1985) showed that there was actually a continuum of self-similar solutions with the LP and Shu solutions as opposite limits in parameter space. Foster & Chevalier (1993) found, when simulating the collapse with marginally stable equilibrium Bonner-Ebert spheres, that the density profile and velocities at small radii tended toward the LP solution, not the Shu solution. At large times, the calculated models are all consistent with each other, but the Shu solution remains the most commonly used solution, especially the property of the constant mass infall rate.

The differences between the two solutions are subtle but important. The LP solution begins before a finite core is formed and the Shu solution begins at the moment a core has formed at r=0. Thus, when the $\rho \propto r^{-2}$ density profile is established, the two solutions have distinct velocity profiles: 3.3 times the local sound speed for the LP solution or zero for the Shu solution. However, both solutions have a density profiles of $\rho \propto r^{-2}$ when the finite core forms, and both tend toward free-fall density profiles of $\rho \propto r^{-3/2}$ afterwards. The biggest difference between the two solutions is the general morphology of the collapse. The Shu solution is an “inside-out” collapse with a constant mass infall rate; the collapse begins in the center and moves outward at the local sound speed. The LP solution collapses all a once, but due to the uniform density profile at small radii, the peak velocity is not in the center, as in the Shu solution, but at a finite radius, so the mass infall rate is not constant; at the beginning of the collapse, the mass infall rate of the LP solution is larger than the Shu solution, then the mass infall rate asymptotically approaches the Shu value. Therefore, given a specific free-fall density profile radius where $\rho \propto r^{-3/2}$, the mass of the central protostar in the LP solution can be larger than the mass predicted by the Shu solution.

As presented in Paper I, we have imaged 24 young stellar sources with sensitivity in spatial scales of $0\farcs5$ to $50''$ in the $\lambda = 2.7$ mm continuum. In this chapter, we address the modeling of the envelope emission for many of the embedded objects from Paper I. We will approach the problem by trying to address three issues in the fits. (1) What constraints can we place on the power-law of the density? Does the power-law index resemble the isothermal sphere ($\rho \propto r^{-2}$) or the free-fall profile ($\rho \propto r^{-3/2}$)? Or something else entirely? For example, Ward-Thompson et al. (1994) found that starless clouds tended to have flat-topped density profiles, more like Bonner-Ebert spheres. However, for Class 0 sources this is the first time that modeling of the envelope can be done down to sub-arcsecond resolution, and the first time that the power-law index is fit, instead of assumed from a model. (2) What constraints can we place on the circumstellar disks in these systems? With the highest resolution to date at these wavelengths, we will be able to place limits on the size of the embedded disk. Can the data be fit with or without a central circumstellar disk? (3) What constraints can we place on the inner and outer radii of the envelopes?

5.3 The Envelope Fitting Procedure

In order to simplify the computations and compare to theoretical discussions, we use a spherically symmetric envelope model. We calculate the observed continuum flux by performing the radiative transfer through the envelope by ray-tracing.

As discussed in §2.4, a power-law radial dependence in the image plane transforms to a power-law in *u,v* distance in the *u,v* plane. The slope of the power-law in a log-log plot of *u,v* distance versus amplitude is related to the sum of the density and temperature power-laws as long as the emission is optically thin,

$$B(r) \propto r^{-(p+q)+1} \quad \rightarrow \quad V(\beta) \propto \beta^{(p+q-3)},$$

where β is *u,v* distance (see §2.4). When the envelope is truncated at a finite radius, the cutoff is equivalent to the convolution of a modified first-order Bessel function with the power-law in the *u,v* plane, causing a flattening of the slope at short *u,v* spacings and a ringing effect in the *u,v* distance versus amplitude plot (see §2.4). (Note that the ringing effect arises from a sharp edged envelope which is probably not physical.) If the inner region of the envelope becomes optically thick, the slopes at large *u,v* spacing will grow steeper. Thus, while the simple power-law relation gives a good qualitative feel for the behavior in *u,v* space, a full numerical model is needed to fit observational data.

The model, as discussed in §1.6 with power-law assumptions, has five degrees of freedom: power-law of the density (p), total mass of the envelope (M) which is needed to determine ρ_o, inner cutoff radius (R_i), outer cutoff radius (R_o), and point source flux (S_p). For each source, we explore a grid of parameter space including: p from 0.5 to 2.9 in steps of 0.2, R_o from 1000 AU to 10000 AU in steps of 1000 AU, R_i of 1 AU, 40 AU, and 80 AU, and central point source flux (S_{ps}) in 1σ steps (σ = rms noise in the last *u,v* distance amplitude bin) starting at no point source, up to a maximum of the amplitude in the last *u,v* distance bin. For each model, the envelope emission is calculated; as an image, the point source flux is correctly attenuated by the envelope; and the model is multiplied by the BIMA primary beam to account for the loss of large-scale structure. The model is then Fast Fourier Transformed (FFTed) and sampled with the same *u,v* spacings as the data. The data and model are then both vector averaged in *u,v* distance bins, and the amplitude for each bin is compared by calculating the reduced χ^2. For each model parameter p, R_i, R_o, and S_{ps}, χ^2 is minimized with respect to the envelope mass.

5.4 Envelope Results

Figures 5.1 to 5.11 show the source data in log(*u,v* distance) versus log(amplitude) plots. For both the models and the data, the complex visibility quantities are vector averaged over annuli in the *u,v* plane, centered at the source positions given in Paper I. The error bars on the figures are the statistical error bars based on the standard deviation of the mean of the data points in the bin, with a minimum of 10%, reflecting the uncertainty in the overall calibration. In each figure, there are four models overlaid on the data to show how the best fit model changes with increasing density power-law, p. We only considered models with a reduced $\chi^2 \leq 1.5$, which corresponds to a confidence level of 95% for the typical source, to be acceptable fits.

5.4.1 L1448 IRS3

L1448 IRS3, the brightest infrared source in the L1448 cloud (Bachiller & Cernicharo 1986), is comprised of three distinct sources in the λ=2.7mm continuum (Terebey, Chandler, & André 1993; Terebey & Padgett 1997; Figure 7 Paper I). Source B, the second brightest source at centimeter wavelengths (Curiel et al. 1990), is the brightest source in the λ=2.7mm continuum. Sources A and B, a proto-binary system, share a common large-scale envelope. All three of the sources may be embedded in a larger envelope, but our data cannot place useful limits on this structure. In the λ = 2.7 mm high resolution image (Figure 7 Paper I), source B appears elongated both parallel and perpendicular to the L1448 IRS3 outflow.

Only source B can be modeled effectively. Sources A and C are too weak: the number of *u,v* bins with adequate signal-to-noise is insufficient to constrain the models. Source C was subtracted from the *u,v* data before source B was modeled. We did not subtract source A from the *u,v* data. This may introduce some errors, but we wanted to ensure that none of the circumstellar envelope was inadvertently subtracted out of the *u,v* data. Since the data is vector averaged, and source A is weak and located $\sim 7''$ from source B, not subtracting source A has minimal effect; the general trend of the data should not be altered. In addition, we assume that the circumbinary envelope is centered on source B.

Figure 5.1 displays the *u,v* data for L1448 IRS3 B (the open squares). The curve is smooth with a well defined slope of -0.3 within the inner 40 kλ (corresponding to p $\sim$2.3 for an infinite power-law envelope; see §2.4). At 40 kλ, there is an inflection point, and the curve transitions into a steeper slope of -1.1 (corresponding to p $\sim$1.9 for an infinite envelope). In fact, the 40 kλ inflection point is an important constraint on the simple power-law models. Despite the distinct slopes, the data can be well fit. As shown in Figure 5.1, acceptable models (reduced $\chi^2 \leq 1.5$) span p = 2.1 to 2.7, with the best models having p = 2.5; with our χ^2 cutoff, p $\leq$ 1.9 and p > 2.9 are excluded. Table 5.1 lists the acceptable parameters for L1448 IRS3 B.

The best family of models is the P = 2.5 family, which overall has the lowest χ^2 values. In the lower left panel of Figure 5.1, the p = 2.5 model perfectly follows the slope of the inner *u,v* spacings. The only point that is not well fit is the 40 kλ bin. However, the 40 kλ bin is a vector average of *u,v* spacings ranging from 30 kλ to 50 kλ, or fringe spacings of around $7''$ to $4''$, respectively. Since the binary system has a separation of $7''$, the 40 kλ *u,v* bin may be artificially high. With the larger density power-law models (p = 2.3 and higher), the outer radius is not well constrained since the models have a very centrally concentrated mass distributions. In all cases, a 1000 AU outer radius was excluded.

The p = 2.1 family of models is probably the least robust of the models displayed, having reduced χ^2 values near 1.5. To fit the inner *u,v* slope, the

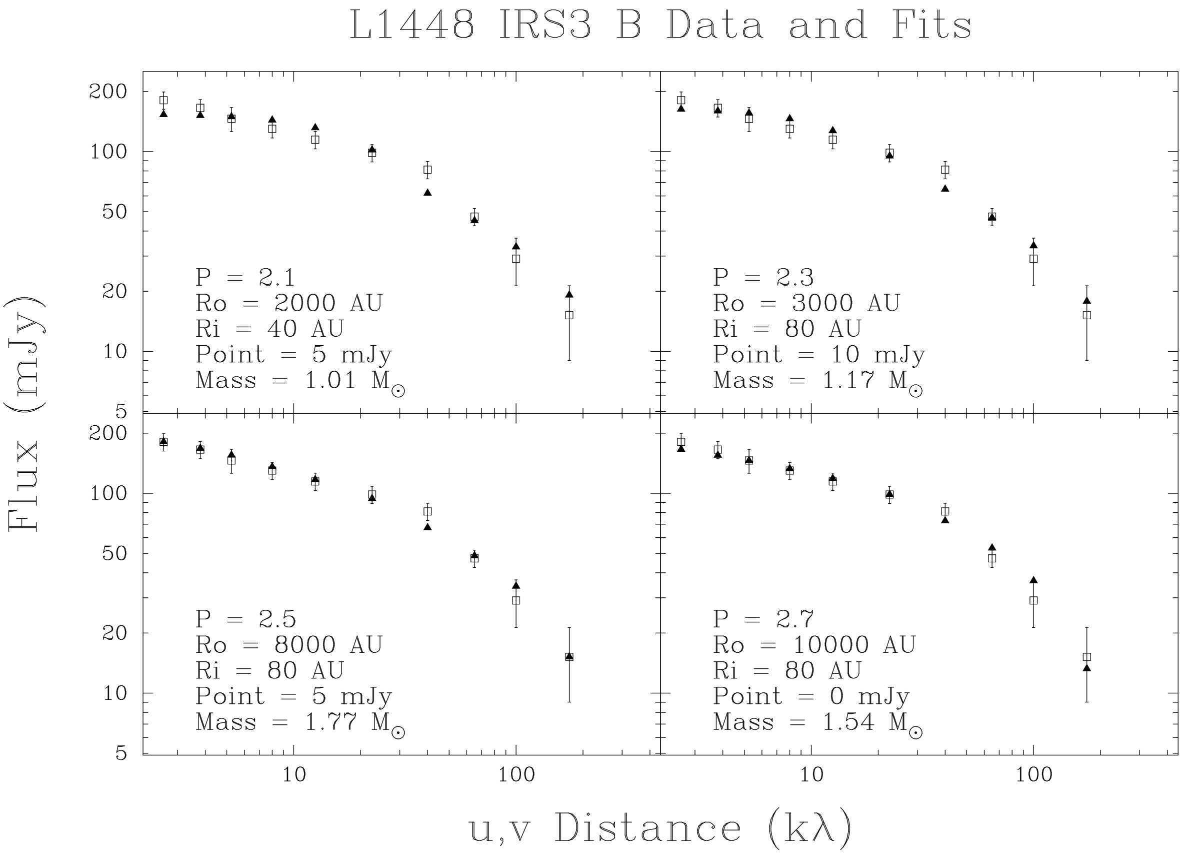

Fig. 5.1. The u,v data binned in annuli around L1448 IRS3 B and four fits to the data using a standard envelope model, $\rho \propto (\frac{r}{1AU})^{-p}$ and $T(r) = T_o(\frac{r}{1AU})^{-0.4}$ where T_o = 380 K, plus a point source.

Table 5.1. L1448 IRS3 B Fit Summary

p index	R_i (AU)	R_o (AU)	S_{ps} (mJy)
2.1	40	2000	5
		3000	10
2.1	80	2000	15
2.3	40	2000	0
		3000	0,5
		4000-10000	0,5,10
2.3	80	2000	5,10
		3000-4000	5,10,15
		5000-9000	10,15
		10000	15
2.5	40	5000-10000	0
2.5	80	2000	0,5
		3000	0,5,10
		4000-10000	0,5,10,15
2.7	80	3000	0
		4000-9000	0,5
		10000	0,5,10

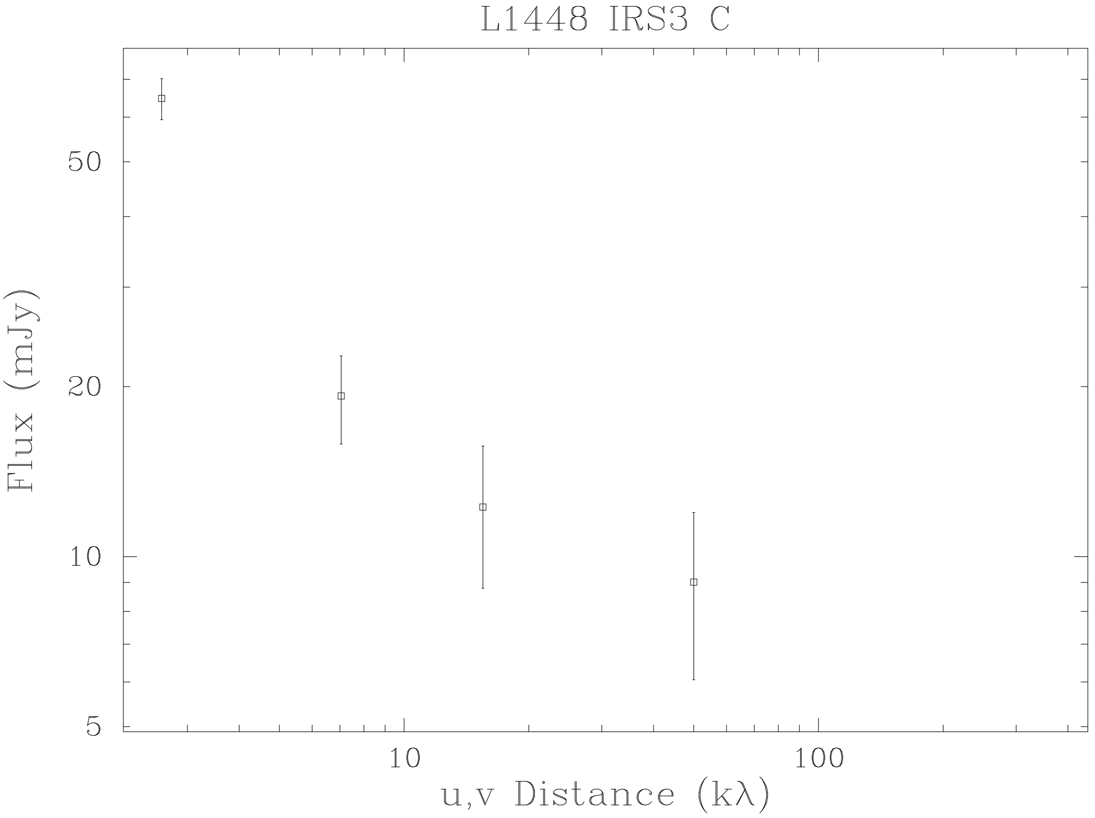

Fig. 5.2. The u,v data binned in annuli around L1448 IRS3 C.

p = 2.1 models require small envelopes. A small envelope will look like a point source to the inner *u,v* spacings; the upper left panel shows a flat profile in the inner *u,v* region, which intersects the data. By using a small envelope, the model approximates a less steep inner *u,v* power-law. As the interferometer resolves the compact envelope, the steeper p = 2.1 power-law becomes evident > 20 kλ.

All of the acceptable models have inner holes in the envelope. Again this is due to the high p values that are required to fit the shallow slope of the inner *u,v* spacings. The slope is so flat that an envelope with no inner cutoff would have an excess of emission at the larger *u,v* spacings; with the steep density power-law, there would be a significant amount of material within the central region that would overestimate the flux.

Although L1448 IRS3 C does not have enough signal-to-noise to model accurately, Figure 5.2 presents the *u,v* bins with amplitudes of $\geq 3\sigma$. The sharp drop of amplitude with *u,v* distance in Figure 5.2 implies that the source is extended; the continuum emission is dominated by the envelope component.

5.4.2 NGC 1333 IRAS 2

The young system NGC 1333 IRAS2 (Jennings et al. 1987) is located in a very active region of star formation in Perseus (Strom, Vrba, Strom 1976; Aspin, Sandell, & Russell 1994; Sandell et al. 1994; Bally et al. 1996; Lada, Alves, & Lada 1996; Warin et al. 1996). NGC 1333 IRAS 2 has two associated outflows; the "N-S" outflow has a principal axis of $\sim 25^\circ$ (Liseau, Sandell, & Knee 1988) and the "E-W" outflow has a principal axis of $\sim 104^\circ$ (Sandell et al. 1994). The source is actually a multiple system with a separation of $\sim 31''$ (Blake 1997). The northern source (source A) powers the "E-W" outflow, and the southern source (source B) is responsible for the "N-S" outflow.

Source A is the brightest and most extended of the two objects (Paper I). In the λ = 2.7 mm high resolution image (Figure 8 Paper I), the envelope of source A appears to be completely resolved out, and the remaining emission is consistent with a point source. Source B was suggested to be a compact source at λ=2.7mm from Figure 17 in Paper I. In the λ=2.7mm high resolution image (Figure 9 Paper I), source B appears to be slightly resolved perpendicular to the "N-S" outflow. There may be an extended envelope that surrounds both of the sources, but our data can not place useful limits on this structure; it is ignored in the modeling.

In Figure 5.3, the *u,v* data are shown for NGC 1333 IRAS 2 A, after subtraction of source B from the *u,v* data. The curve has a well defined slope of -0.4 within the inner 12 kλ (corresponding to p ~2.2 for an infinite power-law envelope). Unlike L1448 IRS3 B, the visibility at larger *u,v* distance flattens to a constant flux, rather than sharply descend. This indicates that the model point source component may play an important role in this source. A summary of fit parameters is shown in Table 5.2; the values of p are not well constrained, with acceptable models ranging from p = 0.5 to p = 2.3 and a best fit model of p = 1.9. The majority of the acceptable models require a point source, but the models do not constrain the point source flux.

The best model families are the p = 1.7 through p = 2.1 models which trace the general trend of the data very well; most of these models have $\chi^2 \ll 1$. The p = 0.5 family of models give acceptable χ^2, but as can be seen in Figure 5.3, these models require a small envelope to simulate the slope in the 5 kλ to 20 kλ region; the fit is not reflecting the slope due to p+q, but rather the falloff from beginning to resolve the overall structure. The flatness of the model in the outer *u,v* spacings is entirely due to the embedded point source. Similarly, the p = 1.5 family requires small envelopes to fit the inner *u,v* spacings. As the density power-law becomes steeper (toward p = 2.3), the models underestimate the inner

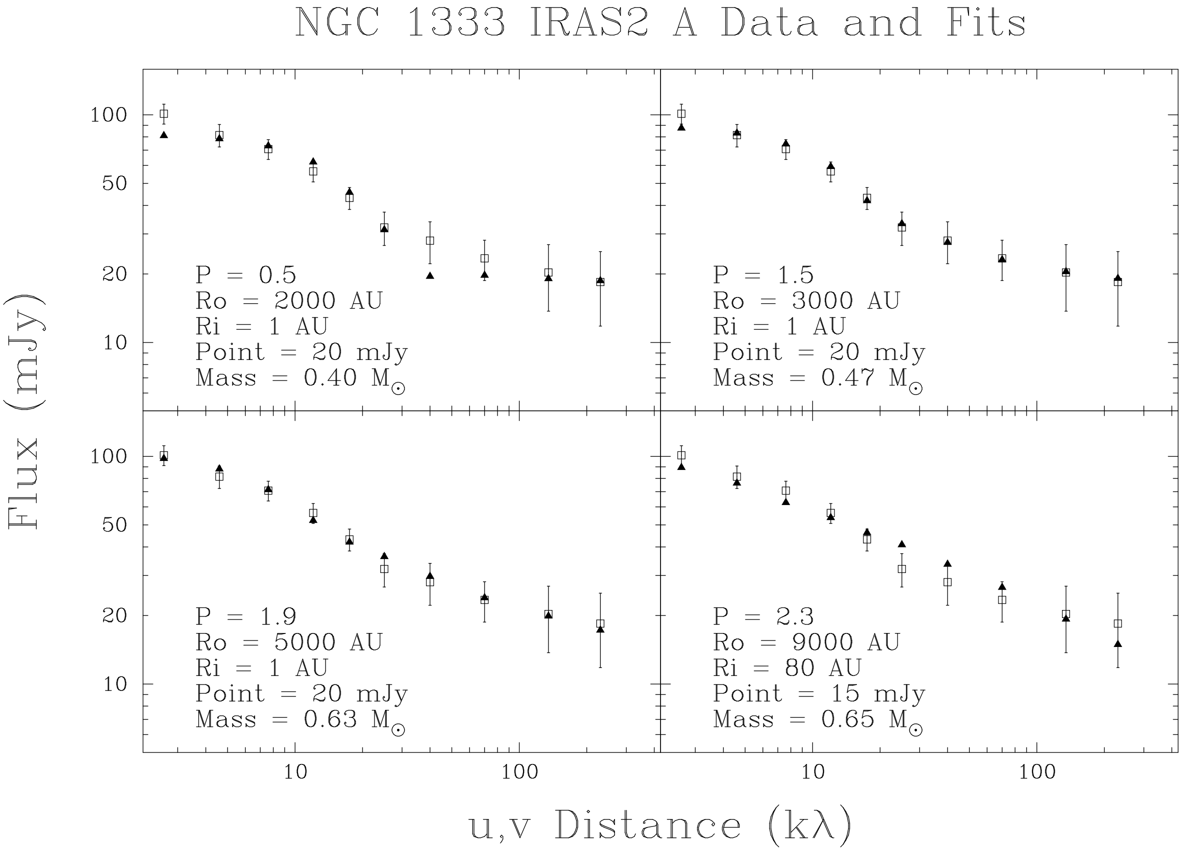

Fig. 5.3. The *u*,*v* data binned in annuli around NGC 1333 IRAS 2 and four fits to the data using a standard envelope model, $\rho \propto (\frac{r}{1AU})^{-p}$ and T(r) = $T_o(\frac{r}{1AU})^{-0.4}$ where $T_o = 555$ K, plus a point source.

Table 5.2. NGC 1333 IRAS2 A Fit Summary

p index	R_i (AU)	R_o (AU)	S_{ps} (mJy)
0.5	1,40,80	2000	20
0.7	1,40,80	2000	20
0.9	1,40,80	2000-3000	20
1.1	1,40,80	2000-3000	20
1.3	1,40	2000-3000	13,20
		4000	20
1.3	80	2000	13
		3000	13,20
		4000	20
1.5	1,40,80	3000	13,20
		4000-5000	20
1.7	1	3000	7,13,20
		4000-5000	13,20
		6000-8000	20
1.7	40	3000	7,13,20
		4000-5000	13,20
		6000-9000	20
1.7	80	3000-5000	13,20
		6000-8000	20

Table 5.2—Continued

p index	R_i (AU)	R_o (AU)	S_{ps} (mJy)
1.9	1	3000-4000	0,7,13,20
		5000-6000	7,13,20
		7000-10000	13,20
1.9	40	3000-6000	7,13,20
		7000-10000	13,20
1.9	80	3000-4000	7,13,20
		5000-10000	13,20
2.1	1	3000-10000	0,7,13,20
2.1	40	3000	7,13
		4000	0,7,13
		5000-7000	0,7,13,20
		8000-10000	7,13,20
2.1	80	3000	7,13
		4000-10000	7,13,20
2.3	1	5000-10000	0,7,13,20
2.3	40	4000-5000	0,7
		6000-10000	0,7,13
2.3	80	4000-8000	7,13
		9000-10000	7,13,20

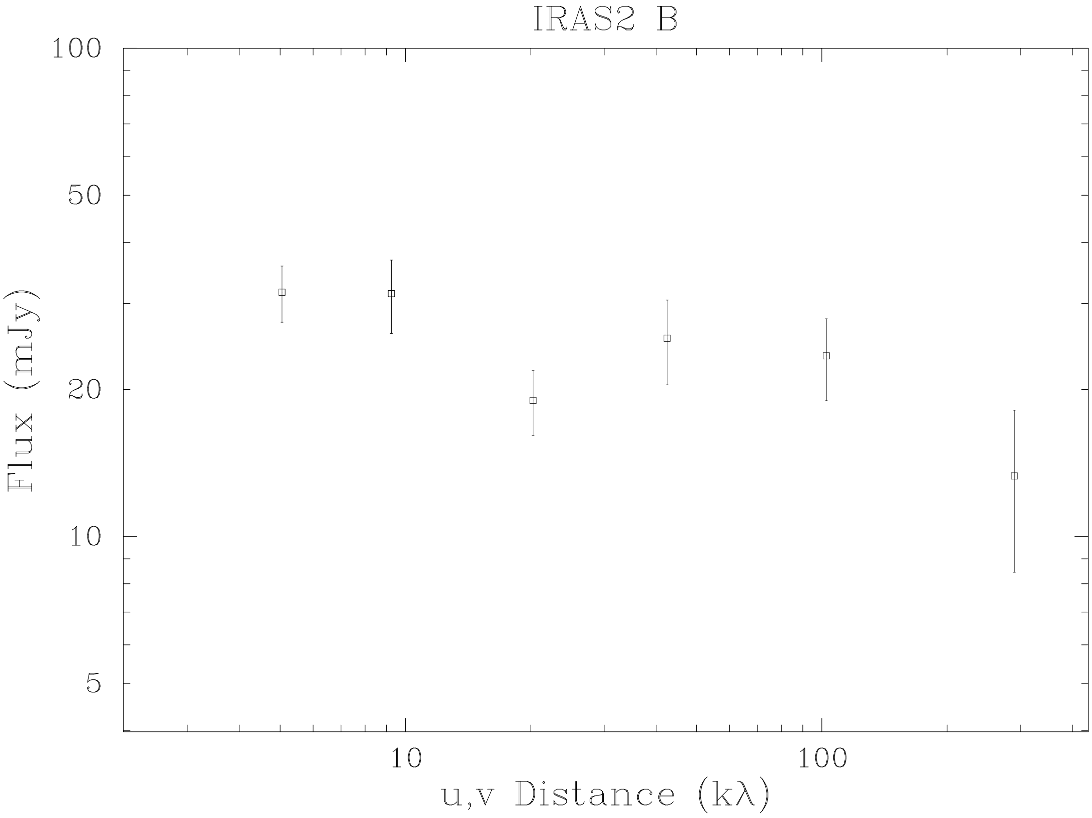

Fig. 5.4. The *u*,*v* data binned in annuli around NGC 1333 IRAS2 B.

and outer *u,v* range flux and overestimate the middle *u,v* range flux.

Figure 5.4 shows the *u,v* distance and amplitude plot for NGC 1333 IRAS2 B. As suggested in Figure 17 of Paper I, IRAS2 B is a compact source; the amplitude does not significantly drop off until around 100 kλ. The modeling was performed for this source, but NGC 1333 IRAS2 B only has one data point with enough signal-to-noise in the $>$ 100kλ region; there are not enough constraints to distinguish a power-law effect from an outer radius effect. The slight dip in the visibility at 20 kλ may be an artifact from the subtraction of source A from the *u,v* data.

5.4.3 SVS 13

SVS 13 (Strom, Vrba, Strom 1976; also referred to as SSV13 in the literature from Herbig & Jones 1983) is located in Perseus southeast of NGC 1333 IRAS2. Coincident with NGC 1333 IRAS3 (Jennings et al. 1987), SVS 13 is comprised of four sources in the millimeter continuum (Grossman et al. 1987; Chini et al. 1997; Paper I). The spectacular outflow of HH objects HH 7-11 (Herbig, 1974) arises from either A1 or A2 (Rodríguez et al. 1997; Welch, Looney, & Mundy 1998), a 5$''$ proto-binary system. Sources A1, A2, and B may also be embedded in a larger-scale envelope (Welch, Looney, & Mundy 1998) that we will not attempt to model in this treatment.

Besides the large-scale envelope, sources A and B are surrounded by individual envelopes. In the case of source A, the separate envelope is probably a circumbinary envelope that enshrouds sources A1 and A2. In the $\lambda = 2.7$ mm high resolution images (Figures 10 & 11 Paper I), SVS 13 A1 and B are amorphous structures. Rodríguez et al. (1997) have suggest that the source we label as A2 may be the originator of the outflow. However, source A2 quickly resolves out of our images, and source A1 has an north-south extension that is perpendicular to the HH 7-11 jet, suggesting that source A1 is may be the better candidate. In the high resolution image of Figure 11 from Paper I, source B is consistent with a point source and an extension toward the south that may be a small jet.

In Figure 5.5, the *u,v* data are shown for NGC 1333 SVS 13 A, after subtraction of sources B and C from the *u,v* data. As mentioned above, sources A and B are embedded in a circumbinary envelope. We verified that the subtracted data was not contaminated by this large-scale envelope; the subtracted *u,v* data were remapped, and large scale emission was not detected in the image plane. Although there may exist some residual of the large-scale common envelope in the *u,v* data, vector averaging in *u,v* annuli minimizes its effect. Similarly, source A2 is a weak source that will quickly average out in the annular vector average.

The *u,v* data of Figure 5.5 flattens to a constant in the outer *u,v* spacings, more similar to IRAS2 A than L1448 IRS3 B. The curve has a well defined slope of -0.23 within the inner 8 kλ (corresponding to p $\sim$ 2.4 for an infinite envelope). At 8 kλ, there is an inflection point, and the curve transitions to a steeper slope of -0.85 (corresponding to p $\sim$ 1.75 for an infinite envelope). However, the transition is smooth and the data can be well modeled with a very wide range of density power laws: p = 0.5 to p = 2.1 (Table 5.3).

The critical data to fit is in the range of 10 kλ to 20 kλ. The best family of models for SVS13 A is the p = 0.9 models, which fit the critical slope region by a combination of density power-law slope and outer radius cutoff. The flattening out of the curve with increasing *u,v* distance, requires nearly all of the acceptable models to have embedded point sources.

As in the case of NGC 1333 IRAS2 A, Figure 5.5 can be fit acceptably with

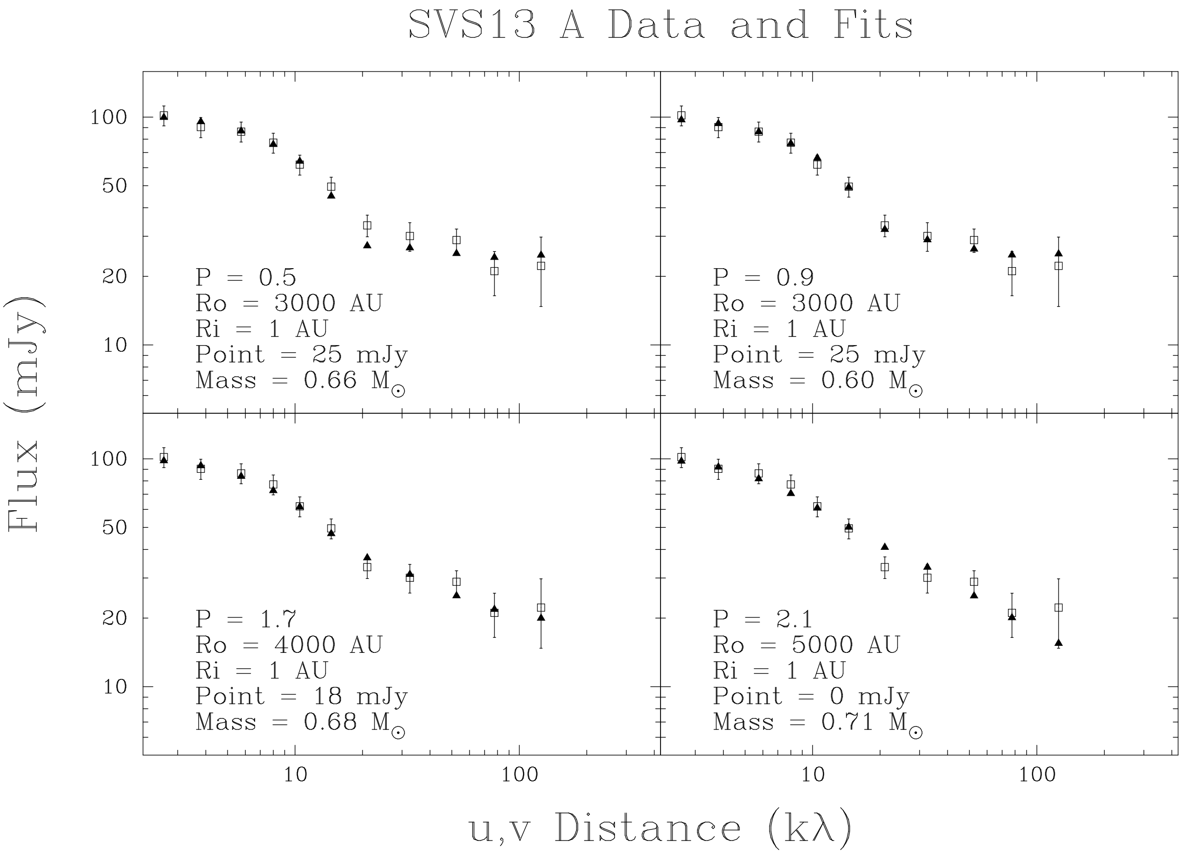

Fig. 5.5. The *u,v* data binned in annuli around SVS 13 A and four fits to the data using a standard envelope model, $\rho \propto (\frac{r}{1AU})^{-p}$ and T(r) = $T_o(\frac{r}{1AU})^{-0.4}$ where T_o = 487 K, plus a point source.

Table 5.3. SVS 13 A Fit Summary

p index	R_i (AU)	R_o (AU)	S_{ps} (mJy)
0.5	1,40,80	3000	25
0.7	1,40,80	3000	25
0.9	1,40,80	3000-4000	25
1.1	1,40,80	3000	18,25
	1,40,80	4000	25
1.3	1,40,80	3000-4000	18,25
	1,40,80	5000	25
1.5	1,40,80	3000	12,18,25
	1,40,80	4000	18,25
	1,40,80	5000	25
1.7	1,40,80	3000	12,18
	1,40,80	4000	12,18,25
	1,40,80	5000-6000	18,25
1.9	1	3000	6,12,18
		4000-5000	6,12,18,25
		6000-7000	12,18,25
		8000-9000	18,25
		10000	25

Table 5.3—Continued

p index	R_i (AU)	R_o (AU)	S_{ps} (mJy)
1.9	40	3000	6,12
		4000	6,12,18
		5000	12,18
		6000	18
		7000	12,18
		8000-9000	18
1.9	80	3000	12
		4000-7000	12,18
		8000-9000	18
2.1	1	5000	6,12,18,25
		6000-10000	0,6,12,18,25
2.1	40	4000	0,6
		5000-6000	0,6,12
		7000-10000	6,12
2.1	80	4000-6000	6,12
		7000	6,12,18
		8000-10000	12

a p = 0.5 model, but it is not likely a realistic solution. The p = 0.5 model requires a small radius to mimic a shallow slope in the inner *u,v* . The slope in the 7 kλ to 25 kλ region is not as extended as the slope for NGC 1333 IRAS2 A and there are less data to constraint the slope. In fact, the combination of outer cutoff and lower density index produces acceptable models for many density power-law indices. However, all of the models in the p = 0.5 family systematically underestimate the 12 kλ to 50 kλ data. At the other extreme, the p =2.1 models tend to overestimate the flux at the mid-ranged *u,v* spacings.

In Figure 5.6, the *u,v* data are shown for NGC 1333 SVS 13 B, after subtraction of sources A (both components) and C from the *u,v* data. The subtracted visibilities were checked for any large scale envelope contamination. There is a slight “bump” in the curve at 80 kλ, which corresponds to a fringe of around $3''$. This excess in amplitude may be a beating effect from incomplete subtraction of one of the other sources; or the excess may be from a non-spherical symmetric component of source B on a size scale of $\sim 3''$. In either case, the 80 kλ *u,v* point cannot be fit with the simple-model. This increases the reduced χ^2 and bias the amplitude upward in the outer parts of the *u,v* plane.

The slope of the *u,v* data from 5 kλ to 35 kλ is -0.6 (corresponding to p $\sim$2.0 for an infinite envelope). Indeed, this nicely defined slope is best fit by the p = 1.9 family of models (Figure 5.6). At the lower end of the acceptable models, the p = 1.3 models require smaller outer radii to fit the slope from 5 kλ to 35 kλ, but even with the smaller outer radius, the p = 1.3 models have too steep a slope for this *u,v* region. On the other side of p = 1.9, the p = 2.1 family of models have too shallow a slope in the same region. This figure nicely demonstrates the effect of the density power-law index in the *u,v* plane.

Most of the acceptable models for SVS 13 B, require a significant point source. In fact, for p = 1.3 to p = 1.9 (the better fit range of models) a zero

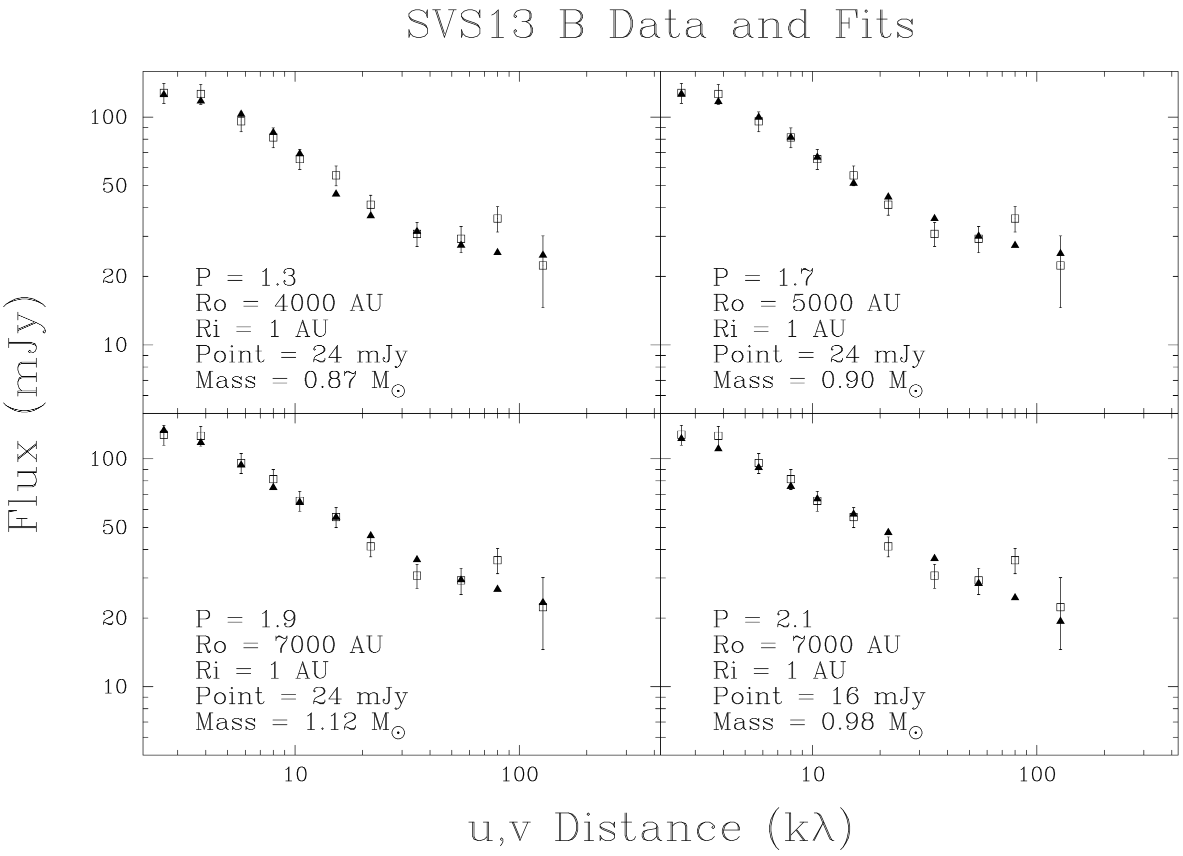

Fig. 5.6. The *u*,*v* data binned in annuli around SVS 13 B and four fits to the data using a standard envelope model, $\rho \propto (\frac{r}{1AU})^{-p}$ and T(r) = $T_o(\frac{r}{1AU})^{-0.4}$ where T_o = 512 K, plus a point source.

Table 5.4. SVS 13 B Fit Summary

p index	R_i (AU)	R_o (AU)	S_{ps} (mJy)
1.3	1,40,80	3000-4000	24
1.5	1,40,80	4000-6000	24
1.7	1	4000-8000	24
1.7	40	4000-6000	16,24
		7000-8000	24
1.7	80	4000-8000	24
1.9	1	5000-9000	16,24
1.9	40	5000-10000	16
1.9	80	5000	16
		6000-9000	16,24
		10000	24
2.1	1	6000	16
		7000-8000	0,8,16,24
		9000-10000	0,8,16
2.1	40	7000-10000	8

or 8 mJy point source is excluded. For the p = 2.1 family of models, the 1 AU inner cutoff allows any point source, a 40 AU inner cutoff can only be fit with a 8 mJy point source, and a 80 AU inner cutoff is excluded. This suggest that there is most likely a significant compact structure, a circumstellar disk, in this source.

5.4.4 NGC 1333 IRAS4

Perhaps the best know millimeter source in the NGC 1333 region is the IRAS4 system (Jennings et al. 1987). NGC 1333 IRAS4 is comprised of at least four distinct young stellar objects (Sandell et al. 1991; Lay, Carlstrom, & Hills 1995; Paper I). Source A, the northern source, is a $1\rlap{.}''7$ binary system that shares a common circumbinary envelope (Lay, Carlstrom, & Hills 1995; Paper I). Source B shows complicated visibility structure in the λ = 840 μm CSO-JCMT single baseline interferometric observations, and it was argued to be at least a binary and perhaps a triple or quadruple system (Lay, Carlstrom, & Hills 1995). However, they were not aware of source C, which may have confused their analysis. Source C is a compact source that has a brightness distribution that more resembles an optical/IR source than its IRAS 4 companions.

In Figure 5.7, the *u,v* data are shown for NGC 1333 IRAS 4 A1— the brighter source at λ=2.7mm in the $1\rlap{.}''7$ binary. For this figure, sources B and C were subtracted from the *u,v* data. We did not subtract out the binary companion source A2; running test models with a second fixed point source at the location of source A2 did not significantly alter the fits. The shortest *u,v* spacing data point in Figure 5.7 is excessively high. The best explanation is that the data are beginning to pick-up a large-scale structure. Since we are not including such a large-scale envelope in this modeling, we did not use the shortest *u,v* spacing to constrain our fits.

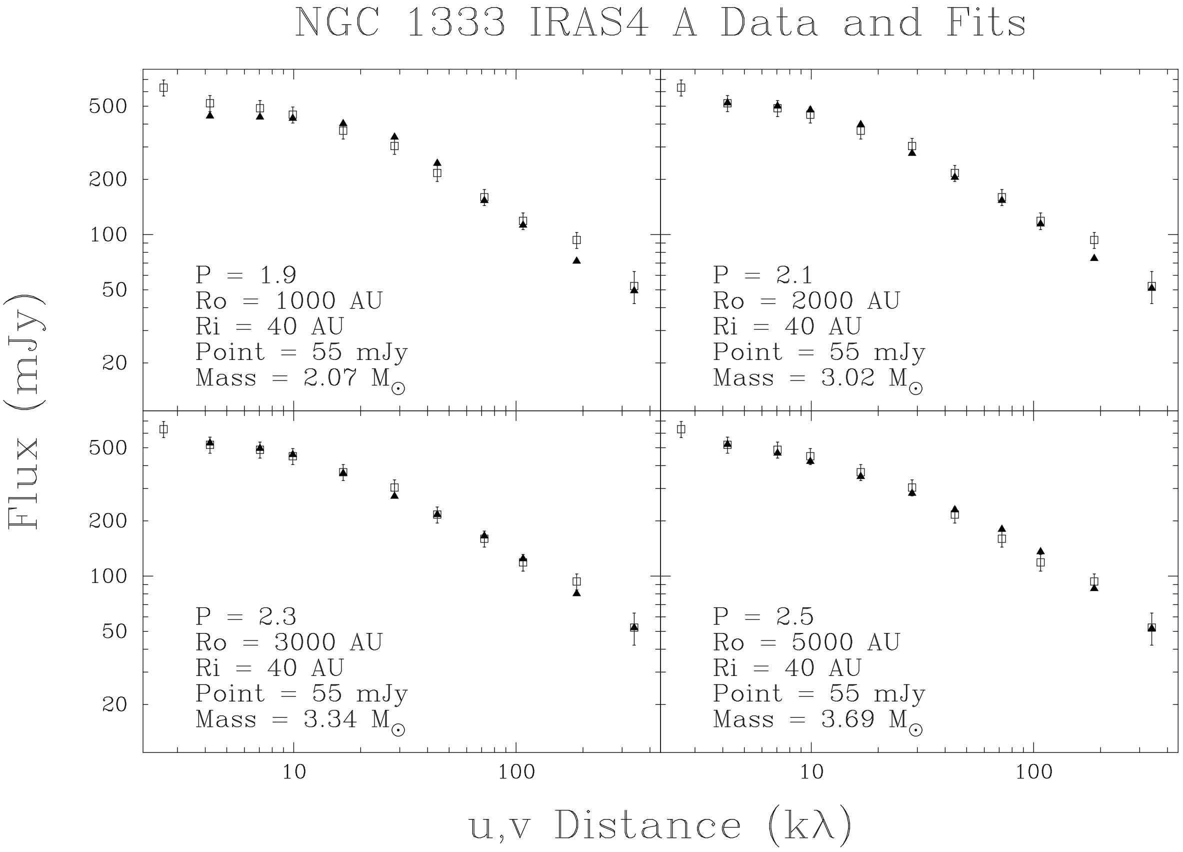

Fig. 5.7. The *u*,*v* data binned in annuli around NGC 1333 IRAS4 A and four models of the data using a standard envelope model, $\rho \propto (\frac{r}{1AU})^{-p}$ and T(r) = $T_o(\frac{r}{1AU})^{-0.4}$ where T_o = 457 K, plus a point source.

Table 5.5. NGC 1333 IRAS4 A Fit Summary

p index	R_i (AU)	R_o (AU)	S_{ps} (mJy)
1.9	40	1000	55
2.1	40	2000	44,55
		3000	44
2.3	40	2000-3000	33,44,55
		4000-10000	44,55
2.5	1	2000-10000	0,11,22,33,44,55
	40	2000	33,44,55
		3000-10000	22,33,44,55
	80	3000-10000	55

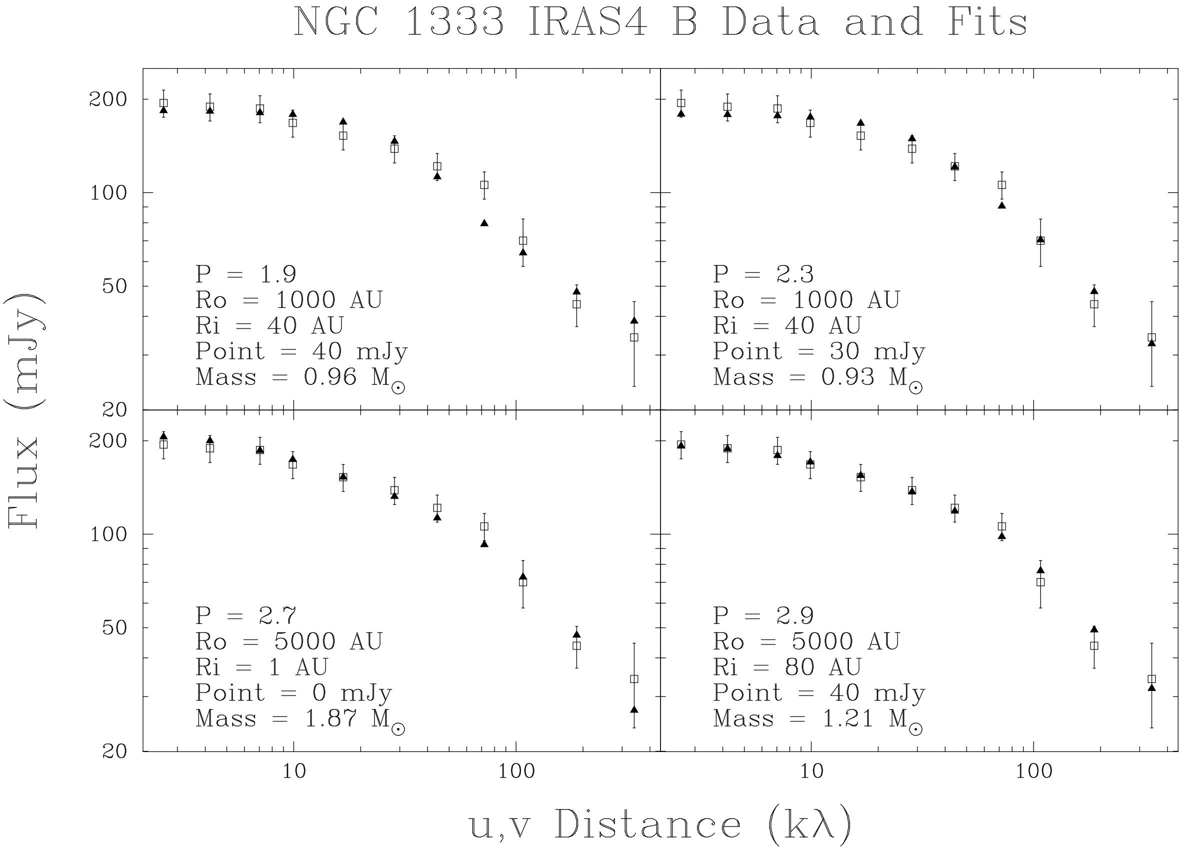

Fig. 5.8. The *u,v* data binned in annuli around NGC 1333 IRAS4 B and four models of the data using a standard envelope model, $\rho \propto (\frac{r}{1AU})^{-p}$ and T(r) = $T_o(\frac{r}{1AU})^{-0.4}$ where $T_o = 347$ K, plus a point source.

Table 5.6. NGC 1333 IRAS4 B Fit Summary

p index	R_i (AU)	R_o (AU)	S_{ps} (mJy)
1.9	40	1000	30,40
1.9	80	1000	40
2.1	40	1000	20,30,40
2.1	80	1000	40
2.3	1	1000	0,10,20,30,40
2.3	40	1000	10,20,30,40
		2000	30,40
		3000	40
2.3	80	1000	30,40
		2000	40
2.5	1	1000-4000	0,10,20,30,40
2.5	40	1000	0,10,20,30,40
		2000	10,20,30,40
		3000-5000	20,30,40
		6000-10000	30,40
2.5	80	1000-2000	30,40
		3000-6000	40

Table 5.6—Continued

p index	R_i (AU)	R_o (AU)	S_{ps} (mJy)
2.7	1	1000-10000	0,10,20,30,40
2.7	40	1000	0,10,20,30
		2000-10000	0,10,20,30,40
2.7	80	1000-2000	20,30,40
		3000-10000	30,40
2.9	1	1000-10000	0,10,20,30,40
2.9	40	1000	0,10,20
		2000-3000	0,10,20,30
		4000-9000	0,10,20,30,40
		10000	0,10,20,30
2.9	80	1000-10000	20,30,40

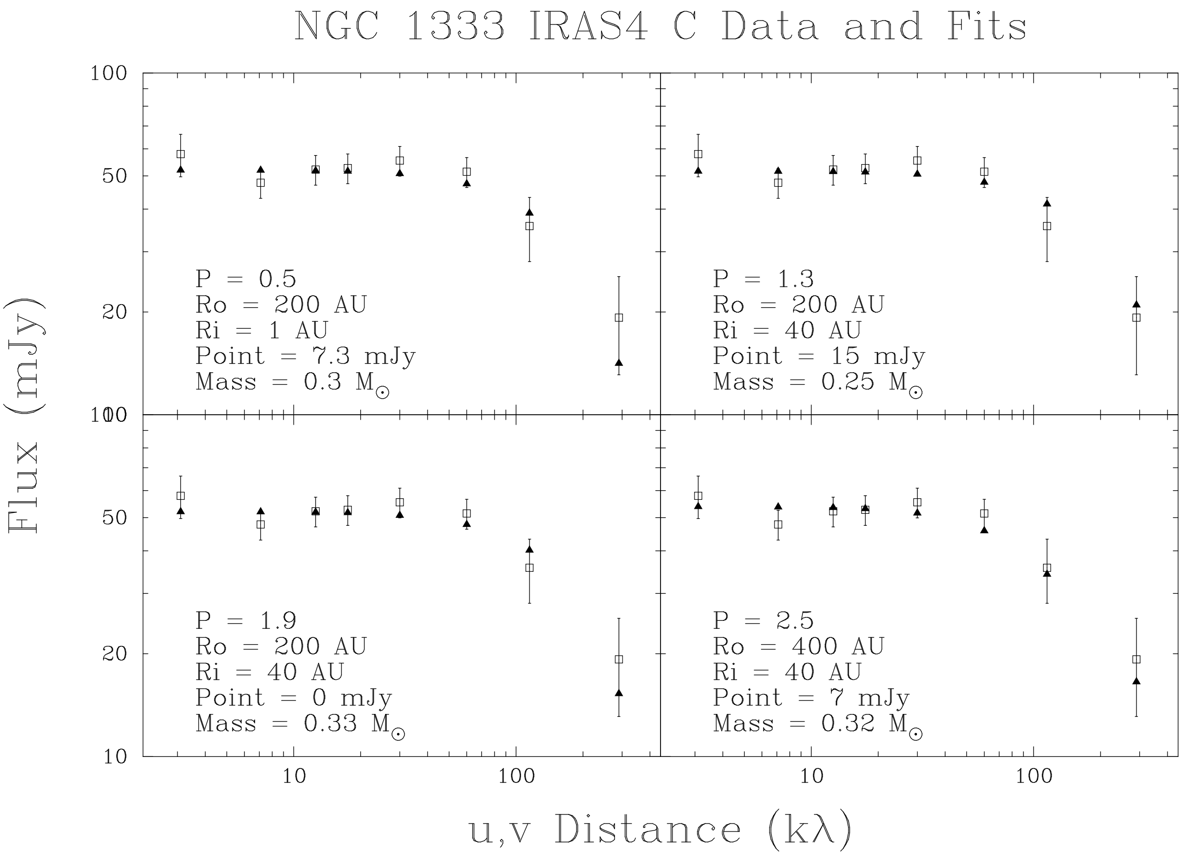

Fig. 5.9. The *u*,*v* data binned in annuli around NGC 1333 IRAS4 C and four fits to the data using a standard envelope model, $\rho \propto (\frac{r}{1AU})^{-p}$ and T(r) = $T_o(\frac{r}{1AU})^{-0.4}$ where T_o = 252 K, plus a point source.

The binned data in Figure 5.7 have a well defined slope of -0.3 (corresponding to p ~2.3 for an infinite envelope) in the 3 kλ to 35 kλ region and a slope of -0.7 (corresponding to p ~1.9 for an infinite envelope) in the 22 kλ to 125 kλ region. The acceptable model parameters are in Table 5.5; the majority of the models are in either the p = 2.3 or p = 2.5 family of models. As shown in Figure 5.7, p = 2.3 is the best fitting model, following the slope of the *u,v* data very closely. The p = 2.5 family has more numerous acceptable models, but in general the p = 2.5 models are not steep enough from 8 kλ to 100 kλ; the inner *u,v* spacings are underestimated and the moderate *u,v* spacings are overestimated. At the lower end of the acceptable models, the p = 1.9 model requires small outer radii to match the inner *u,v* spacing slope, thus the model is probably not realistic. In addition, the slope of the p = 1.9 models is not steep enough in the 10 kλ to 30 kλ range. The p = 2.1 models exhibit the general trend of the *u,v* data, but typically require a small radius to fit the inner *u,v* points. Point source fluxes from 22 to 55 mJy are generally required.

In Figure 5.8, the *u,v* data are shown for NGC 1333 IRAS 4 B, after subtraction of sources A and C from the *u,v* data. The innermost *u,v* data point was not excessively high, so it was used as a model constraint. The data has a well defined slope of -0.2 in the 5 kλ to 90 kλ range (corresponding to p ~2.4 for an infinite envelope). Unlike the data from IRAS 4 A, the slope in the outer *u,v* spacings is particularly steep. As shown in Table 5.6, there are a large range of acceptable models for NGC 1333 IRAS 4 B. The best models are the p = 2.7 and p = 2.9 families, which are easily modeled with $\chi^2 \ll 1.0$ for a wide range in the other parameters. The lower range of acceptable density power-law models (p = 1.9 to p = 2.3) have difficulty fitting the slope of both the intermediate *u,v* spacings and the outer *u,v* spacings.

In Figure 5.9, the *u,v* data are shown for NGC 1333 IRAS 4 C, after subtraction of sources A and B from the *u,v* data. Again, the innermost *u,v* data point was not excessively high, so it was used as a model constraint. As stated in Paper I, the source is mostly compact with nearly constant *u,v* amplitude from 2 kλ to 80 kλ. The source becomes resolved for *u,v* distances longer than 80 kλ, but there are not enough data in this region to constrain the density power-law (with the outer radius as a free parameter, any model density power-law can fit the data).

5.4.5 VLA 1623

VLA 1623 is the prototype Class 0 source (Andrè, Ward-Thompson, & Barsony 1993). Located near the center of the ρ Ophiuchi A star forming region, VLA 1623 drives a large outflow with a principal axis of ∼-60° (Andrè et al. 1990; Dent et al. 1995; Yu & Chernin 1997). The high resolution $\lambda = 2.7$ mm observations (Figure 15 Paper I), suggest that the system is actually a binary system with a separation of $1\farcs1$. Recent high resolution observations at $\lambda = 3.6$ cm show two sources that align with the two $\lambda = 2.7$ mm sources (Bontemps & Andrè 1997), to within uncertainties. Although the $\lambda = 3.6$ cm sources were interpreted as knots of a radio jet that drives the CO outflow, Paper I argues that VLA 1623 is a close binary system with two distinct circumstellar structures.

In Figure 5.10, the *u,v* data are shown for VLA 1623. The *u,v* data were binned around the center of the system, between the two point sources. The first three *u,v* spacing data points are amplitude biased by large scale emission from the nearby regions of SMM1 and SMM2 (Ward-Thompson et al. 1989; Andrè, Ward-Thompson, & Barsony 1993). This structure, seen in the lowest resolution image of Figure 4.15, is a north-south continuum ridge that contains a number of submillimeter sources. From 7 kλ to 25 kλ, the circumbinary envelope structure dominates the *u,v* data, with a shallow slope of -0.15 (corresponding to p ~2.45 for an infinite envelope) At *u,v* spacings greater than 30 kλ, the two circumstellar regions beat against each other, making it difficult to estimate the density power-laws.

We attempted to fit the *u,v* data with two point sources of flux equal to the peak flux in Figure 15 of Paper I. However, this model overestimated the flux in the outer *u,v* spacings. A correct model requires two circumstellar disks (or point sources) embedded within two circumstellar envelopes, and perhaps a larger circumbinary envelope. Since this type of model has too many free parameters to be constrained by the current data; thus, VLA 1623 was not modeled.

5.4.6 IRAS 16293-2422

IRAS 16293-2422 is one of the most studied young stellar objects in the ρ Ophiuchi star forming region. The system is a deeply embedded binary with two molecular outflows (Walker et al. 1986; Wootten 1989; Mundy et al. 1992). The southern source A, drives a large molecular outflow with a principal axis of ~50°. The northern source B has an associated outflow with a principal axis of ~75°, but the outflow does not extend down near the source, which may indicate that the source no longer drives the outflow (Walker, Carlstrom, & Bieging 1993). In high resolution observations at $\lambda = 2$ cm, source A has two peaks, A1 and A2 (Wootten 1989). In the $\lambda = 2.7$ mm high resolution image (Figure 16 Paper I), source A and B are clearly detected. Source A, the most extended object in the survey, appears slightly elongated along the position angle of the $\lambda = 2$ cm sources. The two sources, which may have individual circumstellar envelopes and disks, are embedded within a circumbinary envelope.

In Figure 5.11, the *u,v* data are shown for IRAS 16293-2422. The *u,v* data

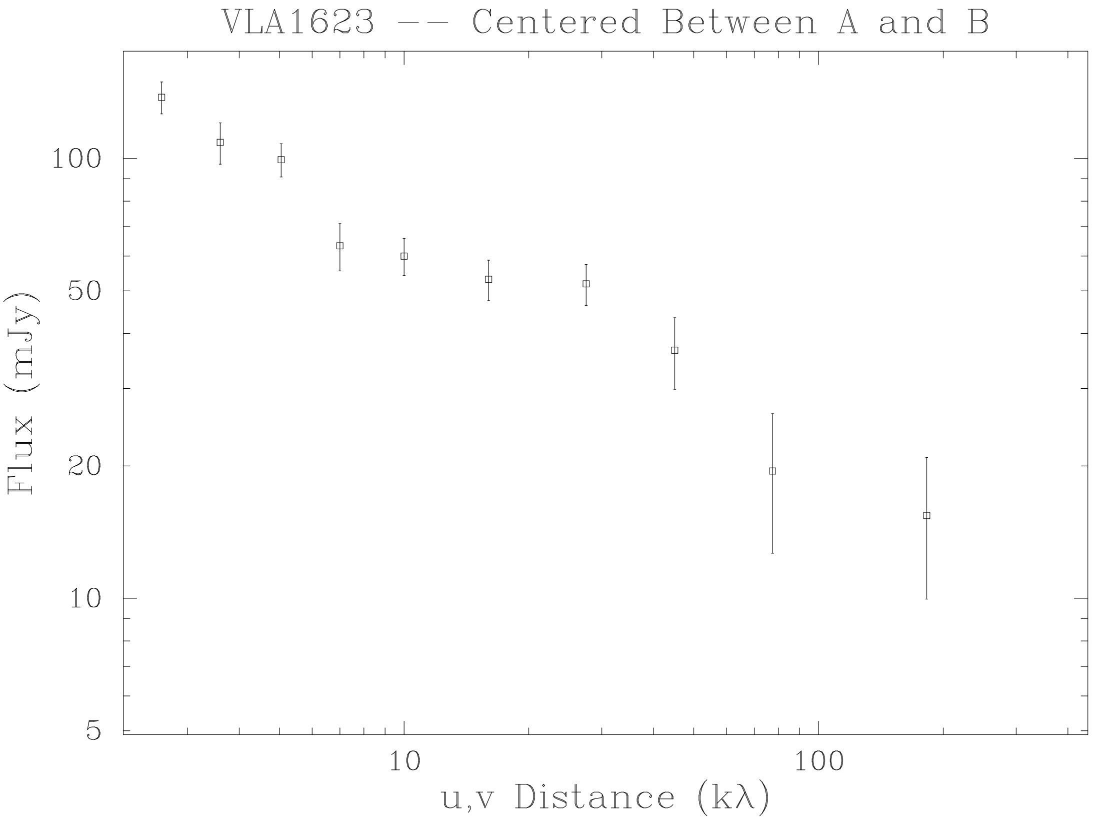

Fig. 5.10. The *u,v* data binned in annuli between sources A and B of VLA 1623.

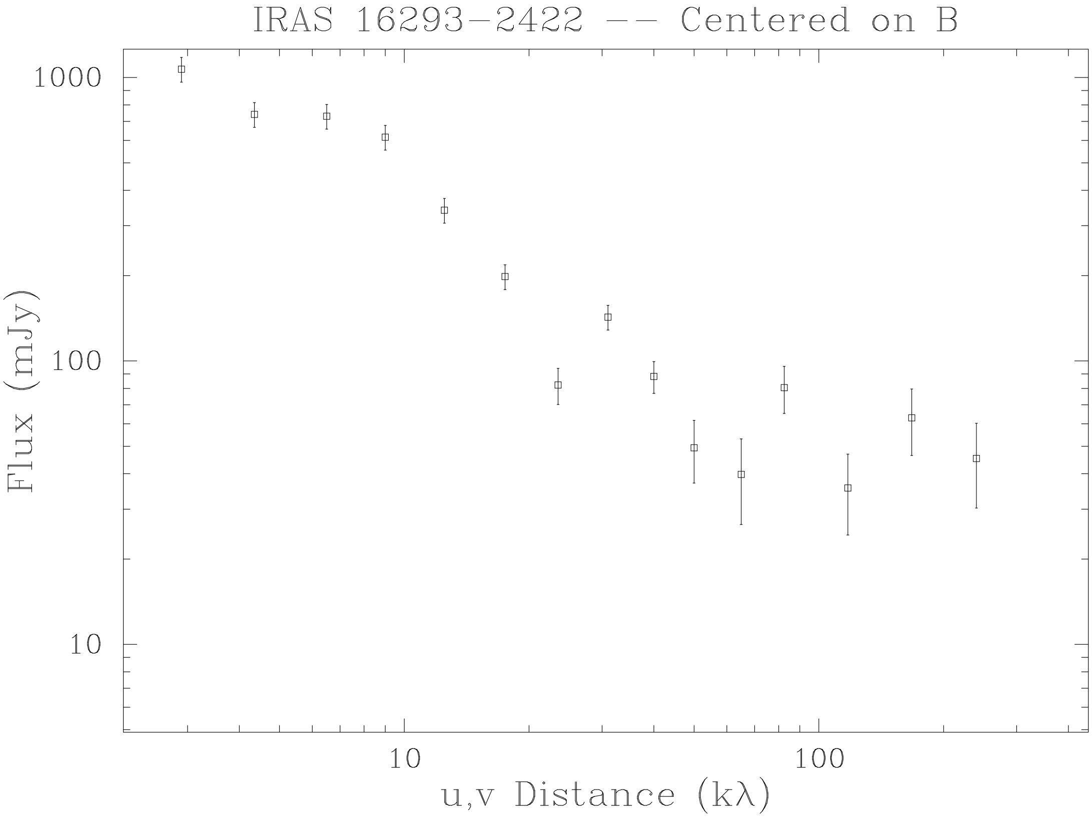

Fig. 5.11. The *u,v* data binned in annuli around source B of IRAS 16293-2422.

were binned around source B, since source A was known to be very extended. Like NGC 1333 IRAS 4 A, the first *u,v* data point is biased high, due to a large scale structure. There is a very steep slope of -1.7 from 8 kλ to 20 kλ, which indicates a small p+q value. For the *u,v* values greater than 20 kλ, the beating effect of the two sources dominates the curve. We attempted to fit the *u,v* data with two point sources of flux equal to the peak flux in Figure 16 of Paper I. As in the case of VLA 1623, this model overestimated the flux in the outer *u,v* spacings. A more complicated model is required, but these data would not constrain the model; thus, IRAS 16293-242 was not modeled further.

5.5 Conclusion of the Standard Envelope Model

By utilizing the standard power-law envelope model, we have been able to place constraints upon the conditions in the early stages of star formation. However, the strength of our constraints are limited by significant cross-correlations between model parameters. There are three specific aspects of the modeling that are worth noting.

(1) One of the primary strengths of this study is the ability of the interferometer to separate large scale emission from compact emission, allowing us to probe for a circumstellar disk component embedded within a circumstellar envelope. As the results show, all systems have acceptable models with no central point source, but, typically, point source flux values in the range of 5 to 40 mJy are found for the best fits. We can make a mass estimate for the embedded disk using the circumstellar disk of HL Tauri as a standard. A HL Tauri type disk (disk mass $\sim$ 0.07 M$_\odot$; §4.5 or §5.10.1) has a flux of $\sim$ 100 mJy at the distance of Taurus (140 pc). If placed at the distance of Perseus (350 pc), the flux of HL Tauri would be 16 mJy. So the range of acceptable point source fluxes would

represent circumstellar disk masses of 0.02 to 0.2 $M_\odot$. This is a small fraction of the circumstellar envelope mass, typically ~ 1 $M_\odot$. However, the addition of the point source is linked to the slope in the *u,v* diagram, and it is difficult to separate completely the effects of a central point source, the inner and outer radii, and the density power-law. Our data, solidly show that most of the emission, typically 90% or more, arises from the circumstellar envelope, but the data can not quantitatively constrain the disk contribution.

(2) For the majority of the good fits, the inner and outer radii are not well constrained. This is due to a combination of steep power-law indices and weak sensitivity to large-scale structures in the interferometric data. In most of the modeled systems, the density power-law index is steep, and the outer edge of the envelope is not well defined. The models that do constrain the outer radius typically require a small envelope to mimic the slope in the inner *u,v* plane. Despite these uncertainties, the majority of the good fits have total system masses (envelope plus disk) within 15% of each other for a given source. The interferometer sensitivity to large scale structure is limited by the shortest *u,v* spacings. The data has sensitivity to structures as large as $\sim 50''$, which is equivalent to a radius of 8500 AU at Perseus.

(3) The most important result from this modeling is the effect of the density power-law index on the fits. All of the theoretical models and numerical studies (which range from simple isothermal spheres to complicated magnetic and rotation models) predict power-law indices less than or equal to 2.0 (Larson 1969; Penston 1969; Hunter 1977; Shu 1977; Whitworth & Summers 1985; Mouschovias, Paleologu, & Fiedler 1985; Fiedler & Mouschovias 1993; Basu & Mouschovias 1994,1995; Safier, McKee, & Stahler 1997). Half of the envelope models (NGC 1333 IRAS 2 A, SVS 13 A, and SVS 13 B) are generally fit with density power-law indices between p = 1.5 to 2.1, but the other half

Table 5.7. Model Summary of Characteristic Best Fits

Source	p-index (range)	Most Likely Parameters p-index	M_{env} ($M_{\odot}$)	S_{ps} mJy	M_{disk} ($M_{\odot}$)
L1448 IRS3 B	2.1 - 2.7	2.5	1.77	5	0.02
NGC 1333 IRAS2 A	0.5 - 2.3	1.9	0.63	7	0.03
SVS 13 A	0.5 - 2.1	0.9	0.60	12	0.06
SVS 13 B	1.3 - 2.1	1.9	1.12	16	0.07
NGC 1333 IRAS4 A	1.9 - 2.5	2.3	3.34	33	0.15
NGC 1333 IRAS4 B	1.9 - 2.9	2.7	1.87	20	0.09

(L1448 IRS3 B, NGC 1333 IRAS 4 A and B) require p = 2.1 to 2.7 (see Table 5.7). Are the the steep power-law indices truly correct? To address this question, we examine the morphology of the fits, the temperature profile assumption, and the possibility of more complicated models.

5.5.1 The Morphology of Steep Density Models in the *u,v* Plane

For the three objects with steep density profile models, Figures 5.1, 5.7, and 5.8, the inner *u,v* spacing data is very flat, which demands a steep density profile to fit the slope. In the 10-200 kλ region, the visibilities transition into a steeper slope in the *u,v* plane, which is indicative of a shallow density profile on the sky. This is in contrast to the infinite envelope visibility slope discussed in §2.5.1; the expected slope in the *u,v* plane for an infinite extent envelope remains constant for all *u,v* spacings. However, with a real envelope, the steep density profiles can diverge from the expected slope in the *u,v* plane through a combination of inner radius cutoff, outer radius, and large optical depth. So, the steep density profiles have portions of parameter space which allow them to fit the general trends of the data.

5.5.2 Temperature Profile Assumption

Systematically, the models that require steep density profiles also have the most massive envelopes (see Table 5.7); "best fit" envelope masses are larger than 1.5 $M_\odot$. Our standard model utilized the simple temperature power-law $T \propto r^{-0.4}$, but this assumption is only valid for an optically thin envelope. When the envelope becomes optically thick to the stellar radiation field, the dust grains at inner radii receive additional heating from dust-generated infrared radiation, allowing the temperature to increase. The resulting temperature profile has a steep falloff over the inner radii, then asymptotically approach $T \propto r^{-0.4}$ in the outer radii. How much of an effect does a massive envelope have on the assumed temperature profile, and how does this affect the inner *u,v* region slope?

5.5.3 A Self-Consistent Radiative Transfer Model

In order to investigate the temperature profile in the simple envelope model, we performed calculations with the self-consistent dust radiative transfer code of Wolfire & Cassinelli (1986; WC hereafter). The WC code assumes a central heating source that is embedded within a spherical dust envelope. The central source is characterized by a stellar luminosity (L_*) and an effective temperature (T_*). The dust envelope is specified by an outer radius, the power-law density index, the density at the outer radius, and the destruction temperature of the dust, which specifies the inner radius. Given these parameters, the WC code self-consistently calculates the dust temperature profile by conserving the luminosity at all radii.

For the star's effective temperature, we used 10000 K, which is the temperature derived for T Tauri stars to explain the veiling continuum (Hartigan, Edwards, & Ghandour 1995). The WC code uses a MRN (Mathis, Rumpl, & Nordsieck 1977) dust grain distribution ("bare" graphite plus silicate grain distribution) and the Draine & Lee (1984) optical constants to describe grain properties. We modified the long wavelength characteristics of this model ($\lambda > 100\ \mu$m) to match the λ^{-1} wavelength dependence of the emissivity generally seen in circumstellar environments (see Figure 5.12; Beckwith and Sargent 1991; Beckwith et al. 1990; Weintraub et al. 1989). This hybrid model preserves the optical and infrared properties of the MRN dust grain model, while forcing the long wavelength behavior to be consistent with our simple models ($\kappa_\nu(110GHz) = 0.009\ cm^2g^{-1}$).

Figures 5.13 thru 5.16 present plots of the temperature profile for various values of the density power-law index p, envelope mass, inner radius cutoff, and luminosity, respectively. Figure 5.13 shows the temperature profile for a 1 $M_\odot$, 5000 AU radius, and 10 $L_\odot$ envelope with various density power-law indices. The line at the bottom of the figure has a -0.4 slope. As the power-law index is increased, the opacity increases, and the dust becomes self-shielding; the interior material can not radiate away its luminosity into the outer envelope, and the temperature rises. At outer radii, the slope always approaches -0.4. Figure 5.14 shows the effect of changing the envelope mass for a fixed luminosity of 10 $L_\odot$, a 5000 AU radius, and a fixed density power-law index of p = 2.0. As expected, the increase of mass places more material into the interior. This results in more self-shielding and the temperature increases. At inner radii, the temperature difference can be as much as a factor of two. Again, beyond 100 AU all of the temperature profiles tend toward the optically thin $T \propto r^{-0.4}$. Figure 5.15 demonstrates that the inner radius cutoff has a negligible effect on the temperature profile out beyond $\sim$ 40 AU, and Figure 5.16, shows the effect of increasing luminosity for fixed envelope properties; the temperature profiles approximately scale as $(\frac{L}{L_\odot})^{0.25}$ as found by Wilner, Welch, & Forster (1995).

The WC code shows that the optically thin temperature assumption is incorrect for envelope masses > 0.1 $M_\odot$ and density profiles steeper than p = 1; however, the largest changes occur at small radii (< 100 AU or $0\farcs3$ at the distance of Perseus) where our observations are not that sensitive. How does this corrected temperature profile manifest itself in the *u,v* plane? The temperature power-law index increases in the inner radii but converges to 0.4 in the outer radii; so p+q will be larger at inner radii and unaltered at outer radii. In the *u,v*

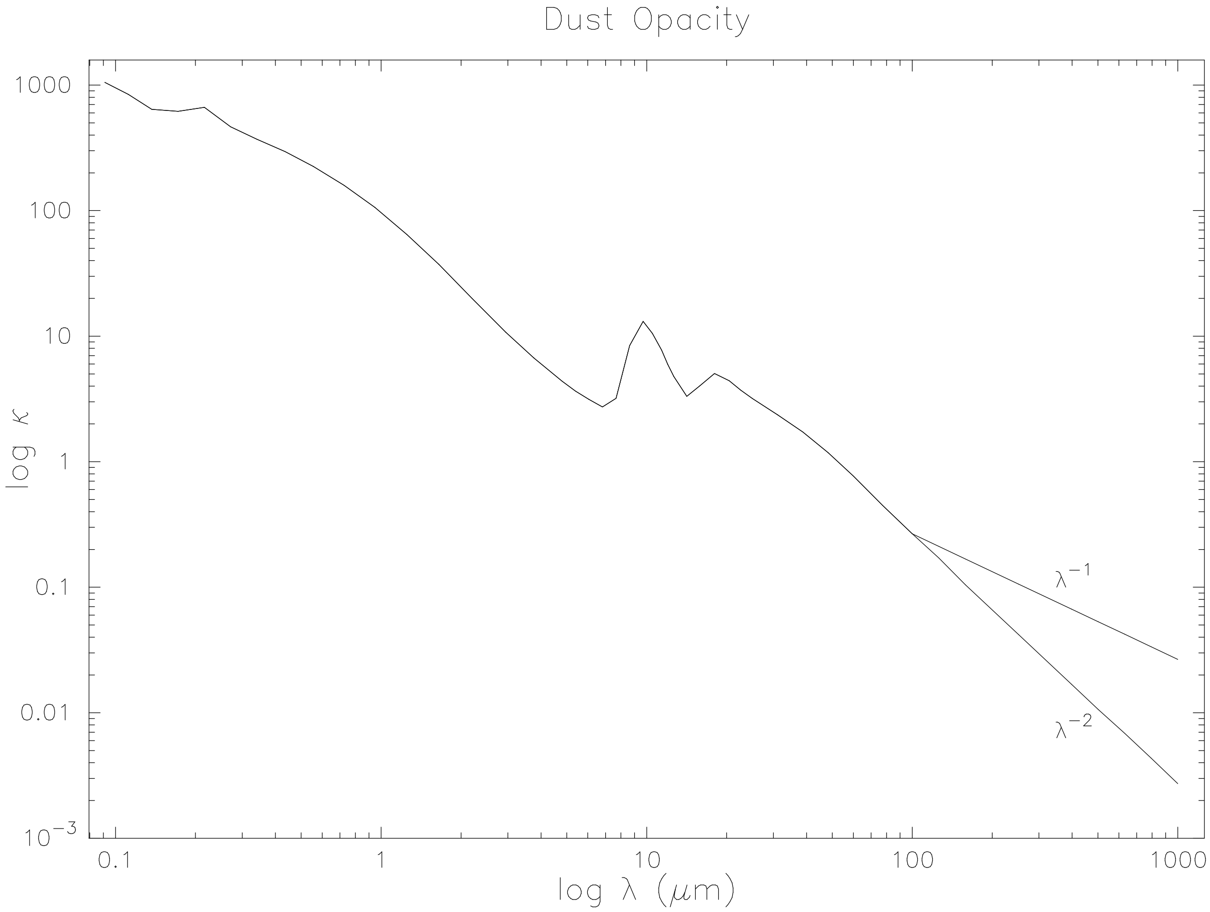

Fig. 5.12. The dust opacity function used in the WC code calculation. The λ^{-2} is the original MRN dust opacity function and the λ^{-1} profile is the long wavelength modified dust opacity function more appropriate for young stellar systems.

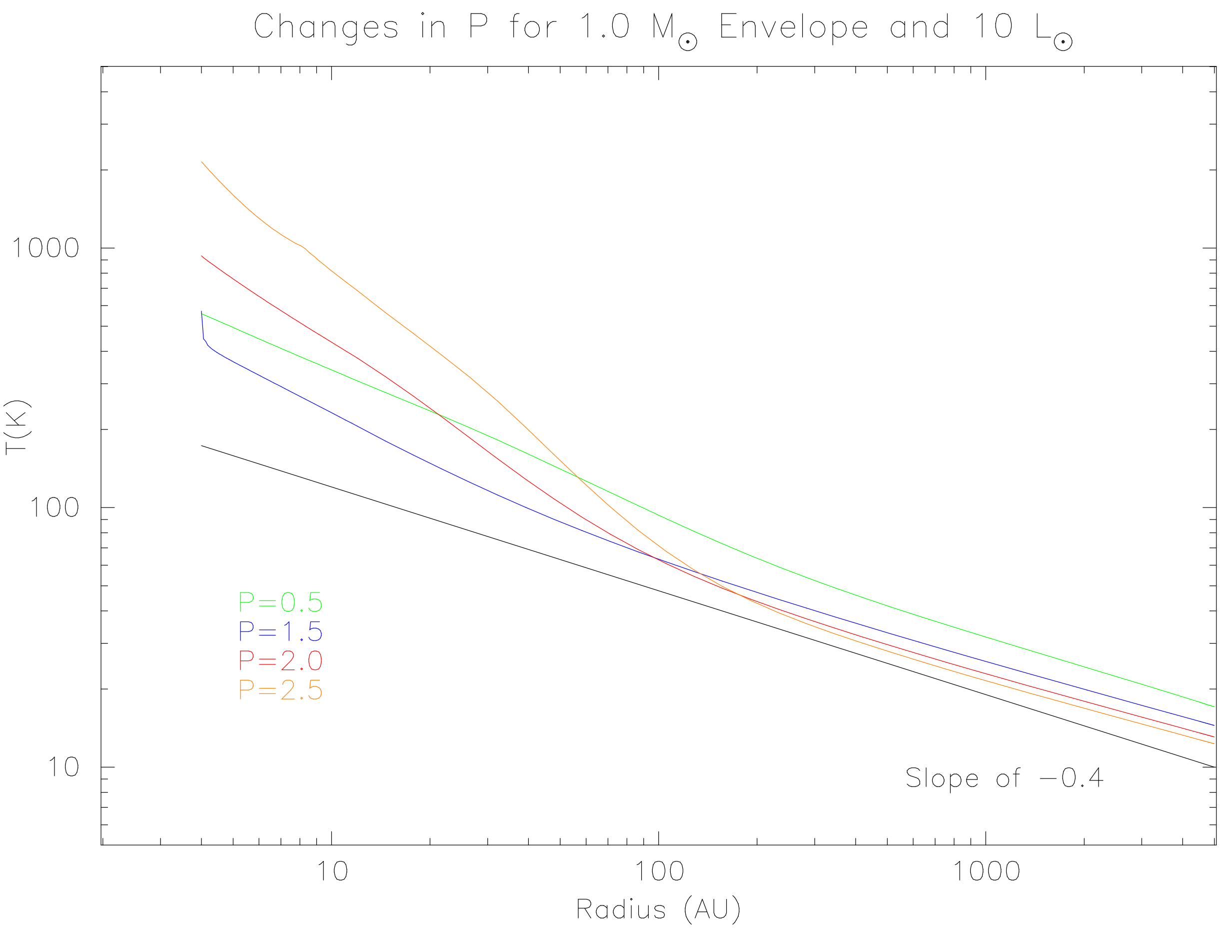

Fig. 5.13. Variations in the temperature profile due to changes in the density power-law index (p) of a 1 M$_\odot$, 5000 AU radius envelope with a luminosity of 10 L$_\odot$ using the self-consistent radiative transfer code of Wolfire & Cassinelli (1986).

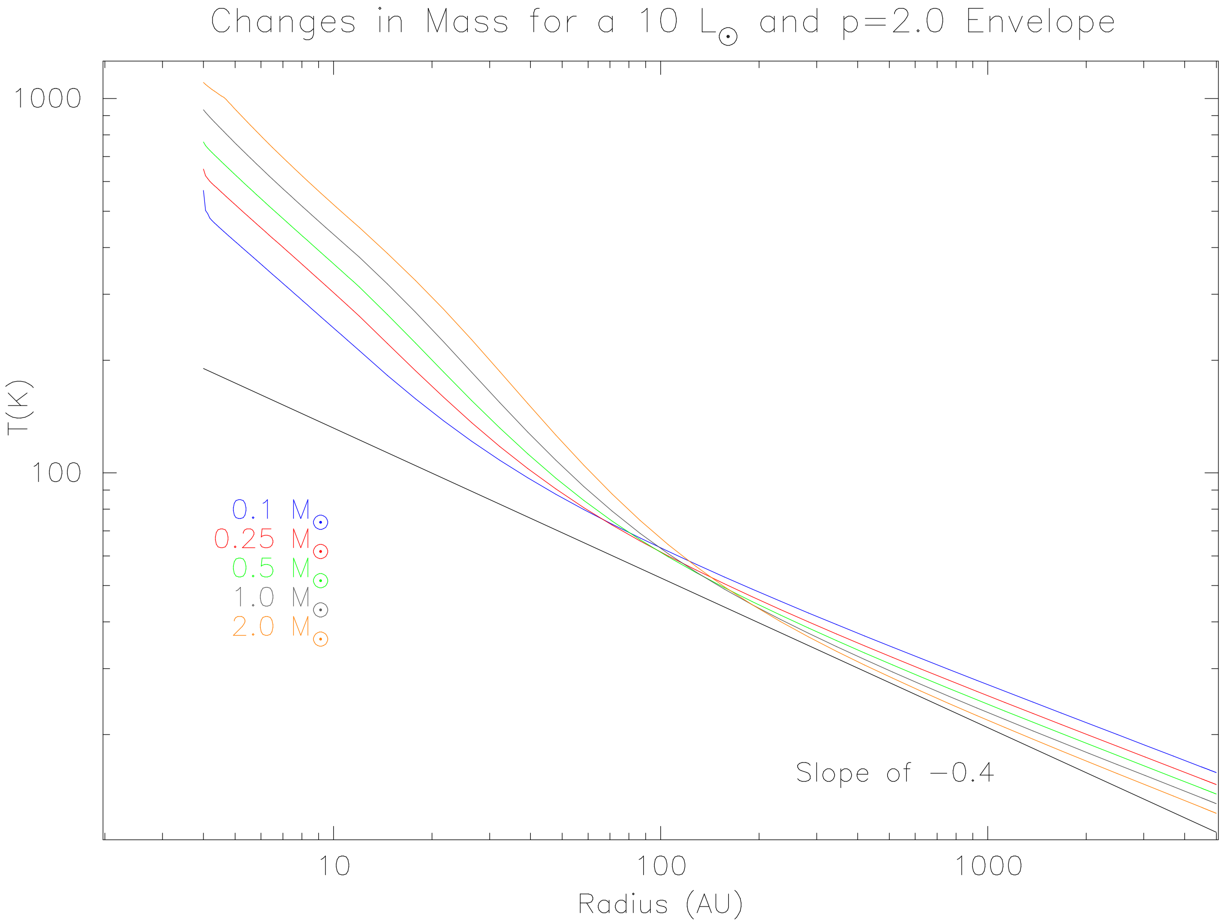

Fig. 5.14. Variations in the temperature profile due to changes in mass for an envelope with a density power-law index of 2.0, a radius of 5000 AU, and a luminosity of 10 $L_\odot$ using the self-consistent radiative transfer code of Wolfire & Cassinelli (1986).

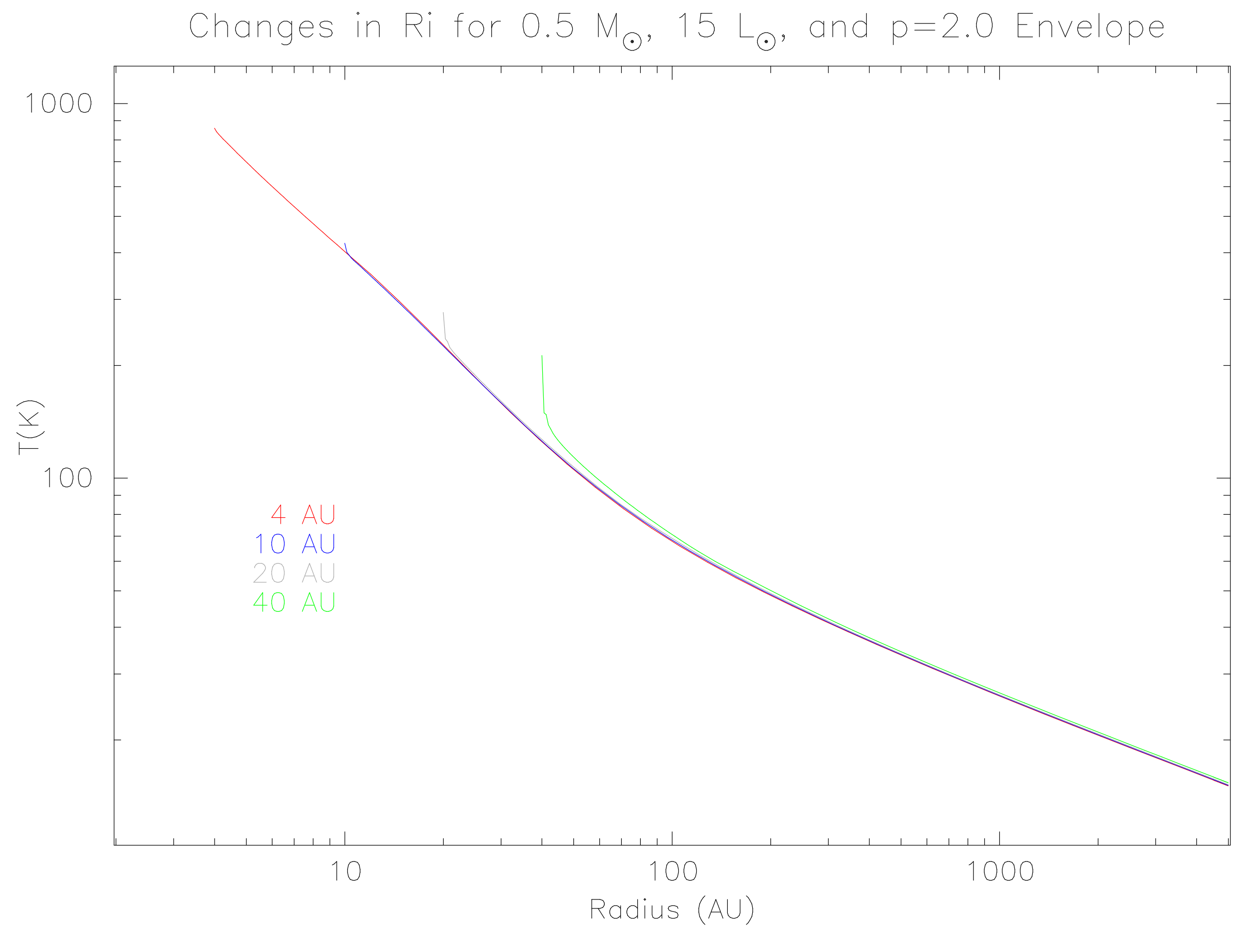

Fig. 5.15. Variations in the temperature profile due to changes in the inner radius cutoffs for an envelope of 0.5 $M_\odot$, a density power-law index of 2.0, an outer radius of 5000 AU, and a luminosity of 10 $L_\odot$ using the self-consistent radiative transfer code of Wolfire & Cassinelli (1986).

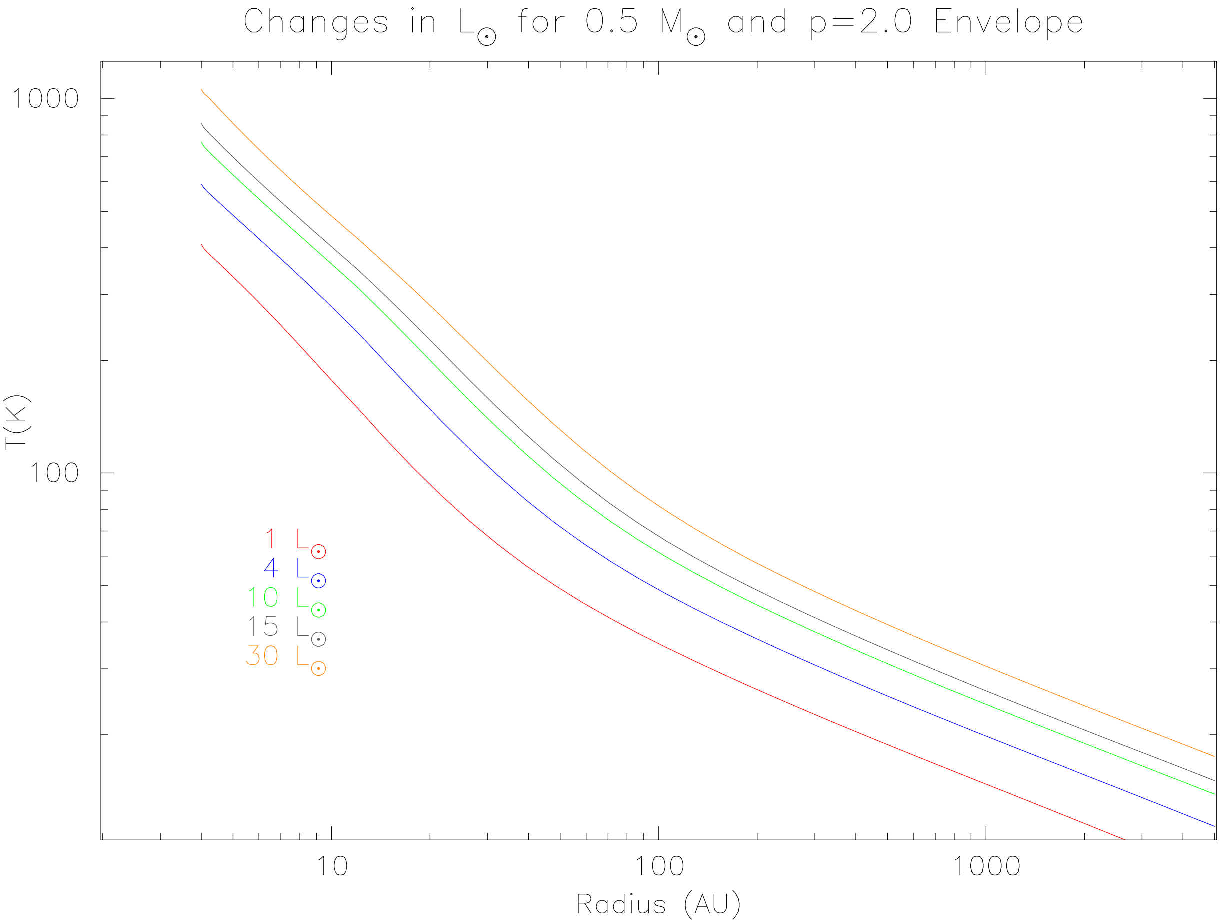

Fig. 5.16. Variations in the temperature profile due to changes in the luminosity for an envelope of 0.5 $M_{\odot}$, a density power-law index of 2.0, and an outer radius of 5000 AU.

plane, this corresponds to an unchanged slope at small u,v spacings (the outer radii) and a shallower slope at larger u,v spacings (the inner radii). This correction is in the opposite sense of the change in slope in the visibility data of Figures 5.1, 5.7, and 5.8.

We incorporated the temperature profile from the WC code into our power-law envelope models. In this case, we explored a grid of parameter space including: p from 1.0 to 2.0 in steps of 0.2, R_o from 1000 AU to 10000 AU in steps of 1000 AU, central point source flux in the same steps as before, and the inner radius, R_i was set to 5 AU.

Figure 5.17 presents the best fit models with a power-law density and a self-consistent temperature profile for the three massive envelopes and SVS13 A, one of the lower mass envelope models. For SVS 13 A, the p = 1.6 model is nearly identical to the p = 1.7 fit with the $T \propto r^{-0.4}$ assumption in Figure 5.5. Although p = 0.9 is listed as the best fit in Table 5.7, the p = 1.7 is statistically indistinguishable. IRAS 4 A, the most massive modeled envelope, has the most impressive difference. With the self-consistent temperature model, it is well fit by a p = 1.8 density profile. With the $T \propto r^{-0.4}$ assumption, the envelope could only be fit reasonably with p > 2.1. Since this source is the most massive, we do expect the self-consistent temperature profile to have the most affect. In the other two cases, they are better fit by the self-consistent models than the $T \propto r^{-0.4}$ assumption for p < 2.0 (the χ^2 measure is significantly reduced), but the models still require unlikely small radii; thus, the preferred solutions still have steep density profiles.

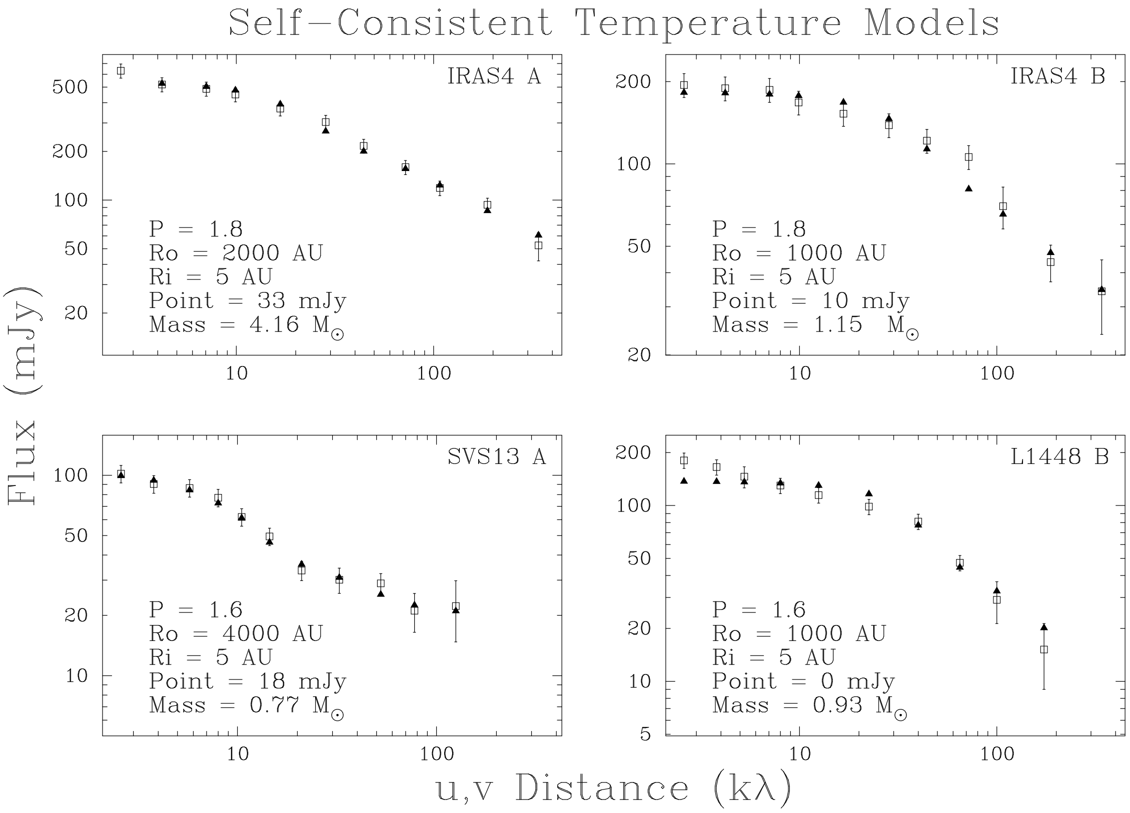

Fig. 5.17. Best fit simple power-law envelope models for NGC 1333 IRAS 4 A, NGC 1333 IRAS 4 B, L1448 IRS3 B, and SVS 13 A, utilizing the self-consistent radiative transfer code of Wolfire & Cassinelli (1986).

5.5.4 Envelope Conclusions and Questions

For the most massive source, NGC 1333 IRAS4 A, the self-consistent temperature model fits the data very well with $p < 2.0$. For NGC 1333 IRAS4 B and L1448 IRS3 B, the self-consistent temperature model lowers the χ^2 for the shallower density power-law indices, but they require small envelopes to mimic the shallow slope in the short *u,v* spacings. What other effects could be responsible for a steep power-law index?

We adopted a constant dust opacity with radius in our models. However, dust properties can change with environment (e.g. Gehrz 1989; Weintraub, Sandell, & Duncan 1989; Henning, Michel, & Stognienko 1995). As Figure 5.12 illustrates, the dust opacity in the interstellar medium is better described by a λ^{-2} power-law at long wavelengths, but in star forming regions the dust opacity is best described by a λ^{-1} power-law (Hildebrand 1983; Beckwith and Sargent 1991; Chini et al. 1991; Zinnecker et al. 1992). There are several grain alterations that may explain the increased dust opacity in circumstellar regions, such as chemical evolution (Begemann et al. 1994; van Dishoeck & Blake 1988), formation of dirty ice mantles (Draine 1985; Henning, Chini, & Pfau 1991; Preibisch et al. 1993), altering of the grain geometry (long "needle-like" grains; Wright 1982), or grain coagulation into fluffy grains (Wright 1987; Jones 1988; Bazell & Dwek 1990; Ossenkopf 1991; Stognienko, Henning, & Ossenkopf 1995). In any of these scenarios, we might expect the dust opacity in the circumstellar region to become a function of radius: the outer regions could have grain properties similar to the interstellar medium while the inner, denser portion of the envelope is likely to have the most processed grains due to the short timescales for grain alteration. Since this timescale depends on the density, the dust opacity could have a power-law dependence on radius. In the standard power-law envelope model, the emission is dependent on the optical depth,

$$d\tau \;=\; \kappa_\nu \; \rho(r) \; dl.$$

With grain alteration, the optical depth becomes the product of power-laws in density and dust opacity,

$$d\tau \;=\; \kappa_0\left(\frac{\nu}{\nu_o}\right)^{-\beta}\left(\frac{r}{r_o}\right)^{-s}\rho_o\left(\frac{r}{r_o}\right)^{-p} dl.$$

Thus, a radial dependency in the dust opacity could be indistinguishable from that in density and erroneously produce steeper density power-law indices in the simple model fits.

Another possible explanation for the steeper density profiles is non-spherical or more complicated geometries. All of the embedded systems are known to be driving large molecular outflows that are evacuating material out of the envelope. These cavities could have a significant effect on the slope in the *u,v* plane, especially for a steep density profile. In addition, the sources may have complicated geometry with large scale structures intertwined with smaller structures. For example, the fit of L1448 IRS3 B in Figure 5.17, follows the data in the outer *u,v* regions, but underestimates the *u,v* data in the inner *u,v* plane. The L1448 IRS3 system is in a very confusing star forming region with many young stellar systems, suggesting the presence of larger structure that may contaminate the flux at the inner *u,v* spacings.

In summary, we have shown that all of the envelope models are well fit by the standard power-law model, but that for the more massive envelopes, the density profile power-law indices are larger than expected by star formation theory. When a self-consistent temperature profile is used, the lower mass envelope fits are unchanged, and the higher mass envelopes have better fits with $p < 2.0$. With these models, we can place some of the first constraints on the emission contributions from the envelope and disk, respectively.

5.6 Introduction to Modeling of Disks

Young optical stellar systems commonly exhibit excess infrared and millimeter continuum emission when compared to similar main sequence stars (Mendoza 1966). This excess emission is commonly explained as arising from circumstellar disks that surround the young stars (Mendoza 1968; Lynden-Bell & Pringle 1974; Harvey, Thronson, & Gatley 1979; Cohen & Kuhi 1979; Cohen 1983; Adams, Lada, & Shu 1987; Bertout, Basri, & Bouvier 1988). Theoretical models predict circumstellar disk radii that range in size from tens of AU to a few hundred AU (Ruden & Lin 1986; Lin & Pringle 1990; Ruden & Pollack 1991; Shu et al. 1993; Yorke, Bodenhemer, & Laughlin 1993; Stahler et al. 1994). These size scales, on the order of one arcsecond or less for the nearest star forming regions, place strong instrumental demands on observations.

Imaging the disks is best done at wavelengths beyond 10 μm because the majority of the mass is in the outer regions of the disk, which are at temperatures below 100 K. Only recently has sub-arcsecond resolution observations been available with instruments at millimeter and submillimeter wavelengths. The circumstellar disk of HL Tauri, the brightest millimeter source in the $\lambda = 1.3$ mm survey of Beckwith et al. (1990), was first resolved by the CSO-JCMT single baseline interferometer (Lay et al. 1994), and shortly thereafter imaged by the BIMA interferometer at $\lambda = 2.7$ mm (Mundy et al. 1996) and the VLA interferometer at $\lambda = 7$ mm (Wilner, Ho, & Rodríguez 1996). In Paper I (Chapter 4), we presented high resolution images of four T Tauri type stellar systems. We have resolved the circumstellar disk in two systems, HL Tauri and DG Tauri, and the circumbinary disk in the GG Tauri system. Since these data have good signal-to-noise, we can model these systems in the *u,v* plane.

5.7 The Disk Fitting Procedure

As discussed in §2.4.2, a power-law radial dependence of a circumstellar disk in the image plane transforms to a power-law in *u,v* distance in the *u,v* plane. The slope of the power-law in a log-log plot of *u,v* distance versus amplitude is related to the sum of the density and temperature power-laws as long as the emission is optically thin and the disk has a face-on geometry,

$$B(r) \propto r^{-(p+q)} \quad \rightarrow \quad V(\beta) \propto \beta^{(p+q-2)},$$

where β is *u,v* distance (see §2.4). Since the circumstellar disks are of order one arcsecond, we expect a emission profile that is flat in the inner *u,v* plane, until around 100 kλ, then the power-law properties should become evident. However, as in the case for envelopes, the slope is cross-correlated with temperature profile, outer-radius, and especially geometry. Disks are intrinsically non-axisymmetric depending upon the inclination in the plane of the sky, which adds to the difficulty of determining the surface density power-law index directly from the slope in the *u,v* plane. Thus, while the simple power-law relation gives a good qualitative feel for the behavior in *u,v* space, a full numerical model is needed to fit realistic circumstellar disk data.

The standard model, as discussed in §1.7, has six parameters: power-law of the surface density (p), total mass of the circumstellar disk (M) which is needed to determine the surface density constant Σ_o, inner cutoff radius (R_i), outer cutoff radius (R_o), inclination angle (i), and the principal axis (γ) of the major-axis of the ellipse formed by the projection of an inclined disk onto the plane of the sky. Since the *u,v* distance versus amplitude figures are representations of the visibilities averaged in annuli around the source, we do not well constrain the position angle of the principal axis or the inclination; thus, we assume i and γ values from other observations.

For each source, we explore the grid of models including: p from 0.0 to 1.9 in steps of 0.25, R_i of 1 or 5 AU, and R_o from 40 to 200 AU in steps of 20 AU. (GG Tauri was gridded differently due to the unique nature of the emission from the circumbinary disk.) For each model, the disk emission is calculated as an image, and the model is multiplied by the BIMA primary beam. The model is then Fast Fourier Transformed (FFTed) and sampled with the same *u,v* spacings as the data. The data and model are then both vector averaged in *u,v* distance bins, and the amplitude for each bin is compared by calculating the reduced χ^2. For each model parameter p, R_o, and R_i grid point, χ^2 is minimized with respect to the disk mass. Since the majority of the model information is in the data at large *u,v* spacings, we have doubled the statistical weight of the outer *u,v* data points.

5.8 Disk Results

Figures 5.18 to 5.20 show the source data in log(*u,v* distance) versus log(amplitude) plots. For both the models and the data, the complex visibility quantities are vector averaged over annuli in the *u,v* plane, centered at the source positions given in Paper I. The error bars on the figures are the statistical error bars based on the standard deviation of the mean of the data points in the bin, with a minimum of 10%, reflecting the uncertainty in the overall calibration. In each figure, there are four models overlaid on the data to show how the best fit model changes with increasing surface density power-law, p. We only considered models with a reduced $\chi^2 \leq 1.5$ to be acceptable fits. Again, this corresponds to a 95% confidence level for the typical model.

5.8.1 HL Tauri

HL Tauri was the first circumstellar disk to be resolved and imaged (Lay et al. 1994; Mundy et al. 1996). Although HL Tauri was first classified as a visible T Tauri system, it has recently been shown to be a younger source, still embedded within a reflection nebula which was mistaken for the star (Stapelfeldt et al. 1995; Beckwith & Birk 1995; Weintraub, Krastner, & Whitney 1995; Close et al. 1997). HL Tauri has a large-scale ($\sim$ 2000 AU) envelope that has been detected in CO (Sargent & Beckwith 1991; Hayashi, Ohashi, & Miyama 1993). Paper I, Figure 4.4 (d) shows the new BIMA image, which clearly resolves the circumstellar disk with better signal-to-noise and higher resolution than the image of Mundy et al. (1996). The extension toward the north-east in Figure 4.4 (d) is along the axis of the optical jet (Mundt et al. 1990).

Recent work by Lay et al. (1997) has done extensive modeling in the *u,v* plane at λ = 650 μm and 870 μm from the CSO-JCMT single baseline interferometer and the Owens Valley Radio Observatory millimeter array at λ = 1.4 mm, with comparisons to observations at λ = 2.7 mm (Mundy et al. 1996) and λ = 7 mm (Wilner, Ho, & Rodríguez 1996). They found that the shorter wavelength data required steep surface density power-law indices, while the sizes measured by the longer wavelength data required shallow power-law index; they could not simultaneously fit the long and short wavelength data. In our modeling, we adopted the inclination and principal axis angles from the most likely values of Lay et al. (1996), 40° and 125°, respectively.

The *u,v* data are shown for HL Tauri in Figure 5.18. As expected from a small, circumstellar disk dominated emission structure on the sky, the *u,v* plot is unresolved until about $\sim$ 60 kλ. The slope beyond 60 kλ is -0.95 (corresponding to a p = 0.55 for an infinite power-law with q = 0.5). This data is well fit with

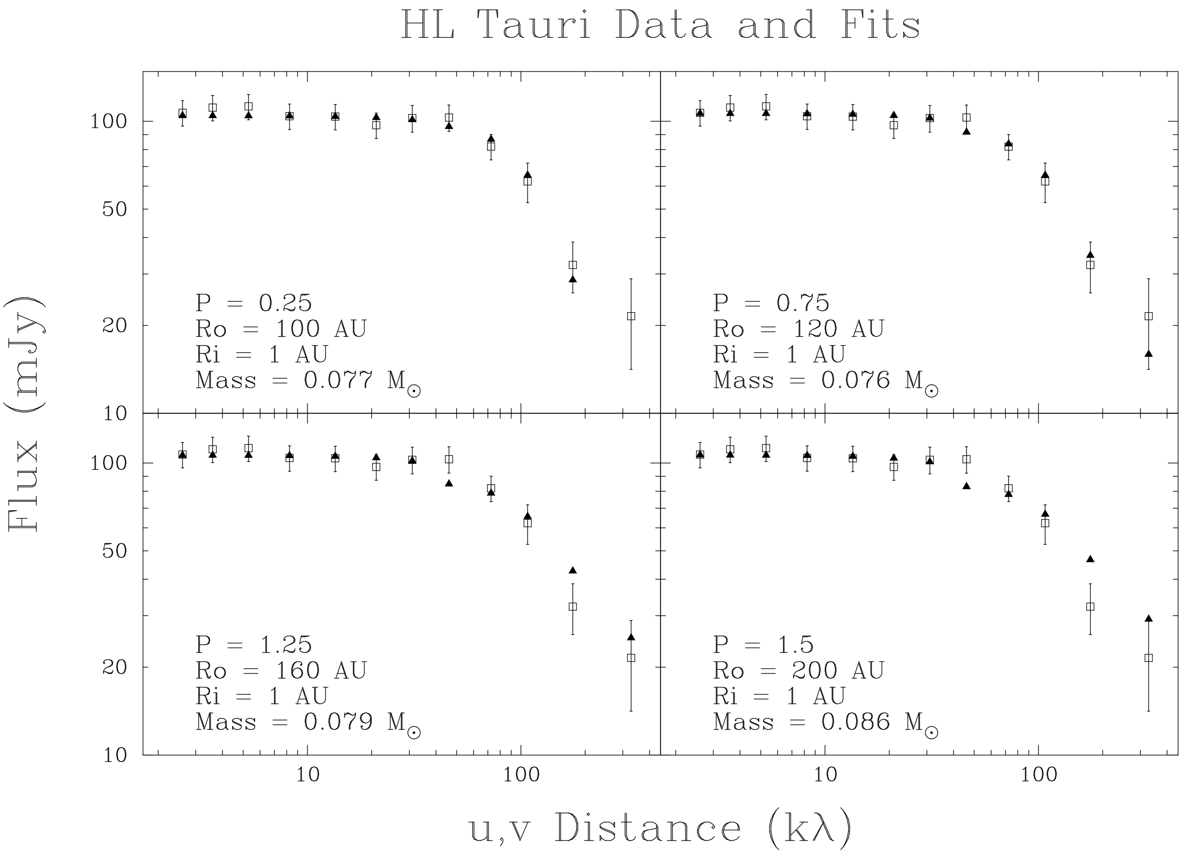

Fig. 5.18. The *u,v* data binned in annuli around HL Tauri and four fits to the data using a standard envelope model, $\Sigma \propto (\frac{r}{1AU})^{-p}$, $T(r) = 350(\frac{r}{1AU})^{-0.5}$ K, $i = 40°$, and $\gamma = 125°$.

Table 5.8. HL Tauri Fit Summary

p index	R_i (AU)	R_o (AU)
0.00	1,5	80,100
0.25	1,5	80,100,120
0.50	1,5	80,100,120,140
0.75	1,5	100,120,140,160
1.00	1,5	100,120,140,160,180
1.25	1,5	120,140,160,180,200
1.50	1,5	160,180,200

the standard model (see Table 5.8); the best model is the $p = 0.75$ family. There were not any acceptable fits for $p > 1.5$. As the power-law index is increased, the models require larger outer radii. The models are insensitive to small variations in inner radii. The mass derived are typically 0.07 to 0.09 $M_{\odot}$.

5.8.2 DG Tauri

The circumstellar disk of DG Tauri has been estimated to have a radius of 75 AU by modeling of DG Tauri's Spectral Energy Distribution (Adams, Emerson, & Fuller 1990). In addition, DG Tauri has been observed in the near infrared during a lunar occultation and with near-infrared speckle (Leinert et al. 1991). This study suggested two circumstellar structures to fit the data: an extended "shell" 6.8 AU in diameter and a larger scale "halo" 130 AU in diameter. In Paper I, Figure 4.1 (d) shows the BIMA image; the extension toward the southwest is along the axis of the optical jet (Kepner et al. 1993; Lavalley et al. 1997; Stapelfeldt et al. 1997). We adopt a principal axis of the disk which is perpendicular to the jet axis; this agrees with the derived principal axis from the Gaussian fit to the emission in Figure 4.1 (d), 165°. We use the derived inclination of 51° from Eislöffel (1992).

In Figure 5.19, the *u,v* data are shown for DG Tauri. The data show that DG Tauri has clearly been resolved by the observations. The slope beyond 100 $k\lambda$ is -0.75 (corresponding to a $p = 0.75$ for an infinite power-law). This data is well fit with the standard model (see Table 5.9) ; the best model is the $p = 1.5$ family, but all surface density power-law index values have acceptable fits. The models are insensitive to inner radii and to the outer radii for $p > 1.0$. The disk mass derived is typically in the range of 0.04 to 0.06 $M_{\odot}$.

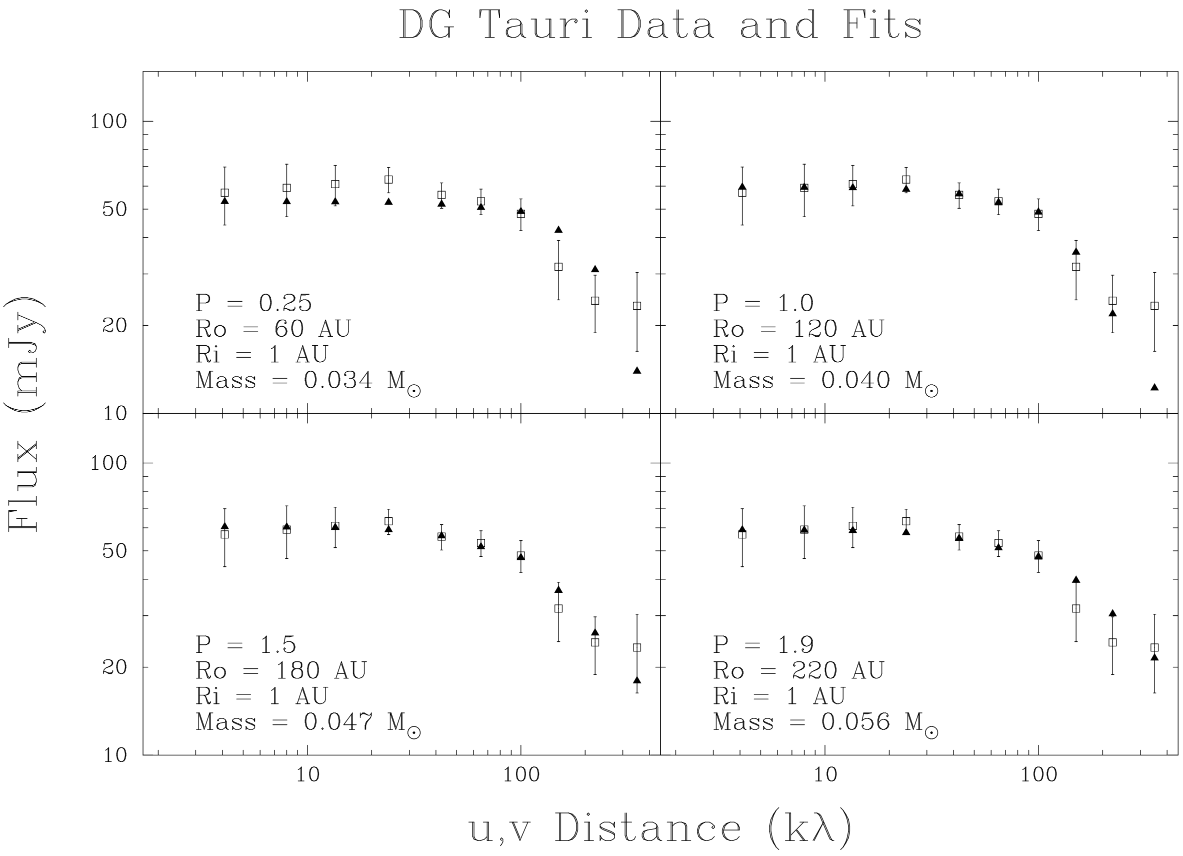

Fig. 5.19. The *u,v* data binned in annuli around DG Tauri and four fits to the data using a standard envelope model, $\Sigma \propto (\frac{r}{1AU})^{-p}$, $T(r) = 350(\frac{r}{1AU})^{-0.5}$ K, $i = 51°$, and $\gamma = 165°$.

Table 5.9. DG Tauri Fit Summary

p index	R_i (AU)	R_o (AU)
0.00	1,5	60
0.25	1,5	60,80
0.50	1,5	60,80,100
0.75	1,5	60,80,100,120,140,160
1.00	1,5	80,100,120,140,160,180,200,220
1.25	1,5	80,100,120,140,160,180,200,220
1.50	1,5	80,100,120,140,160,180,200,220
1.75	1,5	80,100,120,140,160,180,200,220
1.90	1,5	80,100,120,140,160,180,200,220

5.8.3 GG Tauri

GG Tauri is a close binary system with a separation of $0\farcs255$ (Leinert et al. 1991) and a large circumbinary disk (inner radius $\sim$ 180 AU and outer radius $\sim$ 800 AU; Simon & Guilloteau 1992; Dutrey, Guilloteau, & Simon 1994). These radii were determined from detailed modeling of the $\lambda = 2.7$ mm continuum ($1\farcs7$ resolution) and the large-scale CO rotating disk. In Paper I, Figure 4.5 shows the BIMA image; the structure is ring-like in panel (c), becoming "clumpy" by panel (d). We model this source with the standard circumstellar disk model, but following the results of (Dutrey, Guilloteau, & Simon 1994) we allow large inner radii and large outer radii. We adopt the principal axis derived from a Gaussian fit to the emission in Figure 4.5 (c), 20°, and we use the inclination angle from the models of Dutrey, Guilloteau, & Simon (1994), 43°.

In Figure 5.20, the *u,v* data are shown for GG Tauri. The data show that GG Tauri has clearly been resolved by the observations. Since the model has a large inner radii (in effect an annulus), the effect in the *u,v* plane is to convolve the expected power-law profile with a modified first order Bessel function ($\sim J_1(\beta)/\beta$), which causes a strong ringing effect in the *u,v* plane. If the data had enough signal to noise, the oscillations would be clear. Since we average in *u,v* bins, the oscillation is smeared out. The models for GG Tauri have acceptable fits for all surface density power-law indices. However, none of the models can fit the last *u,v* data point. That data point is a $> 2.5\sigma$ detection. Since the model cannot fit the last data bin, we must conclude that there may be some residual structures at small scales, possibly two circumstellar disks. The circumbinary disk mass derived is typically in the range of 0.08 to 0.11 $M_\odot$.

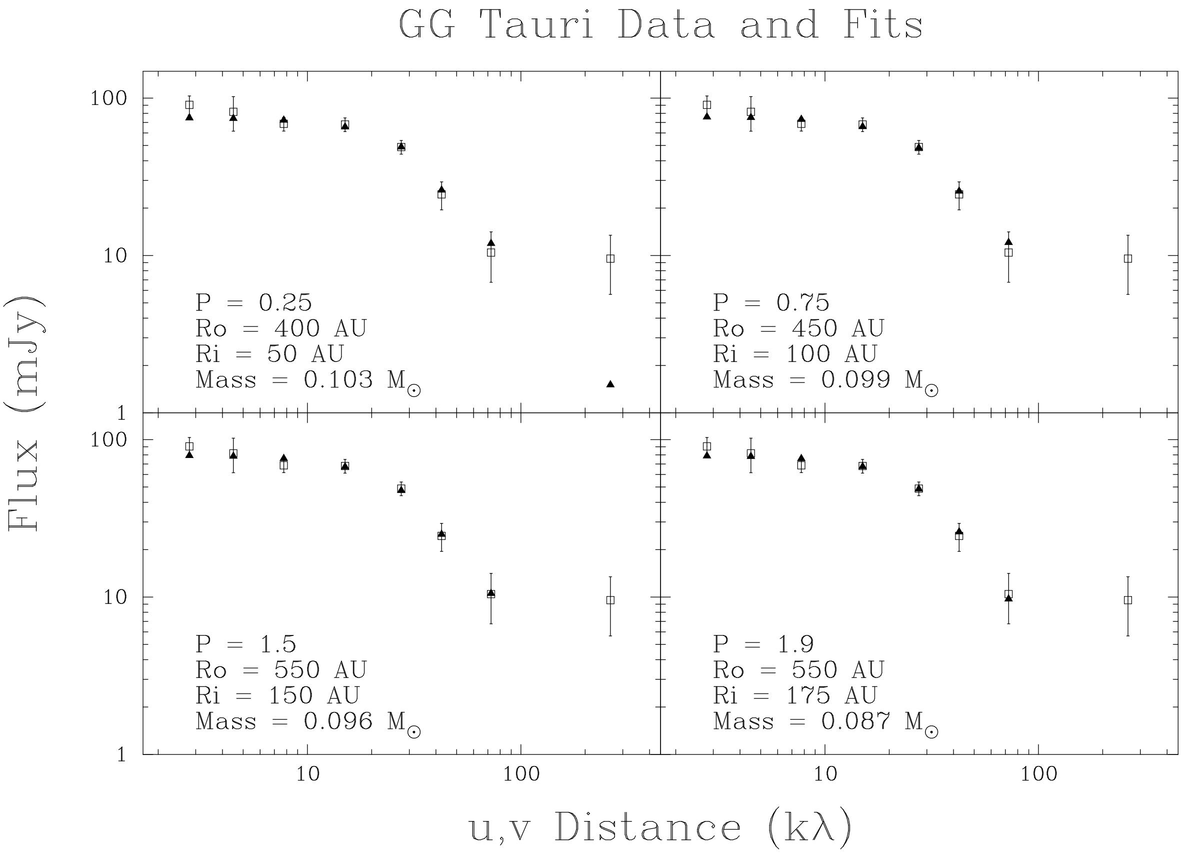

Fig. 5.20. The *u,v* data binned in annuli around GG Tauri and four fits to the data using a standard envelope model with a large inner radius cutoff, $\Sigma \propto (\frac{r}{1AU})^{-p}$, $T(r) = 350(\frac{r}{1AU})^{-0.5}$ K, $i = 43°$, and $\gamma = 20°$.

Table 5.10. GG Tauri Fit Summary

p index	R_i (AU)	R_o (AU)
0.00	50	350,400
	75	400
0.25	50	450
	75	400,450
	100	400
0.50	50	450,500
	75	400,450
	100	400,450
	125	400
0.75	50	500,550
	75	500
	100	450,500
	125	450
1.00	100	500,550
	125	450,500
	150	450

Table 5.10—Continued

p index	R_i (AU)	R_o (AU)
1.25	125	500,550
	150	450,500
1.50	150	500,550
	175	450,500
1.75	150	550,600,650
	175	500,550
1.90	150	650
	175	500,550,600

5.9 Circumstellar Disk Conclusions

For the circumstellar disks of the HL Tauri and DG Tauri, we have placed limits on the most likely power-law index and outer radius. For HL Tauri, we have more data in the slope region of the *u,v* plot, allowing us to place firm limits of $0.5 < \mathrm{p} < 1.25$ ($\chi^2 < 1.0$). In the case of GG Tauri, we have showed that the ring model produces acceptable fits over a wide range of density power-law indices. In addition, there is likely contribution to flux from a point source, which may correspond to two circumstellar disks.

We thank Mark Wolfire for all of his help and advice on how to properly use his self-consistent radiative transfer code to calculate the temperature profile for the envelope sources. This work was supported by NSF Grants NSF-FD93-20238 and AST-9314847. LGM acknowledges support from NASA grant NAGW-3066.

Chapter 6

Conclusions and Future Directions

6.1 Thesis Conclusions

The unique, high resolution observations presented in this thesis, combined with detailed modeling in the *u,v* plane, have provided insights into many of the major questions in modern star formation theory. With the capabilities of the BIMA interferometer, we have made important steps forward in the understanding of star formation from the early stages of deeply embedded protostars to the latter stages of optical T Tauri systems. Here, we will briefly summarize some of the important conclusions of this thesis.

(1) With the highest angular resolution to date at this wavelength, we are able to image circumstellar disks (Mundy et al. 1996) and search for close binaries (Looney, Mundy, & Welch 1997); with a combination of low and high resolutions, we are able to map the envelopes of the embedded sources and resolve out the large-scale structure in order to peer inside the envelopes and image the central regions.

(2) The detailed $\lambda = 2.7$ mm continuum study of L1551 IRS5 highlights the

importance of high resolution imaging; to correctly model and understand these young systems, we need to have structural information on a broad range of size scales. In the case of L1551 IRS5, we resolved a close binary system with two circumstellar disks in this archetype Class I single source (Adams, Lada, & Shu 1987). This binarity was recently confirmed by high resolution $\lambda = 7$ mm observations (Rodríguez et al. 1998). We determined that the system is comprised of three dust structures: a circumstellar envelope ($\sim$ 1200 AU in radius), a circumbinary structure ($\sim$ 75 AU in radius), and two circumstellar disks with radii $\leq$ 25 AU.

(3) We performed a high resolution survey of 24 young stellar objects in the $\lambda = 2.7$ mm continuum. This is the first sub-arcsecond resolution survey of dust structures around young stars at this wavelength.

(4) The morphology of the optical and embedded systems are distinctly different. The optical T Tauri stars exhibit compact emission from the circumstellar disks on size scales of 1 arcsecond or less. This circumstellar disk is resolved in the HL Tauri and DG Tauri systems, and a circumbinary disk is resolved in the GG Tauri system. The embedded systems exhibit continuum emission that is dominated by a large scale, spherical circumstellar envelope, with little residual emission at small scales; thus, the envelope is the main reservoir of mass in embedded systems. If there are circumstellar disks in these systems, they are not over-massive compared to the envelope power-law extended to small scales.

(5) Simple mass estimates of the circumstellar material derive masses of 0.06 to 1.98 $M_\odot$ for the embedded systems and 0.01 to 0.06 $M_\odot$ for the optical systems. This, combined with the source luminosities, suggests that the optical sources have accreted most of their final stellar mass and that even the deeply embedded systems have accreted a significant fraction of their final stellar mass.

(6) The survey has a large number of multiple systems; morphologically, they can be separated into three types: independent envelope, common envelope, and common disk systems, characterized by separations of $\geq$ 6500 AU, 3000 to 150 AU, and $<$ 100 AU, respectively. These scales are probably indicative of the formation mechanism for multiple systems. The large separation is the size scale, suggested by Larson (1995), for prompt initial fragmentation of clouds; the collapse is initiated in a cloud that contains a number of weakly condensed Jeans masses (Larson 1978; Pringle 1989; Bonnell et al. 1991). The mid-range separation is the expectation of a moderately centrally-condensed spherical system (Burkert & Bodenheimer 1993; Boss 1995; Boss 1997). Finally, the close multiple systems are similar to disk models with high angular momentum which fragment early in the disk formation (Artymowiez & Lubow 1994; Bate & Bonnell 1997).

(7) Utilizing a self-consistent radiative transfer code (Wolfire & Cassinelli 1986), we found that the $T \propto r^{-0.4}$ is a good approximation for many systems, but for envelopes with steep density profiles or massive envelopes, one needs to utilize self-consistent models to accurate model the temperature profile in the envelope. The temperature profile diverges from the $T \propto r^{-0.4}$ assumption mostly in the inner radii of the envelope ($\leq$ 100 AU) where the data presented in this thesis are less sensitive.

(8) The embedded systems can be modeled with the standard envelope model plus an embedded point source to represent a circumstellar disk. In half of the modeled embedded systems, the density profile is well described by a power-law between p = 1.0 and p = 2.0, which is expected by all of the collapse models and numerical studies. However, for the more massive envelopes, the simple envelope model suggested steep power-law indexes p $>$ 2.0. Since these sources are most effected by the $T \propto r^{-0.4}$ assumption, we modeled NGC 1333

IRAS4 A, NGC 1333 IRAS4 B, L1448 IRS3 B, and SVS13 A (a low mass envelope system), using the self-consistent temperature model. The χ^2 for fits with p $<$ 2.0 were significantly reduced compared to the fixed temperature power-law models for the more massive envelopes. The fit of SVS13 A was mostly unchanged. We explored other assumptions that may result in derived steep density profiles.

(9) All of the embedded systems have acceptable models with no central point source, but point sources flux values typically ranged from 5 to 40 mJy, or disk mass estimates of 0.02 to 0.2 $M_{\odot}$. The addition of the point source is cross-correlated with the power-law index and the inner and outer radii, so the exact value of the point source is difficult to determine. Our data conclusively show that the majority of the emission arises from the circumstellar envelope, and, since our circumstellar envelope mass estimates range from 0.5 to 4.2 $M_{\odot}$, typically, 90% of the mass is located in the envelope.

(10) The standard circumstellar disk model fits the *u,v* data of the three brightest optical systems. For the case of HL Tauri, which has the most signal to noise, we constrain the surface density power-law index to be $0.5 < p < 1.5$. We fit the circumbinary disk of GG Tauri with a standard circumstellar disk model with a large inner radii, basically an annulus. The circumstellar disk masses range from 0.04 to 0.09 $M_{\odot}$, and the circumbinary disk mass range from 0.08 to 0.11 $M_{\odot}$.

6.2 Future Directions

As the data in this thesis have shown, sub-arcsecond, or better, resolution can provide unique insight into understanding the process of star formation. The data presented in this thesis are from the 9-element BIMA interferometer operating at $\lambda = 2.7$ mm during the 1995/1996 observing season. In 1997, we expanded the baselines of the BIMA Array to 1.9 km. In addition, BIMA has installed $\lambda = 1.3$ mm receivers and added another antenna, bringing the total to ten. We intend to build on this thesis work with more observations of young systems, higher resolution observations, and data at $\lambda = 1.3$ mm and 2.7 mm.

High resolution observations in the $\lambda = 1.3$ mm band will provide $0\rlap{.}''2$ resolution, or 30 AU linear resolution at the distance of Taurus. Since dust emission increases rapidly with frequency $\left(F_\nu \propto \nu^{(2.5\ to\ 4.0)}\right)$, we should be able to achieve better signal-to-noise than that of the data presented here. With the increase in resolution, the circumstellar disks of the optical sources will have more resolution elements across the disk, which will place more constraints on the surface density power-law index. For the embedded systems, which are about twice as distant as Taurus, we will be able probe deeper into the envelope to examine the details of the collapse process on scales of 50 to 1000 AU and place better constraints on the size and mass of any circumstellar disks. The modeling in this thesis can be further constrained by observations at other wavelengths; the addition of $\lambda = 1.3$ mm and 7 mm observations will improve the constraints detailed here.

With the increased sensitivity to dust structures at $\lambda = 1.3$ mm, we will further our study to younger systems, specifically starless cores which contain no IRAS (far infrared) sources. By observing objects which have not yet formed stars, we will gain information of the density profile at an earlier time in the star formation process than the data presented in this thesis. Starless cores are thought to represent an earlier evolutionary stage, before or right after the initial collapse. In these objects, we can examine the envelope density and kinematics in regions which are as yet undisturbed by protostellar outflows, winds, or jets. Recent submillimeter studies have shown that the emissivity profiles of starless cores, thus probably their density profiles, are flat in the center (Ward-Thompson et al. 1994). In view of our findings that luminous systems often contain multiple systems, one explanation could be that the starless cores are forming multiple systems within separate condensations that appear as a flat distribution at low resolution. Interferometric observations can prove or disprove this possibility.

Our most important future goal is to increase the sample of young stellar systems observed at high resolution with the BIMA interferometer. With such studies, we can image the circumstellar disks of more objects, search for close binary systems in the local star forming regions, and provide an ensemble of modeling that will begin to place stronger limits on the density profiles, sizes, and evolution of young stellar systems.

REFERENCES

Adams, F.C., Emerson, J.P., & Fuller, G.A. 1990, ApJ, 357, 606

Adams, F.C., Lada, C.J., & Shu, F.H. 1987, ApJ, 312, 788

Adams, F.C., Ruden, S.P., & Shu, F.H. 1989, ApJ, 347, 959

Adams, F.C. & Shu, F.H. 1985, ApJ, 296, 655

Adams, F.C., Shu, F.H, & Lada, C.J. 1988, ApJ, 336, 865

André, P. 1987, Molecular Clouds and Protostars, ed. T. Montmerle & C. Bertout, (Sacaly, CEA)

André, P., Deeney, B.D., Phillips, R.B., & Lestrade, J. 1992, ApJ, 401, 667

André, P., Martín-Pintado, J., Despois, D., & Montmerle, T. 1990, A&A, 236, 180

André, P., Ward-Thompson, D., & Barsony, M. 1993, ApJ, 406, 122

Anglada, G., Rodríguez, L.F., Torrelles, J.M., Estalella, R., Ho, P.T.P, Cantó, J., López, R., & Verdes-Montenegro, L. 1989, ApJ, 341, 208

Artymowiez, P., & Lubow, S.H. 1994, ApJ, 421, 651

Aspin, C., Sandell, G., & Russell, A.P.G. 1994, A&AS, 106, 165

Baade, W. 1952, Trans. IAU 8, ed. P.Th. Oosterhoff, (Cambridge: Cambridge Univ. Press)

Bachiller, R., André, P., & Cabrit, S. 1991, A&A, 241, L43

Bachiller, R., & Cernicharo, J. 1986, A&A, 166, 283

Bachiller, R., Cernicharo, J., Martín-Pintado, J., Tafalla, M., & Lazareff, B. 1990, A&A, 231, 174

Bachiller, R., Guilloteau, S., Dutrey, A., Planesas, P., & Martín-Pintado, J. 1995, A&A, 299, 857

Bally, J., Devine, D., & Reipurth, B. 1996, ApJ, 473, L49

Barnard, E.E. 1919, ApJ, 49, 12

Basu, S., & Mouschovias, T.C. 1994, ApJ, 432, 720

Basu, S., & Mouschovias, T.C. 1995, ApJ, 452, 286

Bate, M.R., & Bonnell, I.A. 1997, MNRAS, 285, 33

Bate, M.R., Bonnell, I.A., & Price, N.M. 1995, MNRAS, 277, 362

Bazell, D., & Dwek, E. 1990, ApJ, 360

Beckwith, S.V.W., & Birk, C.C. 1995, ApJ, 449, L59

Beckwith, S.V.W., & Sargent, A.I. 1991, ApJ, 381, 250

Beckwith, S.V.W., Sargent, A.I., Chini, R.S., & Güsten, R. 1990, AJ, 99, 924

Beckwith, S.V.W., Sargent, A.I., Scoville, N.Z., Masson, C.R., Zuckerman, B., & Phillips, T.G. 1986, ApJ, 309, 755

Begemann, B., Dorschner, J., Henning, Th., Mutschke, H., & Thamm, E. 1994, ApJ, 423, L71

Bertout, C., Basri, G., & Bouvier, J. 1988, ApJ, 330, 350

Bieging, J., & Cohen, M. 1985, ApJ, 289, L5

Bieging, J., Cohen, M., & Schwartz, P.R. 1984, ApJ, 282, 699

Blake, G.A. 1997, IAU Symposium 178, Molecules in Astrophysics: Probes and Processes, ed. E.F. van Dishoeck, (Dordrecht: Kluwer), 31

Bok, B.J. & Reilly, E.F. 1947, ApJ, 105, 255

Bonnell, I.A. 1994, MNRAS, 269, 837

Bonnell, I.A., & Bastein, P. 1992, ApJ, 401, 654

Bonnell, I.A., & Bate, M.R. 1994, MNRAS, 271, 999

Bonnell, I.A., Bate, M.R., Clarke, C.J., & Pringle, J.E. 1997, MNRAS, 285, 201

Bonnell, I.A., Martel, H., Bastein, P., Arcoragi, J.P., & Benz, W. 1991, ApJ, 377, 553

Bontemps, S., & André, P. 1997, Low Mass Star Formation from Infall to Outflow, Poster proceedings of IAU Symposium 182, Low Herbig-Haro Flows and the Birth of Low Mass Stars, ed. F. Malbet & A. Castets, 63

Boss, A.P. 1993, ApJ, 410, 157

Boss, A.P. 1995, Rev. Mex. A. A., 1, 165

Boss, A.P. 1997, ApJ, 483, 309

Boss, A.P., & Bodenheimer, P. 1979, ApJ, 234, 289

Bouvier, J., Cabrit, S., Fernández, M., Martín, E.L., & Matthews, J.M. 1993, A&AS, 101, 485

Bracewell, R.N. 1965, The Fourier Transform and its Application, (New York, McGraw Hill)

Briggs, D.S. 1995, BAAS, 187, 112.02

Burkert, A., & Bodenheimer, P. 1993, MNRAS, 264, 798

Butner, H.M., Evans II, N.J., Lester, D.F., Levreault, R.M., & Strom, S.E. 1991, ApJ, 376, 636

Calvet, N, Hartmann, L., Kenyon, S.J., & Whitney, B.A. 1994, ApJ, 434, 330

Cameron, A.G.W. 1962, Icarus, 1, 13

Cassen, P., & Moosman, A. 1981, Icarus, 48, 353

Cassen, P., & Summers, A. 1983, Icarus, 53, 26

Cernis, K. 1990, Ap&SS, 166, 315

Chini, R. Henning, Th., & Pfau, W. 1991, A&A, 247, 157

Chini, R., Reipurth, B., Sievers, A., Ward-Thompson, D., Haslam, C.G.T., Kreysa, E., & Lemke, R. 1997, A&A, 325, 542

Clarke, C. 1995, A&AS, 223, 73

Clarke, C., & Pringle, J.E. 1991, MNRAS, 249, 584

Close, L.M., Roddier, F., Northcott, M.J., Roddier, C., & Graves, J.E. 1995, ApJ, 478, 766

Cohen, M. 1983, ApJ, 270, L69

Cohen, M., Bieging, J., & Schwartz, P.R. 1982, ApJ, 253, 707

Cohen, M. & Kuhi, L.V. 1979, ApJS, 41, 743

Curiel, S., Raymond, J.C., Rodríguez, L.F., Cantó, J., & Moran, J.M. 1990, ApJ, 365, L85

Davis, C.J., & Smith, M.D. 1995, ApJ, 443, L41

Dent, W.R.F., Matthews, H.E., & Walther, D.M. 1995, MNRAS, 277, 193

Draine, B.T. 1985, ApJS, 57, 587

Draine, B.T. 1990, The Interstellar Medium in Galaxies, ed. H.A. Thronson & J.M. Shull, (Dordrecht: Kluwer), 483

Draine, B.T., & Lee, H.M. 1994, ApJ, 285, 89

Dulk, G.A. 1985, ARA&A, 23, 169

Duquennoy, A., & Mayor, M. 1991, A&A, 248, 485

Durisen, R.H., Gingold, R.A., Tohline, J.E., & Boss, A.P. 1986, ApJ, 305, 281

Durisen, R.H., & Sterzik, M.F. 1994, A&A, 286, 84

Dutrey, A., Guilloteau, S., Duvert, G., Prato, L., Simon, M., Schuster, K., & Ménard, F. 1996, A&A, 309, 493

Dutrey, A., Guilloteau, S., & Simon, M. 1994, A&A, 286, 149

Dutrey, A., Guilloteau, S., Prato, L., Simon, M., Duvert, G., Schuster, K., & Ménard, F. 1998, A&A, 338, L63

Edwards, S., Ray, T., & Mundt, R. 1993, Protostars and Planets III, ed. E.H. Levy & J.I. Lunine, (Tucson, Univ. of Arizona Press), 567

Eislüffel, J., Günther, E., Hessman, F.V., Mundt, R., Poetzel, R., Carr, J.S., Beckwith, S.V.W., & Ray, T.P. 1991, ApJ, 383, L19

Elias, J. 1978, ApJ, 224, 857

Feigelson, E.D. 1987, Cool Stars, Stellar Systems, and the Sun, ed. J.L. Linsky & R.E. Stencel (Berlin, Springer), 455

Fiedler, R.A., & Mouschovias, T.C. 1992, ApJ, 391, 199

Fiedler, R.A., & Mouschovias, T.C. 1993, ApJ, 415, 680

Foster, P.N., & Chevalier, R.A. 1993, ApJ, 415, 680

Fuller, G.A., Ladd, E.F., & Hodapp, K.W. 1996, ApJ463, L97

Fuller, G.A., Ladd, E.F., Padman, R, Myers, P.C., & Adams, F.C. 1995, ApJ, 454, 862

Galli, D., & Shu, F. 1993, AJ417, 243

Gehrz, R.D. 1989, Interstellar Dust: Proc. IAU Symp. 135, ed. L. Allamandola & A.G.G.M. Tielens (Dordrecht: Kluwer), 445

Ghez, A.M., Neugebauer, G., Matthews, K. 1993, AJ, 106, 2005

Ghez, A.M., White, R.J., & Simon, M. 1997, ApJ, 490, 353

Glyn Jones, K. 1968, Messier's Nebulae and Star Clusters, (London: Faber and Faber), 157

Gradshteyn, I.S., & Ryzhik, I.M. 1980, Table of Integrals, Series, and Products, (New York, Academic Press)

Grossman, E.N., Masson, C.R., Sargent, A.I., Scoville, N.Z., Scott, S., & Woody, D.P. 1987, ApJ, 320, 356

Hartigan, P., Edwards, S., & Ghandour, L. 1995, ApJ, 452, 736

Harvey, P.M., Thronson, A.T., & Gatley, I. 1979, ApJ, 231, 115

Hayashi, M., Ohashi, N., & Miyama, S.M. 1993, ApJ, 418, L71

Heintz, W.D. 1969, JRASC, 63, 275

Helmholtz, H. 1853, Cited Lecture Kelvin (1863)

Henning, Th., Chini, R., & Pfau, W. 1992, A&A, 263, 285

Henning, Th., Michel B., & Stognienko, R. 1995, Planet. Space Sci., 43, 1333

Herbig, G.H. 1952, JRASC, 46, 233

Herbig, G. H. 1974, Lick Observatory Bulletin No. 658

Herbig, G.H., & Jones, B.F. 1983, AJ, 88, 1040

Herschel, Wm. 1784, Phil. Trans. Roy. Soc., A74, 437

Hildebrand, R.H. 1983, Quart. J. Roy. Astron. Soc., 24, 267

Högbom, J.A. 1974, A&AS, 15, 417

Holdaway, M.A., & Owens, F.N. 1995, NRAO. Millimeter Array Memo 126.

Hunter, C. 1977, ApJ, 218, 834

Jeans, J.H. 1928, Astronomy and Cosmogony, (Cambridge: Cambridge Univ. Press)

Jennings, R.E., Cameron, D.H.M., Cudlip, W., & Hirst, C.J. 1987, MNRAS, 226, 461

Jensen, E.L.N., Mathieu, R.D., & Fuller, G.A. 1994, ApJ, 429, L29

Jensen, E.L.N., Mathieu, R.D., & Fuller, G.A. 1996, ApJ, 458, 312

Jones, A.P. 1988, MNRAS, 234, 209

Jones, B.F., & Cohen, M. 1986, ApJ, 311, L23

Joy, A. 1945, ApJ, 102, 168

Joy, A. 1946, PASP, 58, 244

Kant, I 1755, Allegmeine Naturgeschichte und Teorie des Himmels

Keene, J., & Masson, C.R. 1990, ApJ, 355, 635

Kelvin, W.T. 1863, Brit. Assoc. Rep. Part II, p27, Les Mondes 3, 472

Kenyon, S.J,, & Hartmann, L. 1987, ApJ, 323, 714

Kepner, J., Hartigan, P., Yang C., & Strom, S. 1993, ApJ, 415, L119

Kitamura, Y., Kawabe, R., & Saito, M. 1996, ApJ, 456, L137

Koerner, D.W. & Sargent, A.I. 1997, personal communication

Koerner, D.W. & Sargent, A.I. 1998, personal communication

Koerner, D.W., Sargent, A.I., & Beckwith, S.V.W. 1993, Icarus, 106, 2

Königl, A., & Ruden, S.P. 1993, Protostars and Planets III, ed. E.H. Levy & J.I. Lunine, (Tucson, Univ. of Arizona Press), 641

Kraus, J.D. 1966, Radio Astronomy, (New York, McGraw Hill)

Krügel, E, & Siebenmorgen, R. 1994, A&A, 288, 929

Lada, C.J. 1987, Star Forming Regions: Proc. IAU Symp. 115, ed. A.K. Dupree & M.T.V.T. Lago, (Dordrecht: Kluwer), 1

Lada, C.J., Alves, J., & Lada, E.A. 1996, AJ, 111, 1964

Lada, C.J., & Wilking, B.A. 1984, ApJ, 287, 610

Ladd, E.F., Fuller, G.A., Padman, R., Myers, P.C., & Adams, F.C. 1995, ApJ, 439, 771

Langer, W.D., Castets, A., & Lefloch, B. 1996 ApJ, 471, L111

Larson, R.B. 1969, MNRAS, 145, 271

Larson, R.B. 1978, MNRAS, 184, 69

Larson, R.B. 1995, MNRAS, 272, 213

Lavalley, C., Cabrit, S., Dougados, C., Ferruit, P., & Bacon, R. 1997, A&A, 327, 671

Lay, O.P. 1994, Ph.D. Thesis, Cambridge Univ.

Lay, O.P., Carlstrom, J.E., & Hills, R.E. 1995, ApJ, 452, L73

Lay, O.P., Carlstrom, J.E., & Hills, R.E. 1997, ApJ, 489, 917

Lay, O.P., Carlstrom, J.E., Hills, R.E., & Philips, T.G. 1994, ApJ, 434, L75

Leinert, Ch., Haas, M., Richichi, A., Zinnecker, H., & Mundt, R. 1991, A&A, 250, 407

Leinert, Ch., Zinnecker, H., Weitzel, N., Christou, J., Ridgway, S.T., Jameson, R., Haas, M., & Lenzen, R., 1993, A&A, 278, 129

Lin, D.N.C., & Papaloizou, J.C.B. 1979, MNRAS, 186, 799

Lin, D.N.C., & Pringle, J.E. 1990, ApJ, 358, 515

Liseau, R., Sandell, G., & Knee, L.B.G. 1988, A&A, 192, 153

Lockyer, N. 1887, Proc. Roy. Soc., 43

Lockyer, N. 1888, Proc. Roy. Soc., 44

Looney, L.W., Mundy, L.G., & Welch, W.J. 1997, 484, L157

Looney, L.W., Mundy, L.G., & Welch, W.J. 1998, ApJ, submitted

Lynden-Bell, D, & Pringle, J.E. 1974, MNRAS, 168, 603

Marcy, G.W., & Butler, R.P. 1996, ApJ, 464, L153

Mathis, J.S., Rumpl, W., & Nordsieck, K.H. 1977, ApJ, 217, 425

Mayor, M., & Queloz, D. 1995, Nature, 378, 355

Mendoza, E.E. 1966, ApJ, 143, 1010

Mendoza, E.E. 1968, ApJ, 151, 977

Messier, C. 1781, Nebulae and Star Clusters

Mestel, L., & Spitzer, L. Jr. 1956, MNRAS, 116, 505

Mezger, P.G., & Henderson, A.P. 1967, ApJ, 147, 471

Mitchell, G.F., Hasegawa, T.I., Dent, W.R.F., & Matthews, H.E. 1994, ApJ, 436, L177

Mitchell, G.F., Sargent, A.I., & Mannings, V. 1997, ApJ, 483, L127

Morgan, J.A., Snell, R.L., & Strom, K.M. 1990, ApJ, 376, 618

Monaghan, J.J., & Lattanzio, J.C. 1986, A&A, 158, 207

Mouschovias, T., Paleologu, E.V., & Fiedler, R.A. 1985, ApJ, 291, 772

Mundt, R., Brugel, E.W., & Bührke, T. 1987, ApJ, 319, 275

Mundt, R., & Fried, J.W. 1983, ApJ, 274, L83

Mundt, R., Ray, T.P., Raga, A.C., & Solf, J. 1990, A&A, 232, 37

Mundy, L.G., McMullin, J.P, Grossman, A.W., & Sandell, G. 1993, Icarus, 106, 11

Mundy, L.G., Looney, L.W., Erickson, W., Grossman, A., Welch, W.J., Forster, J.R., Wright, M.C.H., Plambeck, R.L., Lugten, J., & Thornton, D.D. 1996, ApJ, 464, L169

Mundy, L.G., Looney, L.W. & Welch, W.J. 1998, in prep

Mundy, L.G., Wilking, B.A., & Myers, S.T. 1986, ApJ, 311, L75

Mundy, L.G., Wootten, A., Wilking, B.A., Blake, G.A., & Sargent, A.I. 1992, ApJ, 385, 306

Myers, P.C., & Ladd, E.F. 1993, ApJ, 413, L47

Nakano, T. 1984, Fund. Cosmic Phys., 9, 139

Natta, A. 1993, ApJ, 412, 761

Ohashi, N., Kawabe, R., Hayashi, M., & Ishiguro, M. 1991, AJ, 102, 2054

Ohashi, N., Hayahi, M., Ho, P.T., Momose, M., & Hirano, N. 1996, AJ, 466, 957

Ossenkopf, V. 1991, A&A, 251, 210

Osterloh, M., & Beckwith, S.V.W. 1995, ApJ, 439, 288

Ouyed, R., Pudritz, R.E. 1997, ApJ, 482, 7120

Patience, J., Ghez, A.M., Reid, I.N., Weinberger, A.J., & Matthews, K. 1998, AJ, In Press

Panagia, N., & Felli, M. 1975, A&A, 39, 1

Penston, M.V. 1969, MNRAS, 144, 425

Pollack, J.B., Hollenbach, D., Beckwith, S.V.W., Simonelli, D.P., Roush, T., & Fong, W. 1994, ApJ, 421, 615

Preibisch, T., Ossenkopf, V., Yorke, H.W., & Henning, Th. 1993, A&A, 279, 577

Pringle, J.E. 1989, MNRAS, 239, 361

Pringle, J.E. 1991, The Physics of Star Formation and Early Stellar Evolution, ed. N. Kylafis & C.J. Lada, (Dordrecht:Kluwer), 437

Pudritz, R.E., Wilson, C.D., Carlstrom, J.E., Lay, O.P., Hills, R.E., & Ward-Thompson, D. 1996, ApJ, 470, L123

Reipurth, B., & Zinnecker, H. 1993, A&A, 278, 81

Reynolds, S.P. 1986, ApJ, 304, 713

Rodríguez, L.F., Anglada, G., & Curiel, S. 1997, ApJ, 480, L125

Rodríguez, L.F., Anglada, G., & Raga, A. 1995, ApJ, 454, L149

Rodríguez, L.F., Cantó, J., Torrelles, J.M., Gómez, J.F., Anglada, G., & Ho, P.T.P. 1994, ApJ, 427, L29

Rodríguez, L.F., Cantó, J., Torrelles, J.M., & Ho, P.T.P. 1986, ApJ, 301, L25

Rodríguez, L.F., D'Alessio, P., Wilner, D.J., Ho, P.T.P., Torrelles, J.M., Curiel, S., Gómez, J.F., Lizano, S., Pedlar, A., Canto, J., & Raga, A. 1998, Nature, 395, 355

Rodríguez, L.F., Myers, P.C., Cruz-González, I., & Terebey, S. 1989, ApJ, 347, 461

Rohlfs, K. 1986, Tools of Radio Astronomy, (Berlin, Springer-Verlag)

Rowan-Robinson, M. 1980, ApJS, 44, 403

Ruden, S.P., & Lin, D.N.C. 1986, ApJ, 308, 883

Ruden, S.P., & Pollack, J.B. 1991, ApJ, 375, 740

Safier, P.N., McKee, C.F., & Stahler, S.W. 1997, ApJ, 660

Safronov, V.S. 1960, Ann, Astrophys, 23, 901

Sandell, G., Aspin, C., Duncan, W.D., Russell, A.P.G., & Robson, I.E. 1991, ApJ, 376, L17

Sandell, G., Knee, L.B.G., Aspin, C., Robson, I.E., & Russell, A.P.G. 1994, A&A, 285, L1

Sargent, A.I., & Beckwith, S.V.W. 1987, ApJ, 323, 294

Sargent, A.I., & Beckwith, S.V.W. 1991, ApJ, 382, L31

Schwartz, P.R., Simon, T., & Zuckerman, B. 1983, *Rev. Mex. Astr. Ap.*, 7, 191

Shu, F.H. 1977, ApJ, 214, 488

Shu, F.H., Adams, F.C, & Lizano, S. 1987, ARA&A, 25, 23

Shu, F.H., Najita, J., Galli, D., Ostriker, E., & Lizano, S. 1993, Protostars and Planets III, ed. E.H. Levy & J.I. Lunine, (Tucson, Univ. of Arizona Press), 3

Shu, F.H., Najita, J., Ostriker, E., Wilkin, F., Ruden, S., & Lizano, S. 1994, ApJ, 429, 781

Shu, F.H., Tremaine, S., Adams, F.C., & Ruden, S.P 1990, ApJ, 358, 495

Simon, M., Chen, W.P., Howell, R.R., Benson, J.A., & Slowik, D. 1992, ApJ, 384, 212

Simon, M., Ghez, A.M., Leinert, Ch., Cassar, L., Chen, W.P., Howell, R.R., Jameson, R.F., Matthews, K., Neugebauer, G., & Richichi, A. 1995, ApJ, 443, 625

Simon, M., & Guilloteau, S. 1992, ApJ, 397, L47

Snell, R.L., & Bally, J. 1986, ApJ, 303, 683

Snell, R.L., Loren, R.B., & Plambeck, R.L. 1980, ApJ, 239, L17

Spitzer, L., Jr. 1978, Physical Processes in the Interstellar Medium, (New York, Wiley)

Stahler, S.W., Korycansky, D.G., Brothers, M.J., & Touma, J. 1994, ApJ, 431, 341

Stapelfeldt, K.R., et al. 1995, ApJ, 449, 888

Stapelfeldt, K.R., Burrows, C.J., Krist, J.E., & the WFPC2 Science Team 1997, IAU Symposium 182, Herbig-Haro Flows and the Birth of Low Mass Stars, ed. B. Reipurth & C. Bertout, (Dordrecht: Kluwer), 355

Stine, P.C., Feigelson, E.D., André, P., & Montmerle, T. 1988, AJ, 96, 1394

Stognienko, R., Henning, T., & Ossenkopf, V. 1995, A&A, 296, 797

Strom, S.E., Grasdalen, G.L., & Strom, K.M. 1974, ApJ, 191, 111

Strom, K.M., Strom, S.E., & Vrba, F.J. 1976, AJ, 81, 320

Strom, S.E., Vrba, F.J., & Strom, K.M., 1976, AJ, 81, 314

Suters, M., Stewart, R.T., Brown, A., & Zealey, W. 1996, AJ, 111, 320

Terebey, S., Chandler, C.J., & André, P. 1993, ApJ, 414, 759

Terebey, S., & Padgett, D.L. 1997 , IAU Symposium 182, Herbig-Haro Flows and the Birth of Low Mass Stars, ed. B. Reipurth & C. Bertout, (Dordrecht: Kluwer), 507

Terebey, S., Shu, F.H., & Cassen, P. 1984, ApJ, 286, 529

Thamm, E., Steinacker, J., & Henning, Th. 1994, A&A, 287, 493

Thompson, A.R., Moran, J.M., & Swenson, G.W. 1986, Interferometry and Synthesis in Radio Astronomy, (New York, Wiley-Interscience)

van Diskoeck, E.F., & Blake, G.A. 1998, ARA&A, 36, in press

Walker, C.K., Carlstom, J.E., & Bieging, J.H. 1993, ApJ, 402, 665

Walker, C.K., Lada, C.J., Young, E.T., Maloney, P.R., & Wilking, B.A. 1986, ApJ, 309, L47

Ward-Thompson, D., Robson, E.I., Whittet, D.C.B., Gordan, M.A., Walther, D.M., & Duncan, W.D. 1989, MNRAS, 241, 119

Ward-Thompson, D., Scott, P. F., Hills, R. E., & Andre, P. 1994, MNRAS, 268, 276

Warin, S., Castets, A., Langer, W.D., Wilson, R.W., & Pagani, L. 1996, A&A, 306, 935

Weintraub, D.A., Kastner, J.H., & Whitney, B.A 1995, ApJ, 452, L141

Weintraub, D.A., Sandell, G., & Duncan, W.D. 1989, ApJ, 340, L69

Welch, W.J. et al. 1996, PASP, 108, 93

Welch, W.J., Looney, L.W., & Mundy, L.G. 1998, in preparation

Whitworth, A., & Summers, D. 1985, MNRAS, 214, 1

Whittet, D.C.B. 1974, MNRAS, 168, 371

Wilner, D.J., Ho, P.T.P., & Rodríguez, L.F. 1996, ApJ, 470, L117

Wilner, D.J., Rodríguez, L.F., & Ho, P.T.P 1998, in preparation

Wilner, D.J., Welch, W.J., & Forster, J.R. 1995, ApJ, 449, L73

Wolfire, M.G., & Cassinelli, J.P. 1986, ApJ, 310, 207

Wootten, A. 1989, ApJ, 337, 858

Wright, E.L. 1982, ApJ, 255, 401

Wright, E.L. 1987, ApJ, 320, 818

Yorke, H.W., Bodenheimer, P., & Laughlin, G. 1993, ApJ, 411, 274

Yu, T., & Chernin, L.M. 1997, ApJ, 479, L63

Zinnecker, H., Bastien, P., Arcoragi, J.P., & Yorke, H.W. 1992, A&A, 265, 726